http://researchcommons.waikato.ac.nz/

Research Commons at the University of Waikato

Copyright Statement:

The digital copy of this thesis is protected by the Copyright Act 1994 (New Zealand).

The thesis may be consulted by you, provided you comply with the provisions of the Act and the following conditions of use:

- Any use you make of these documents or images must be for research or private study purposes only, and you may not make them available to any other person.
- Authors control the copyright of their thesis. You will recognise the author's right to be identified as the author of the thesis, and due acknowledgement will be made to the author where appropriate.
- You will obtain the author's permission before publishing any material from the thesis.

Preparation and Characterisation of Double Doped-CeO_2 Systems.

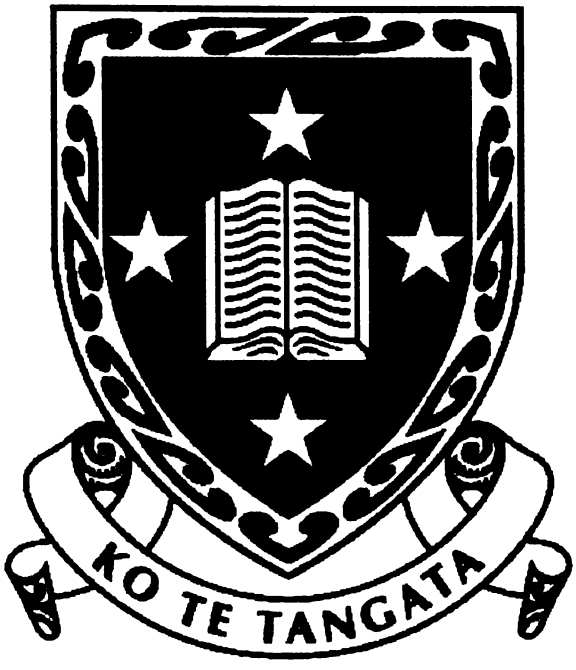

A thesis submitted in partial fulfilment of the requirements for the degree of Doctor of Philosophy at the University of Waikato by

Robert S Torrens

The University of Waikato,
Hamilton, New Zealand.

February 2002

Dedication

To my family, for their love, support, encouragement and patience with their 'perpetual student'.

FAMILY

What the term "family"
Has come to mean to me
Is a union of souls who
Always help in times of need.

They are the ones who will say
The awakening words you must hear
When you're running a wrong path
And have lost the ability to see clear.

They are the ones who give encouragement
And a positive feeling inside
When you are in the midst of turmoil
Wanting to just run and hide.

They are the ones who help you see
What life and love is all about
They are the patient listeners
When others want to shout.

They are the ones you laugh and cry with
And tell secrets you'd tell no one else
Their value more precious than a trophy
Polished and shining on your wooden shelf

They are the ones you miss the most
And go see on those special days
They are the ones who REALLY know you
And accept you anyway!

by Dawn Marie Sahli

Abstract

Potential Solid Oxide Fuel Cell (SOFC) electrolyte materials of the composition $Ce_{0.8}Gd_{0.2-x}M_xO_{2-\delta}$ (M = Pr or Sm, x = 0.005 - 0.05) were prepared by two wet-chemical methods: oxalic acid co-precipitation and a variant of the Pechini method.

X-ray diffraction of the oxide powders indicates that they are single-phase cubic fluorite materials. High temperature x-ray diffraction studies show that there is no evolution of secondary phases up to the maximum temperature of testing, 1273 K. Thermal expansion coefficients, calculated from lattice parameters measured at different temperatures, reveal the praseodymia containing samples to have a higher coefficient of thermal expansion, 1.3×10^{-5} K^{-1} as opposed to 1.0×10^{-5} K^{-1} for $Ce_{0.8}Gd_{0.2}O_{2-\delta}$.

There was little variation in particle size (measured by laser diffraction) or surface area (measured by gas adsorption) between the powder prepared by the different preparation techniques and no systematic variation with double dopant concentration. Scanning electron microscopy (SEM) of the powders showed the preparation techniques produced particles with different morphologies; co-precipitated particles were elongated crystals composed of primary crystallites, while Pechini method particles appeared to be porous agglomerates of primary crystallites. Powders produced by the Pechini method proved to be more difficult to fabricate into pellets, with problems arising during pressing and sintering, resulting in a high rejection rate.

X-ray microscopy of pressed and sintered pellets indicates that the use of a binder/lubricant reduces intra-pellet density variations.

Sintering studies indicate that, while the Pechini method powders had rapid initial densification, the co-precipitated powders were more able to obtain closed porosity (96% of the theoretical density) at lower temperatures. Praseodymia containing samples exhibited enhanced sintering compared to the other samples, achieving 98-99% of theoretical density after sintering for 10 hours at 1400 °C.

SEM investigation of sintered pellets indicates that both of the double dopant species acted to retard grain growth.

Impedance spectroscopy results show the praseodymia double doped materials to have higher conductivities than the base $Ce_{0.8}Gd_{0.2}O_{2-\delta}$ material. The praseodymia containing composition showing the highest conductivity was $Ce_{0.8}Gd_{0.185}Pr_{0.015}O_{2-\delta}$ with a conductivity of 1.3×10^{-2} S cm^{-1} (at 600 °C, in air). Samaria double doping also increased conductivity, though not to the same extent as praseodymia double doping. The highest conductivity obtained for a samaria containing sample was 1.0×10^{-2} S cm^{-1} (at 600 °C, in air) for the composition $Ce_{0.8}Gd_{0.19}Sm_{0.01}O_{2-\delta}$. The samples exhibiting the highest conductivities also had the lowest activation energies for conduction. Impedance spectroscopy results at low oxygen partial pressures indicate no difference in ionic domain boundaries.

The thesis concludes with a list of future work needed to carry on these studies.

Acknowledgements

There are a number of people that need to be mentioned for having made this work possible.

My supervisors: Dr Nigel Sammes for introducing me to the field of ceramics research and fuel cells; Professor Kevin Kendall, formerly of Keele University, UK, for facilitating the exchange program I took part in. Of particular note is Dr Tony Cartner, for his patience and perseverance on taking over my supervision with the departure of Dr Sammes.

Mr Yuanji Zhang, Dr Geoff Tompsett, Mr Alf Harris, Dr Jim Austin and Ms Jijian Lu for their technical expertise with various pieces of equipment used for this research.

Dr Andreas Markwitz of Geological and Nuclear Sciences for performing the Ion Beam Analyses.

I would also like to thank Acumentrics Corporation, USA, and the Department of Materials and Process Engineering, Waikato University, for their partial financial support during this work.

I would also like to show my appreciation to my friends who, while not necessarily helping with this research, did help the author in so many other ways:

The Keele Crew: Steph Livermoor, Ann Cantrell, Ann Diskin, Caine Finnerty, Olivier Bellon, Amy Hopkins, Steve Farris, Russell Clayton and especially Paul Windibank and Helen Taylor. For making my stay in England so memorable and enjoyable.

The Other Keele Crew: Roger Roberts, Robert Bracey, Adam Ward, Rachel Mizsei, Wayne Oatway and Kay Williams. For assisting with my escapism and increasing my experience.

The Waikato Crew: Matt Henderson, Geoff Tompsett, Mike Brown, Tracy Murray, John Davidson, Jennie Richmond, Yanhai Du, Bazz Fenton, Russell Cross, Roz Phillips and Nancy Hati. For the lab camaraderie they provided.

And finally my good friends, Conrad Lendrum and Mike Buckley. For being who they are and calling me friend.

Contents

Chapter One - Introduction

Chapter Two - Methodology

Chapter Three - Experimental Method

Chapter Four - Results and Discussion

Conclusions and Recommendations

Appendices

List of Figures

List of Tables

Chapter One

1 Introduction

1.1 Overview

This chapter provides a description of fuel cells, and investigates the driving forces for their development. Features of the more common types of fuel cell are given, with solid oxide fuel cells, SOFCs, covered in greater detail. The components used in the construction of SOFCs are given cursory coverage with the electrolyte materials covered in more detail, given that the systems studied in this research are potential SOFC electrolytes. Currently used electrolyte materials are mentioned, with consideration given to their conduction mechanisms and the affect of grain boundaries on electrical conductivity. Finally, doped ceria electrolyte alternatives are surveyed with particular interest paid to doping[1] strategies employed.

1.2 Fuel Cells, a Description

Fuel cells are electrochemical devices that convert the Gibbs free energy of fuel oxidation into direct current electricity[2]. Theoretically the Gibbs free energy can be converted with 100% efficiency, in practice efficiencies are lower from losses associated with internal resistances and electrode overpotentials. The conversion is achieved by the indirect combination of a fuel (for example natural gas) with an oxidant gas (for example air) across some form of electrolyte. While similar in structure to a battery, fuel cells are electricity generation devices rather than energy storage devices. Instead of recharging, fuel cells require a continuous supply of fuel[3].

As fuel cells directly convert the chemical potential energy of the fuel to electricity, without an intermediate thermal or mechanical step, they are not subject to the Carnot limitation[2], Equation 1.1.

$$E_C = 1 - \frac{T_c}{T_h} \qquad 1.1$$

E_c is the Carnot efficiency
T_c is the temperature of the cold reservoir
T_h is the temperature of the hot reservoir

This means that fuel cells can achieve higher efficiencies than internal combustion engines. Under ideal conditions an internal combustion engine can achieve 35% efficiency, though the average efficiency is 15%[4].

The ideal efficiency, η, of a fuel cell operating irreversibly is given by Equation 1.2[5].

$$\eta = \frac{\Delta G}{\Delta H} \qquad 1.2$$

where:
ΔG is the Gibbs free energy of the reaction
ΔH is the change in enthalpy of the reaction

Fuel cells have had measured electrical efficiencies of up to 65%[6]; 73% when incorporated into a system with a micro-turbine[7]. Steele[8] has proposed that 80% overall efficiency could be achieved with a multistage fuel cell, whereby the exhaust gas of one fuel cell was used as the fuel of the next. A further benefit fuel cells have over automotive internal combustion engines, is that the fuel cell of a stationary vehicle does not have to idle[4], unlike an internal combustion engine. Idling being a source of inefficiency in combustion engines.

Other advantages fuel cells possess are:

- low maintenance, possessing no moving parts
- low emission, being an electrochemical process unwanted SOx and NOx gases are not formed
- fuel flexibility, fuel cells can run on a variety of fuels using either internal or external reforming (refer page 6)

1.2.1 Anatomy of a Fuel Cell

A fuel cell consists of an anode and a cathode, separated by an electrolyte material. The fuel is oxidised at the anode and electrons are released to the external circuit, generating a current. The electrons are accepted by the cathode, where the oxidant is reduced, refer Figure 1.1. There is also movement of a charged species through the electrolyte. The exact nature of the charged species varies with fuel cell type. The nature of the conducting ion also determines where water is formed in the cell, either the anode or the cathode[5].

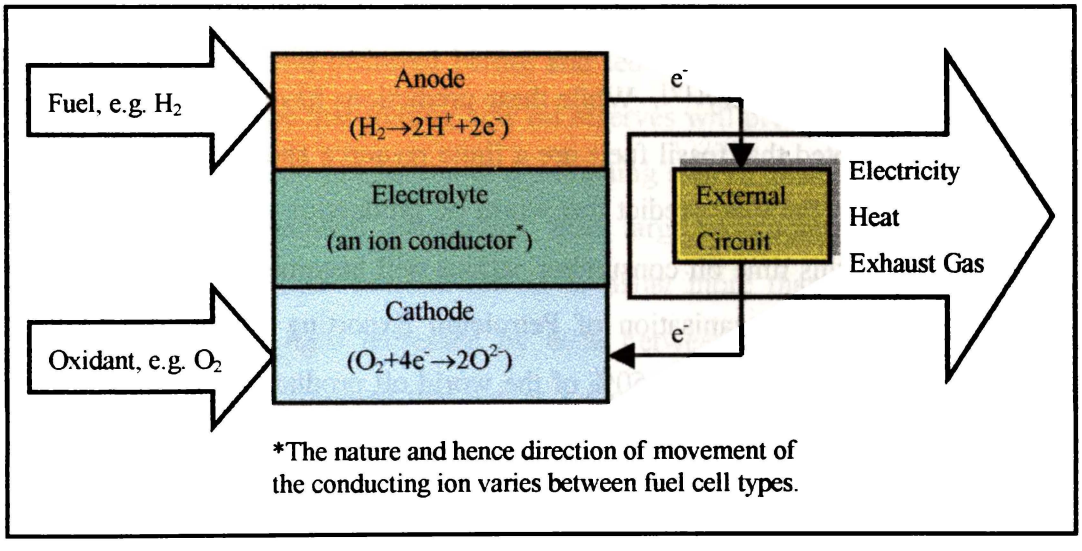

Figure 1.1 A Generalised Fuel Cell.

To obtain usable voltages and currents, individual fuel cells are combined in both parallel and series to create a fuel cell stack. Due to this modular nature, stacks of different power outputs can be easily fabricated by varying the number of component cells a stack contains.

1.3 A Market for Fuel Cells

The science on which fuel cells are based has been known for over 150 years, Sir William Grove first reporting the principles of their operation in 1839[9]. It is only comparatively recently that fuel cell technology has begun to be developed for mainstream applications. Prior to this their use was limited to niche applications such as space exploration, having been used to supply power for all manned space flights since the Gemini Project in 1965[4]. One of the main reasons for the lack of development has been their lack of economic competitiveness. There are a number of factors that mean fuel cells are now becoming commercially viable options[10]. These factors include increasing demand for fuel efficiency[4], a growing awareness of environmental issues[10] and deregulation of the electricity industry[8, 11].

1.3.1 A Call for Fuel Efficiency

The main driving force for increased efficiency is the impending oil crisis. The fossil fuel resources of New Zealand had been predicted to be exhausted by the end of the twentieth century[12]. While these predictions have proved incorrect, it is generally accepted that fossil fuels are a finite resource and will dwindle in the future. Experts in the field predict that world oil production will begin to decline by 2010[13]. At this time oil consuming nations will become more reliant on the members of OPEC (Organisation of Petroleum Exporting Countries) for their needs, as OPEC will have over 50% of the world oil production[14], refer Figure 1.2.

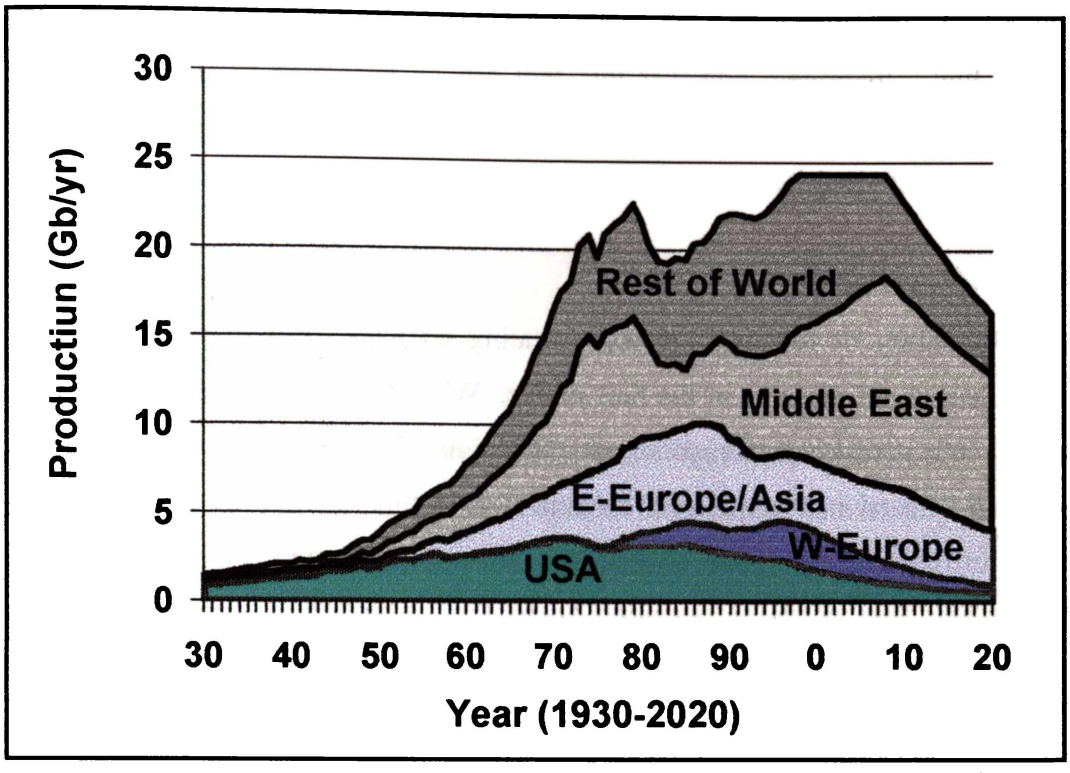

Figure 1.2 World Oil Production[13].
Gb = Giga-barrels = billion barrels.

Dependence on this one group, situated in a politically unstable and unpredictable region of the world, has occurred before and led to the Oil Crisis of the 1970s. While some may argue that finding new oil reserves will prevent this, it will only postpone the inevitable. In addition to diminishing supply, there is also the added factor of increasing demand, particularly from large developing nations such as India and China. Global demand for oil is rising more than 2% a year, with demand expected to have increased by 60% between 2000 and 2020[14]. It becomes increasingly apparent that we, as a race, need to make better use of the remaining oil reserves and for us to begin to seriously considering other, more renewable, forms of energy.

Fuel cells are a promising technology for better utilisation of the remaining fossil fuel reserves, being more efficient than other technologies using fossil fuels as an energy source. Some fuel cells offer the flexibility of operating on a number of fuels, these fuels need not be based on fossil fuels.

Other fuel cells, such as proton exchange membrane fuel cells, will only run on a single fuel - hydrogen, however this fuel can be generated from a number of sources, preferably renewable. This means that fuel cells, as well as better utilising fossil fuels, can continue beyond the current fossil fuel era.

Fuel Reformation[15, 16]

Fuel flexibility of fuel cells, when operating on fuels other than hydrogen, is dependent on reformation of the fuel source. While the overall reaction occurring in fuel cells is that of combustion, refer Equation 1.5 in section 1.3.2, the working reaction utilised is that of electrochemical oxidation of hydrogen. There is a series of reactions that occur to enable a fuel cell to operate using a hydrocarbon fuel. The first of these reactions being the steam reformation of the fuel, Equation 1.3. This is followed by the water-gas shift reaction, Equation 1.4.

$$CH_4 + H_2O \rightarrow CO + 3H_2 \qquad 1.3$$

$$CO + H_2O \rightarrow CO_2 + H_2 \qquad 1.4$$

At elevated temperatures, ca. 650 °C, in the presence of a suitable catalyst, these reactions occur at a sufficient rate to effectively supply hydrogen to the anode. The hydrogen dissociates on the surface of the anode and then, depending on the fuel cell type, either traverses the electrolyte, as H^+, to react at the cathode; or alternatively, reacts with the mobile ions arriving at the anode.

Those fuel cells that operate at elevated temperatures are capable of these reformation reactions within the fuel cell stack, provided the anode has the appropriate catalytic activity. Thus, solid oxide fuel cells and molten carbonate fuel cells are said to be 'internally reforming'. The other fuel cell types, refer section 1.4, due to their comparatively low operating temperatures require an external reforming device to allow them to run on hydrocarbon fuels. The need for an external reformer lowers the efficiency of these fuel cells when running on hydrocarbon fuels, as a portion of the fuel has to be burnt to provide the heat required for the reformation reactions.

1.3.2 Environmental Concern

There is increasing concern over the effect emissions from combustion of carbon containing fuels is having on our environment. There are three compounds of chief concern: Sulphur oxides, SO_x

Nitrogen oxides, NO_x

Carbon dioxide, CO_2

Sulphur and nitrogen oxides are formed during the high temperature combustion conditions found in internal combustion engines. The sulphur is naturally present in fossil fuels, and is generally not removed during the refining process. The nitrogen is taken into the engine with the air intake. Both SO_x and NO_x contribute to the effect known as 'Acid Rain'. Nitrous oxide, N_2O, also contributes to the greenhouse effect. Carbon dioxide is a product of the combustion reaction, refer Equation 1.5 (ethane used as an example).

$$C_2H_6 + 3\tfrac{1}{2}O_2 \rightarrow 2CO_2 + 3H_2O + \text{energy} \qquad 1.5$$

Carbon dioxide is one of a group of gases known as the greenhouse gases, the other gases include water vapour, H_2O, methane, CH_4, nitrous oxide, N_2O and ozone, O_3. These greenhouse gases are essential to life on earth, acting as an insulting layer reducing the loss of heat to the void of space. Since the industrial revolution the amount of carbon dioxide in the atmosphere has been increasing. This is due to the increased burning of fossil fuels, both in industrial processes and by automobiles and also the loss of carbon dioxide sinks, due in major part to deforestation. The increased level of carbon dioxide acts to trap more terrestrial radiation, enhancing the natural greenhouse effect. Evidence suggests that the Earth is now warmer than it has been in nearly 2,000 years[14]. This increase in average global temperature has lead to predictions of rising sea levels and an increase in frequency of catastrophic events such as hurricanes and tornados.

While the overall chemical reaction that occurs in fuel cells is that of combustion, combustion *per se* does not occur. Also many of the fuel cell types operate at temperatures below that associated with combustion.

This means that emissions from fuel cells do not contain NO_x or SO_x gases, traditionally unwanted by-products of combustion, particularly in internal combustion engines. A fuel cell operating on a carbon containing fuel will still emit CO_2. However, for a given amount of generated electrical energy, the amount of CO_2 emitted will be less than if the fuel was used to produce the electricity in some other manner. This is by virtue of the higher efficiencies exhibited by fuel cells. These two factors mean that fuel cells are a 'greener' method of utilising a fuel source.

1.3.3 Electricity Deregulation

Worldwide there is a move to deregulate electricity supply authorities[17]. This could allow for a market in distributed power generation, either with individuals owning their own generation device, or a utility company supplying and maintaining a device situated at the users location. With the supply device located at the users location, transmission losses are minimised and, in the case of fuel cells, heat can be recovered to meet on-site requirements. Distributed generation is also an excellent option in developing nations where there is an increasing demand for electricity but a distinct lack of high cost reticulation infrastructure.
Fuel cells make excellent candidates for decentralised power supply devices for a number of reasons.

1. **Low Maintenance**

   Having no moving parts means that fuel cells are less likely to break down and require less general maintenance[18].

2. **Fuel Flexibility**

   A number of fuels can be used in fuel cells by making use of external reformers or the internal reforming capabilities of some fuel cells.

   This allows the most convenient fuel to be used for a particular situation, this may be bottled propane, biogas generated on-site or a range of other fuels available.

3. Environmental Advantages

Fuel cells are clean running and, while they will emit carbon dioxide if fuelled with a carbon containing fuel, the emissions are lower per unit of electricity produced. Fuel cells are also quiet, having no moving parts or explosive combustion reactions driving a piston.

4. Cogeneration - Combined Heat and Power.

With the incorporation of a heat exchanger the waste heat generated by fuel cells can be used to meet hot water and space heating requirements.

There are some issues that need to be overcome before fuel cells can be realistically considered for general distributed power applications.

1. Cost

Although the price of fuel cells is dropping, they are still far from affordable. It is usually only in situations where other factors are more important than cost that fuel cells have currently found use in localised power generation.

2. New Technology

As fuel cells are an emerging and relatively untried technology, there will be risks for initial adoptees.

3. AC/DC Power Conversion

Fuel cells generate direct current (DC) electricity. As most applications require alternating current (AC) electricity the electricity produced by a fuel cell needs to be passed through an inverter, this reduces the overall efficiency of the system. Alternatively DC appliances would need to be used.

With the number of advantages fuel cells offer and the number of companies actively developing the technology there seems to be a strong future for these devices.

There are still issues that need to be addressed, the main one being lowering their cost, this can be achieved by continued technical advances coupled with mass production.

1.4 Types of Fuel Cells

The defining difference between fuel cell types is the electrolyte material employed.

The most common fuel cell types are as follows:

- Proton Exchange Membrane Fuel Cell (PEMFC)
- Alkaline Fuel Cell (AFC)
- Phosphoric Acid Fuel Cell (PAFC)
- Molten Carbonate Fuel Cell (MCFC)
- Solid Oxide Fuel Cell (SOFC)

1.4.1 PEMFCs

Electrolyte:	Ion conducting polymer
Conducting Ion:	H^+
Operating Temperature:	80°C

Also known as solid polymer electrolyte fuel cells (SPFCs), these fuel cells incorporate a gas impermeable polymer electrolyte, platinum metal catalysts and normally operate on pure hydrogen and air. The electrolyte is an ion exchange membrane with excellent proton conduction. Considerable effort has gone into reducing the amount of platinum these fuel cells require as it is a major component of their cost. This type of fuel cell lends itself to automotive applications[5], possessing a sturdy design, high power densities, low operating temperatures and lacking corrosive liquids. PEMFCs have the disadvantage of being sensitive to carbon monoxide and requiring external reformation of hydrocarbon-based fuels. There are a number of companies[16] developing this technology, and they have been successfully integrated into demonstration vehicles.

1.4.2 AFCs

Electrolyte:	Alkali
Conducting Ion:	OH^-
Operating Temperature:	100-250°C

Employed by NASA in the American space programme, these fuel cells operate on pure oxygen, pure hydrogen and water. The electrolyte is 85% KOH for AFCs operating at high temperature (250°C) or 35-50% KOH for lower operating temperatures. The electrolyte is contained within a matrix, often asbestos. While they can be fabricated from low cost materials and require less platinum than some other types of fuel cell[4], they are sensitive to carbon dioxide contamination. The presence of carbon dioxide causes the formation of K_2CO_3, altering the electrolyte. Many fuelling options involve the on-board generation of hydrogen from a carbon-containing fuel, producing a significant amount of carbon dioxide. This carbon dioxide intolerance coupled with the high cost of the systems has meant that, while AFCs were intended for widespread use, they never achieved commercialisation. Work is currently underway to re-address these systems.

1.4.3 PAFCs

Electrolyte:	Phosphoric Acid
Conducting Ion:	H^+
Operating Temperature:	200°C

Of the different fuel cell types, PAFCs are the most developed and the closest to true commercialisation. The 100% phosphoric acid electrolyte is retained in a silicon carbide matrix. A number of units have been installed at locations in North America and Japan[11]. While the technology has been reasonably well developed, the fuel cells suffer from a number of drawbacks. As well as being bulky, the electrolyte is hot phosphoric acid, which causes problems with corrosion and stack life. The operating temperature means that cogeneration is only just feasible, in that hot water and space heating can be produced.

The cost of PAFCs has been stationary for a number of years at about $US4,000 per kilowatt[11]. This value is approximately three times the cost required for the cells to be considered competitive. This has led some observers to consider the technology not commercially viable[11].

1.4.4 MCFCs

Electrolyte:	Molten carbonate salt
Conducting Ion:	CO_3^{2-}
Operating Temperature:	650°C

These fuel cells have a molten alkali carbonate electrolyte contained within a $LiAlO_2$ ceramic matrix supplied with air and carbon dioxide at the cathode. This fuel cell type has the advantage of being able to run on hydrocarbons without the need for external reforming. There are still a number of problems to be fixed with the MCFC system. A 2-megawatt system developed by Energy Research Corporation operated successfully for 3000 hours, however it rarely produced more than 1 megawatt, half its rated capacity[11]. MCFCs are still being pursued by a number of companies.

1.4.5 SOFCs

Electrolyte:	Solid Oxide Ceramic
Conducting Ion:	O^{2-}
Operating Temperature:	800-1000°C

The first recorded SOFC was operated by Baur and Preis in 1937[19]. Nernst discovered solid oxide electrolytes decades earlier in 1899[20], however he did not initially apply them in electricity generation devices. Rather he applied them in the production of light using a device later called the Nernst Glower.

With the high operating temperature and a suitable catalytic anode these fuel cells are capable of internally reforming virtually any carbon-based fuel. The high operating temperature, while allowing the option of cogeneration, limits the materials that can be used in the balance of plant.

As the materials studied in this thesis are intended for use in SOFCs, this type of fuel cell will be discussed in more detail in the following section.

1.5 Solid Oxide Fuel Cells (SOFCs)

Ceramic fuel cells are the most common type of SOFC. Ceramic fuel cells have a number of advantages over other types of fuel cells, refer Table 1.1.

Table 1.1 Advantages and Disadvantages of Ceramic Fuel Cells[21].

Advantages	Disadvantages
❖ Does not use precious metals, such as Pt. ❖ No liquids involved in the cell. ❖ Electrolyte composition does not change with operation. ❖ High operating temperature: - promotes rapid reaction kinetics - allows for internal reforming of fuels - produces high quality waste heat for co-generation ❖ All the components are solid, allowing for fabrication of different shapes.	❖ Ceramics can be difficult to process. ❖ If the cell cracks, possible explosive mixing of H_2 and O_2/air. ❖ High operating temperature: - creates problems with differing thermal expansions of components - limits the materials used in the balance of plant ❖ Can be fragile, unlike PEMFCs.

1.5.1 Components of an SOFC

SOFCs consist of 3 components, anode, electrolyte and cathode. When cells are combined to form a stack a fourth material is also used to act as an interconnect between individual cells. The interconnect acts to mechanically and electrically connect the component cells.

Each component has a specific function in the fuel cell and must meet a number of requirements[7]. Some of these requirements are component specific, while others apply to all components, refer Table 1.2.

Table 1.2 SOFC Cell Component Requirements[7, 21]

Requirements of all components: ❖ Chemically inert with respect to the other cell components under realistic operating conditions and cycles. ❖ Similar coefficients of thermal expansion to minimise thermal stresses and potential loss of mechanical integrity. ❖ It is also desirable for the components to have a high strength and toughness, as well as being easy to fabricate.	
Anode requirements:	❖ Porous to allow gas diffusion. ❖ High electronic conductivity*, >100 Scm^{-1} (can be either purely electronic or mixed ionic/electronic conductivity). ❖ Stable under reducing environments.
Cathode requirements:	❖ Porous to allow gas diffusion. ❖ High electronic conductivity, >100 Scm^{-1}. ❖ Stable under oxidising environments.
Interconnect requirements:	❖ Fully dense to prevent mixing of the gas streams. ❖ High electronic conductivity. ❖ Stable under both oxidising and reducing environments.

* Conductivity has the units of Siemens per metre (Sm^{-1}), though Siemens per centimetre, (Scm^{-1}) is commonly used. Conductivity is the reciprocal of resistivity (Ωm), hence 1 S = 1 Ω^{-1}.

Requirements of SOFC electrolytes are detailed in Section 1.6.1.

The individual components of an SOFC may be used in fabricating a number of different SOFC designs.

1.5.2 Major SOFC Designs

The two SOFC designs being most actively developed use either tubular or planar configurations.

1) Planar

Also termed flat-plate, this design has the cell components (anode/electrolyte/cathode) as thin flat plates sandwiched between interconnect plates, refer Figure 1.3. The interconnect, having ribs on both sides, forms gas channels and serves as a bipolar gas separator connecting the anode and cathode of adjoining cells. Having a flat-plate design allows several different ways of ducting the gases in and out of the cell.

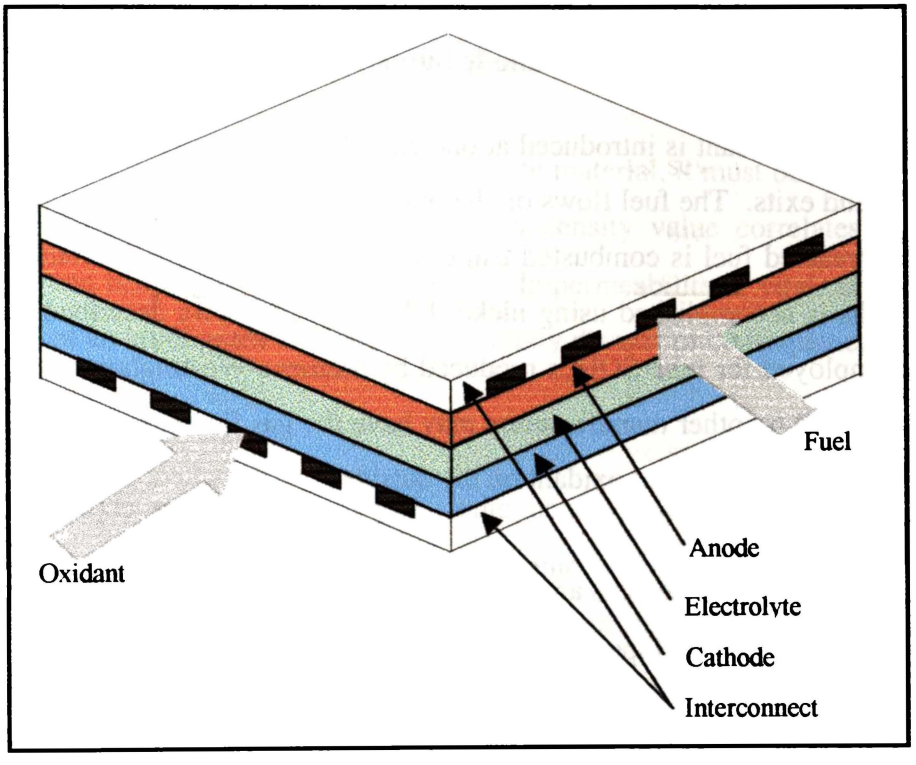

Figure 1.3 Schematic of a Planar SOFC Cell Configuration.

2) Tubular

The tubular design is considered by some to be the most advanced because of advantages such as ease of sealing and high thermal shock resistance[22]. In early designs cell components were thin layers on an inert, porous support tube.

More recently, the support tubes have been fabricated from either the cathode material[23], refer Figure 1.4, or the anode material[22].

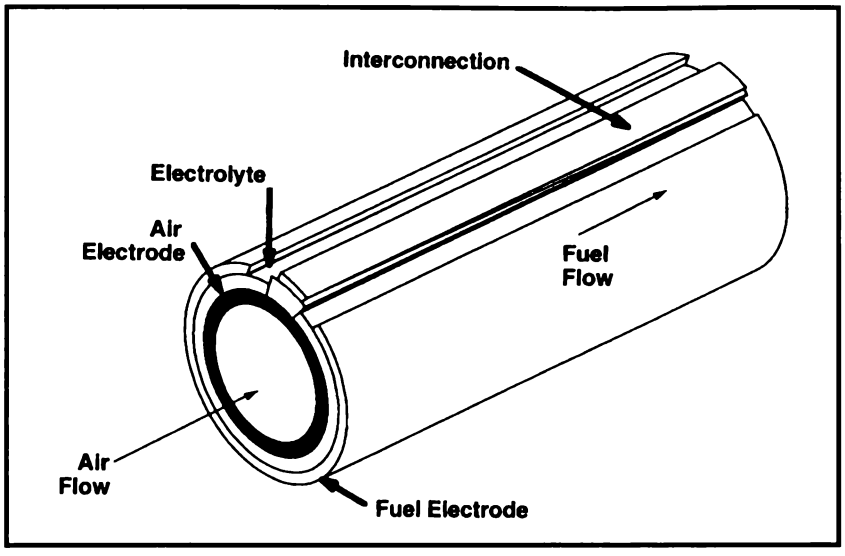

Figure 1.4 Schematic of a Cathode Supported Tubular SOFC.[23]

In operation, the oxidant is introduced at one end of the tube, traverses the length of the tube and exits. The fuel flows on the outside of the support tube, at the exit point the unreacted fuel is combusted using the oxidant stream. Interconnection between cells is accomplished using nickel felt. The gas flows described above are those employed for tube SOFCs produced by Siemens-Westinghouse; tubular SOFCs produced by other manufacturers may have the gas flows reversed, that is fuel flowing on the inside and oxidant on the outside.

While planar and tubular designs are the most widespread, there are also a number of other designs being developed by groups around the world[23, 24].

1.6 SOFC Electrolytes

The single most important component of a SOFC, the electrolyte, is usually a metal oxide capable of ionic conduction, specifically oxide ion conduction. The crystallographic structure associated with most oxygen ion conductors is the fluorite structure or a related structure.

As with the other components, the electrolyte material must fulfil a number of requirements.

1.6.1 Requirements of SOFC Electrolytes[7, 21, 25, 26]

The five main requirements an electrolyte must meet are discussed below.

1) Density

Whichever material is chosen as the electrolyte material, it must be sinterable to at least 96% of the theoretical density. This density value correlates to closed porosity and hence gas impermeability[27]. Impermeability is vital, as mixing of the oxidant and fuel gases could have potentially disastrous consequences.

2) Conductivity

The electrolyte must posses a high ionic conductivity, σ_i=0.05 Scm^{-1} at the proposed operating temperature. The electronic conductivity of the electrolyte should be kept to a minimum to avoid short-circuiting the fuel cell. In practice this means having an ionic transference number, t_i (refer Equation 1.6), approaching unity.

$$t_i = \sigma_i/\sigma_T \qquad 1.6$$

t_i = ionic transference number

σ_i = ionic conductivity

σ_T = total conductivity

3) Stability

The electrolyte needs to be stable under the operating conditions employed and also during the heat up portion of its operation. This means that the electrolyte should be capable of tolerating both oxidising and reducing conditions and exhibit no detrimental phase changes during thermal cycling.

4) Chemical Compatibility

There should be no chemical reaction between the electrolyte and the other fuel cell components under the expected operating conditions and also during cell fabrication. Such reactions could produce second phases that can adversely affect the fuel cells performance either by reducing the mechanical integrity or degrading the performance of the cell.

5) Thermal Expansion Compatibility

The thermal expansion of all components should match as closely as possible to minimise cracking and delamination. Steele[28] has stated that a thermal expansion mismatch of up to 10% can be tolerated. The coefficient of thermal expansion should also remain constant despite changes in oxygen partial pressure during operation.

1.6.2 Currently Used Electrolyte Materials

Currently, the most commonly used electrolyte material is doped zirconia. The dopant usually employed is yttria, to form yttria stabilised zirconia, YSZ. Zirconia is doped because it only possesses the oxygen ion conducting cubic fluorite phase at high temperatures, refer Figure 1.5.

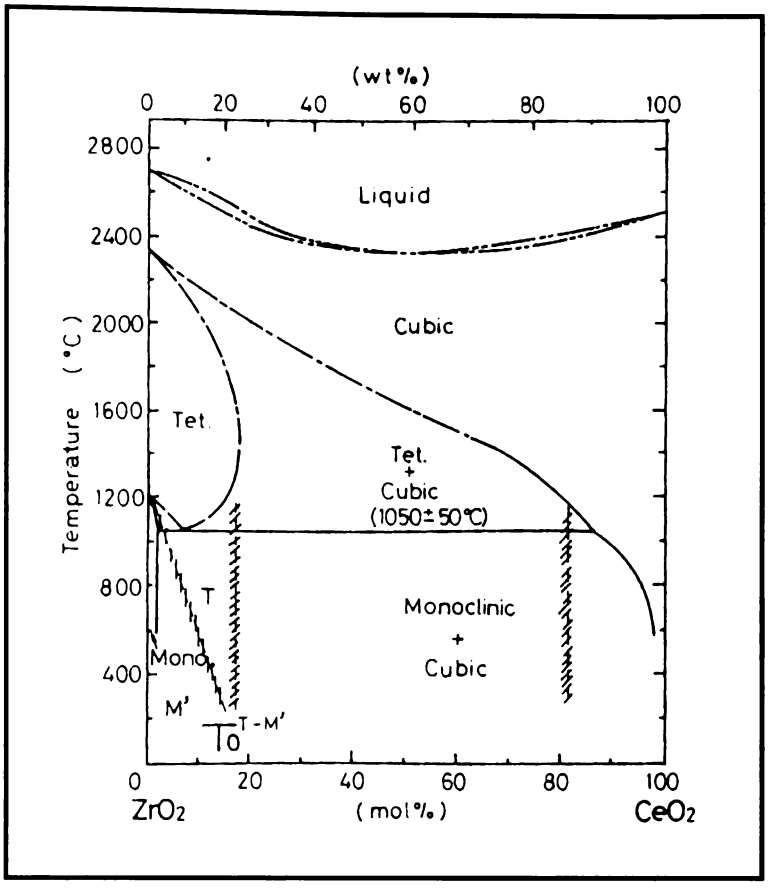

Figure 1.5 Phase Diagram of Zirconia and Ceria[29].

The phase changes zirconia undergoes prior to attaining the cubic phase have large associated volume changes, particularly the monoclinic to tetragonal transformation[30]. These volume changes cause mechanical integrity problems, particularly on cooling through the tetragonal to monoclinic phase boundary, where a 4% volume increase is observed. These detrimental phase changes can be eliminated by doping with an aliovalent ion, which acts to stabilise the cubic phase so that it exists at all temperatures below the melting point. An aliovalent ion is an ion with a formal charge differing from that of the host ion; in the course of this work aliovalent will always refer to a cation of lower charge than the host. The addition of aliovalent ions also has the added benefit of enhancing the oxygen ion conductivity by introducing oxygen ion vacancies, (refer Figure 1.6).

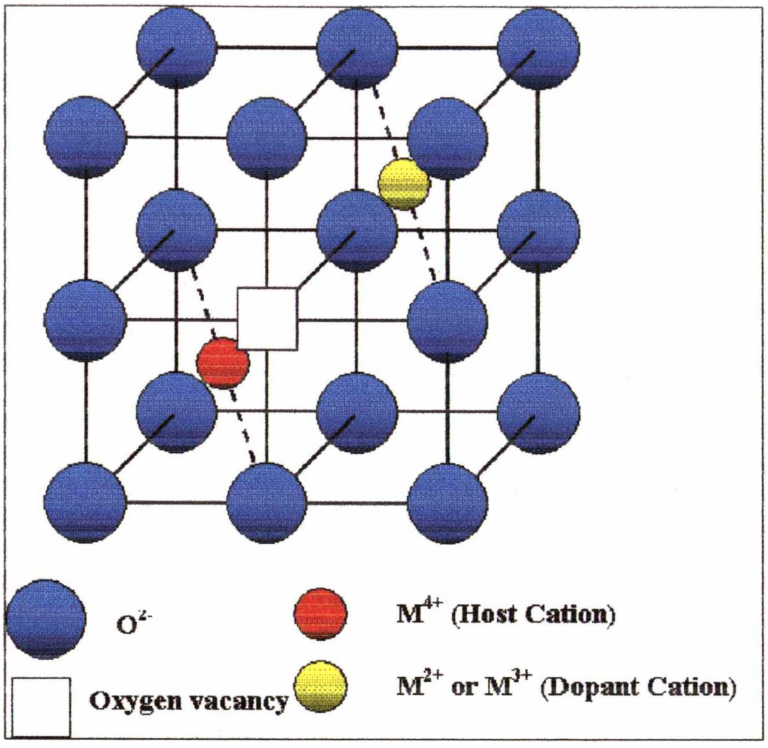

Figure 1.6 Doped Fluorite Structure.

While the addition of aliovalent ions stabilises the cubic fluorite phase of zirconia down to room temperature, the material must be operated at high temperatures, typically 900-1000 °C, to obtain usable power densities.

1.6.3 Conduction Mechanism

The stabilisation of the fluorite structure of zirconia, by direct substitution of an aliovalent ion for Zr^{4+} in the host lattice, leads to the formation of lattice defects. Lattice defects are formed to preserve the electroneutrality of the system. There are a number of plausible models for the structural defect formed. It has been well established that an oxygen vacancy model applies to fluorite-type oxygen conductors[31, 32]. The formation of oxygen vacancies is detailed in Equation 1.7, using yttria and calcia as examples of trivalent and divalent dopants in zirconia. The equations utilise Kröger-Vink notation, refer Appendix One.

$$Y_2O_3 \xrightarrow{ZrO_2} 2Y'_{Zr} + V_O^{\bullet\bullet} + 3O_O^x \qquad 1.7$$

$$CaO \xrightarrow{ZrO_2} Ca''_{Zr} + V_O^{\bullet\bullet} + O_O^x$$

The introduction of oxygen vacancies increases the conductivity of the material by increasing the concentration of the mobile species[33], C_i, (refer Equation 1.8).

$$i_o = \sigma_i E = qC_i v_d \qquad 1.8$$

i_o = current density

σ_i = ionic conductivity

E = applied electric field

q = charge of the mobile species

C_i = concentration of mobile species,

in this case $V_O^{\bullet\bullet}$

v_d = drift velocity

Conduction in oxygen ion conductors occurs by ion hopping, termed random walk, where ions jump from one ion vacancy to the next. Though it is the ions moving the mechanism is considered one of vacancy migration[33]. Not only is the conductivity of a material dependent on the concentration of the mobile species, it is also dependent on the charged species mobility.

As the ions move via a diffusion mechanism the carrier mobility, μ, will obey the Einstein relationship, Equation 1.9.

$$\mu \equiv {v_d}/{E} = {qD}/{kT} \qquad 1.9$$

D = diffusion coefficient

k = Boltzmann's constant

T = absolute temperature

By combining Equations 1.8 and 1.9 a form of the Nernst-Einstein Equation is obtained, Equation 1.10.

$$\sigma_i = \frac{C_i q^2}{kT} D_i \qquad 1.10$$

From Equation 1.10 it can be seen that if a value for the diffusion coefficient of the mobile ion in the lattice can be measured then it is possible to calculate the conductivity.

The diffusion coefficient is defined in Equation 1.11.

$$D = D_o \exp\left(-\Delta G_m / kT\right) \qquad 1.11$$

ΔG_m = motional free energy

D_o = diffusion pre-exponential factor

Motional free energy is given in Equation 1.12.

$$\Delta G_m = \Delta H_m - T\Delta S_m \qquad 1.12$$

H_m = motional enthalpy

S_m = motional entropy

Substitution of Equations 1.9 and 1.11 into Equation 1.8 yields Equation 1.13[34]. This Arrhenius type equation is frequently utilised in investigations of electrochemical properties of oxide ion conductors.

$$\sigma_i = \frac{A}{T}\exp\left(-E_a / kT\right) \qquad 1.13$$

where:

$$A = C_i \frac{q^2}{k} D_o \exp\left(\frac{\Delta S_m}{k}\right) \qquad 1.14$$

and $E_a = \Delta H_m$ 1.15

Effect of Partial Pressure

The defect type associated with pure zirconia, and also pure ceria, is that of anti-Frenkel defects[31]. Anti-Frenkel defects yield anion vacancies, $V_O^{\bullet\bullet}$, and interstitial anions, O_i''. This defect type is also present in doped zirconia and ceria, although the number of defects introduced through doping are generally far in excess of these intrinsic defects. However in extremes of oxygen partial pressure intrinsic defect equilibria begin to have a noticeable affect on the conduction of the materials in question, refer Figure 1.7.

Electroneutrality requires:

$$h^{\bullet} + 2[V_O^{\bullet\bullet}] = e' + 2[O_i'']$$

Frenkel defects give:

$$O_O^x \leftrightarrow V_O^{\bullet\bullet} + O_i''$$

Therefore, the equilibrium constant, K, is given by:

$$K = [V_O^{\bullet\bullet}][O_i''],$$

when the concentration of oxygen anions is large compared with the number of defects at constant temperature and pressure.

Extremes in partial pressure have the following effects:

High P_{O_2} - predominant defects are interstitial anions and positive holes.

$$\tfrac{1}{2}O_2 = O_i'' + 2h^{\bullet}$$

Hence:
$$K = \left(\frac{[O_i''][h^{\bullet}]^2}{P_{O_2}^{\frac{1}{2}}} \right)$$

If $[O_i'']$ is large and approximately constant then: $h^{\bullet} \propto P_{O_2}^{\frac{1}{4}}$

Low P_{O_2} - predominant defects are oxygen vacancies and free electrons.

$$O_O^x = \tfrac{1}{2}O_2 + V_O^{\bullet\bullet} + 2e'$$

Hence:
$$K = [V_O^{\bullet\bullet}][e']^2 P_{O_2}^{\frac{1}{2}}$$

if $[V_O^{\bullet\bullet}]$ is large and approximately constant then: $e' \propto P_{O_2}^{-\frac{1}{4}}$

Figure 1.7 Effect of Oxygen Partial Pressure on Defect Concentrations.

It can be seen from the equations in Figure 1.7 that at sufficiently high oxygen partial pressure the material will exhibit p-type conduction due to the formation of positively charged 'holes', $h^{\bullet}$. At sufficiently low oxygen partial pressures the material will exhibit n-type conductivity due to the formation of free electrons, $e^{/}$. Between these two extremes conductivity is predominantly ionic in nature. The threshold partial pressures at which these conductivities manifest depend on the material in question and bound the electrolytic domain, refer Figure 1.8.

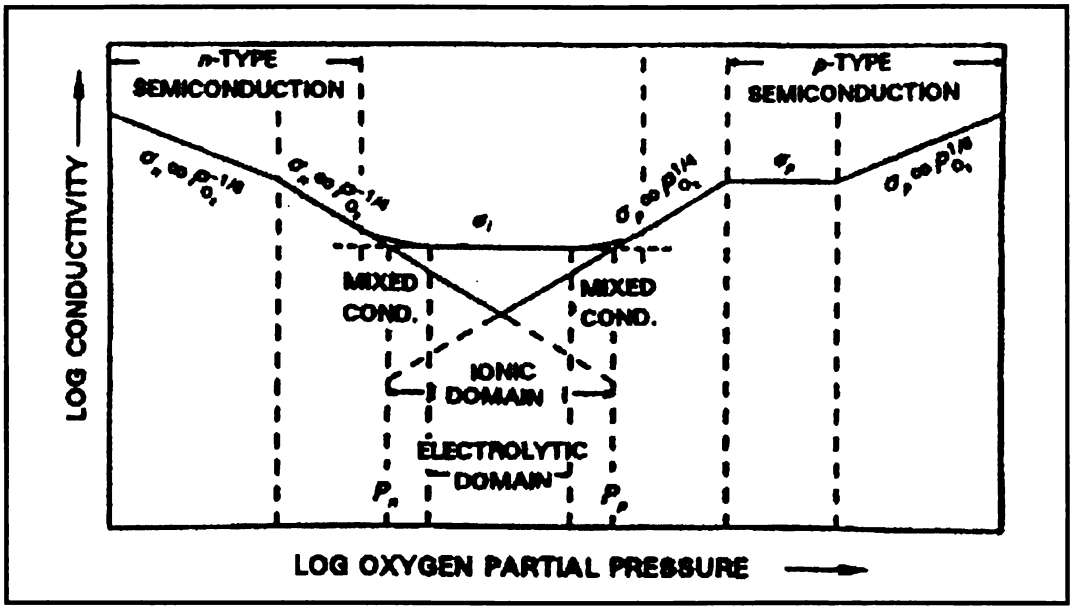

Figure 1.8 Effect of Oxygen Partial Pressure on Conductivity of MO_2 with predominantly Frenkel Defects[35].

The electrolytic domain boundary, EDB, values are determined from the points where ionic conductivity is equal to one hundred times the value of either the p-type or n-type conductivity. The ionic domain of a material is bounded by the points where ionic conductivity is equal to the p-type or n-type conductivity. Figure 1.9 shows typical electrolytic domain boundaries for a number of fluorite materials.

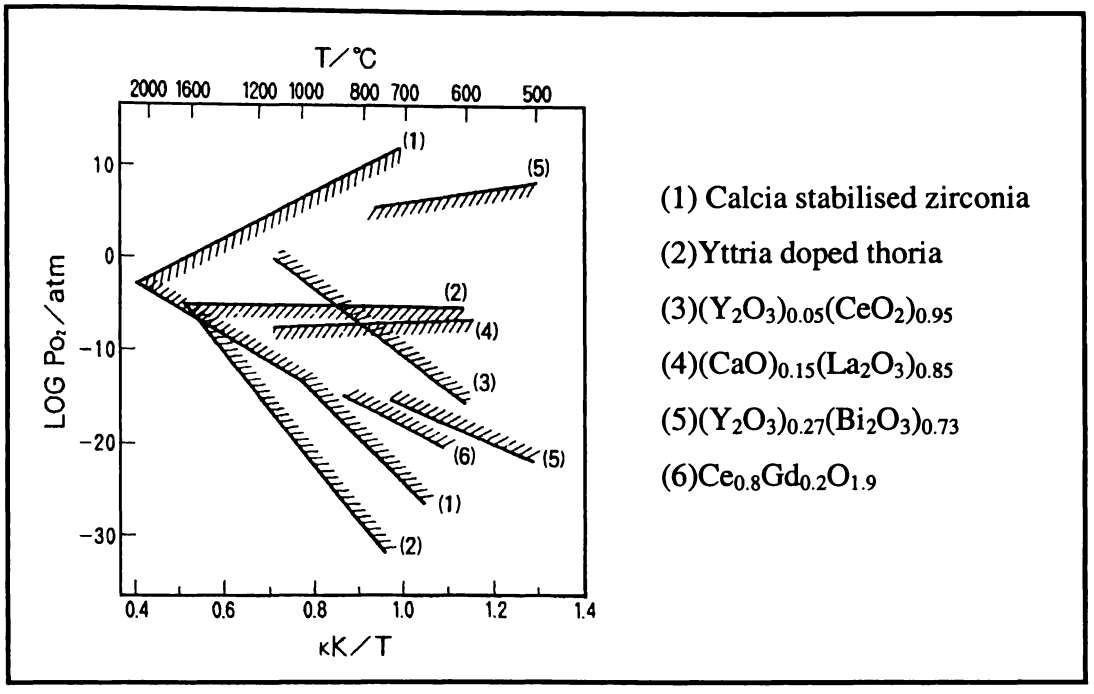

Figure 1.9 Electrolytic Domains for Various Fluorite Oxides[36].

Channel Conduction

An alternate conduction mechanism has been proposed by Kröger[37] whereby oxygen vacancies migrate within electrically neutral defect clusters, defect clusters are discussed in section 1.7.3. With high levels of dopant, adjacent defect clusters begin to come into contact with one another, forming continuous channels through the crystal[38]. Assuming that vacancy migration along these channels has a lower activation energy than outside the channels, then the ionic transport reduces to percolation theory.

In addition to base material, the dopant employed and partial pressure, the conductivity of oxide ion conductors is also affected by the presence of impurities and fabrication methods employed in manufacture[39]. These generally contribute to what is known as the 'Grain Boundary Effect'.

1.6.4 Grain Boundary Effects

It has been found[40-49] that the total resistance of a solid oxide electrolyte can be separated into two components, that attributed to the lattice or grains of the material and that of the grain boundaries. A number of researchers[47, 50] state that lattice conductivity is a materials property, being a function of composition of the electrolyte, the main factors being dopant type and concentration. The grain boundary resistance has been determined to be strongly influenced by processing parameters and the presence of impurities[46, 51]. The grain boundary resistance can be up to three orders of magnitude higher than that of the lattice[46].

There are a number of sources for this 'grain boundary effect'. The main effect is due to the presence of impurities and secondary phases at the grain boundary[21]. Impurities tend to segregate at grain boundaries and at external surfaces during processing and heat treatment[21, 30, 52, 53]. Impurity segregation, particularly of silica, is often due to the formation of a liquid phase during sintering, which allows the flow of silica around the non-melting particles. Of the impurities identified at the grain boundary, silica has a significant effect with respect to lowering the conductivity.

Based on microscopic examination, the presence of a silica impurity causes the formation of a glassy insulting phase at the grain boundaries. An insulating phase may either be continuous or segregated, that is discontinuous[54]. It has been suggested[41, 55] that it is possible to distinguish between these two options by comparing activation energy values. If the activation energy for grain boundary conductivity is the same as that of the lattice then any grain boundary phase is non-conducting and does not fully surround the grains. The grain boundary phase merely acts to limit current flow to unblocked regions where there is direct grain-grain contact[56]. Where the activation energy attributed to the grain boundary is higher than that of the lattice then the grain boundary phase is more likely to be a continuous phase of high resistance[55].

Continuous boundary phases are uncommon in ceramic materials[47] and research has shown that while the activation energy for grain boundary conductivity can be higher than that of the lattice, it does not show any variation with differing impurities[41]. If the boundary phases were truly continuous the activation energy would vary when the composition was varied, the fact that it does not[41] lends credence to a segregated grain boundary phase.

The form the impurity phase takes influences the choice of conduction model. If there is a continuous insulating phase, Figure 1.10(a), a 'blocking' model is appropriate. If however the grain boundary phase is segregated, Figure 1.10(b), then a 'restriction' model is more applicable.

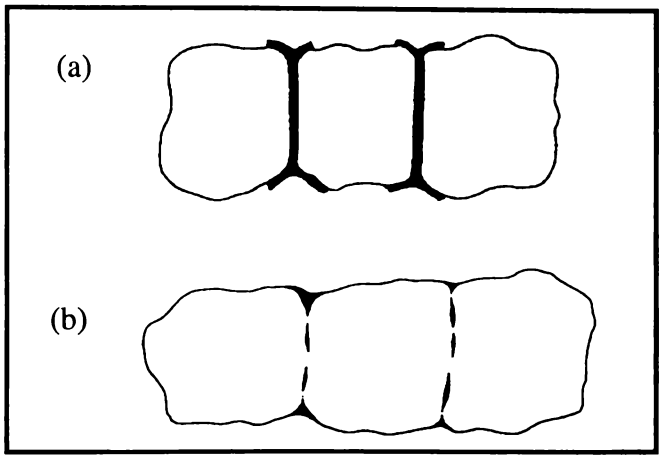

Figure 1.10 Models of Grain Boundary Phases[41].

It has also been suggested[51] that a restriction model is more appropriate for small, sub-micron, grained samples. The reasoning being that a sub-micron grain structure implies that there is a greater area of grain boundaries; given a fixed amount of impurity there would be insufficient material to form a continuous layer at all grain boundaries. Gerhardt and Nowick[46] have shown that the grain boundary effect can be significantly reduced by minimising the amount of silica present in the sample. However, even if materials could be guaranteed silica free, there would still be a grain boundary effect of some sort, though it would have a smaller magnitude[57]. In any polycrystalline material there will be an intrinsic grain boundary resistance.

This intrinsic grain boundary resistance is attributed to a number of factors, these being: imperfect intergrain alignment, pores and solute segregation.

Solute Segregation

Dopants in solid solution may segregate to the grain boundaries. There are a number of reasons for a solute to segregate to the grain boundary. The most important are strain energy relaxation and electrostatic potential. Incorporation of a dopant ion within a crystal lattice can produce an associated strain energy. The segregation of the dopant ion to a grain boundary, where it can be more readily accommodated[58] acts to relieve this strain energy. The strain energy is strongly influenced by the size mismatch between dopant and host[54]. This may be reason why dopants that closely match the radius of the host ion give higher conductivities (covered in section 1.7.3). Also solubility limits are a consideration when considering segregation to grain boundaries[59].

The intrinsic grain boundary effect can also be attributed to space charge separation. Frenkel[60] first proposed the existence of a space charge near lattice discontinuities, such as grain boundaries and free surfaces. At thermodynamic equilibrium the grain boundaries of an ionic crystal may carry an electric potential resulting from the accumulation of charged point defects. The charge excess is due to the different free energies of formation of cation and anion vacancies in pure ionic crystals[54]. In ionic materials lacking electronic charge carriers, low concentrations of aliovalent ions may diffuse in response to the excess charge at grain boundaries. This can lead to segregation of the dopant ion and formation of a space charge region at grain boundaries, see Figure 1.11. Computer simulations have shown that it is energetically favoured to have oxygen vacancies, $V_O^{\bullet\bullet}$, within grain boundaries rather than trying to lock in the relatively large oxygen anions[61]. To maintain long-range electroneutrality the negatively charged dopant ions, M'_{Ce}, segregate to the grain boundaries.

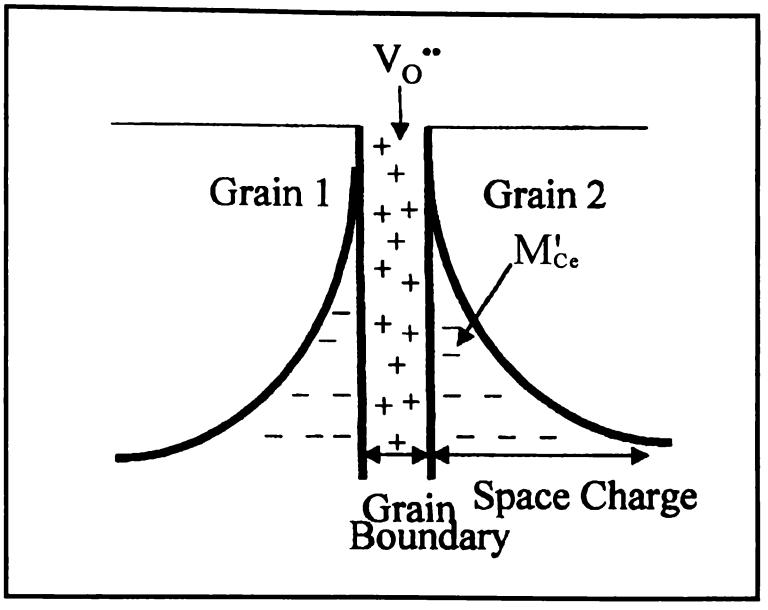

Figure 1.11 Diagram of Space Charge Effect in Doped Ceria[51].

As oxygen vacancies attempt to traverse this space charge region they are more likely to be trapped and form a defect associate with M'_{Ce}. This contributes to the grain boundary resistance of polycrystalline samples even when impurities are absent[51].

1.6.5 Other Oxygen Ion Conductors

It is generally accepted that the operating temperatures of SOFCs need to be lowered from the 900-1000 °C currently employed for zirconia based electrolytes[36, 48, 62-69]. To achieve this, ohmic losses must be reduced[70]. There are two ways in which this could be accomplished[71]. One way is by lowering the specific resistance of the electrolyte by employing a thinner electrolyte, allowing existing electrolytes to be run at lower temperatures. Thin electrolytes however are no longer self-supporting and pose problems with fabrication[72]. Alternatively, employing an electrolyte with higher oxygen ion conductivity would allow for lower operating temperatures.

As listed in Table 1.3, there are materials other than doped zirconia that conduct oxygen ions. Of the materials listed, the ones that have attracted the most attention as replacements for zirconia are the doped cerias, the perovskites and more recently the pyrochlores. Doped bismuth oxide has also been investigated as an electrolyte and as part of layered electrolytes[73].

Table 1.3 Materials Possessing Oxygen Ion Conductivity.[21, 35, 74-76]

HfO_2	- Must be doped to stabilise the conducting cubic fluorite phase. - Low ionic conductivity. - Narrow electrolytic domain.
CeO_2	- Possesses the conducting cubic fluorite phase at all temperatures, only reason for doping is increasing the ionic conductivity. - Suitably doped ceria has a higher ionic conductivity than YSZ. - Susceptible to reduction at low oxygen partial pressures.
ThO_2	- Possesses the conducting cubic phase at all temperatures, only reason for doping is increasing the ionic conductivity. - Even when doped, thoria's ionic conductivity is too low for practical applications. - Possible problems due to radioactivity. - Exhibits p-type conductivity at higher oxygen partial pressures.
Bi_2O_3	- δ-Bi_2O_3 has an ionic conductivity that is among the highest known for solid state conductors. - Doping stabilises the δ-phase but reduces the conductivity. - Is easily reduced at low oxygen partial pressures.
Perovskites, ABO_3	- $LaGaO_3$ doped with appropriate dopants has a conductivity approximately three times higher than YSZ. - Stable at low oxygen partial pressures.
Pyrochlores, $A_2B_2O_7$	- Have a relatively high oxygen ion conductivity prior to doping and with doping this is increased. - Negligible electronic conductivity over a wide range of oxygen partial pressures and temperatures.

1.7 Doped Ceria Electrolytes

Doped ceria has been proposed as an electrolyte for use in fuel cells. After δ-Bi_2O_3 and doped Bi_2O_3 it exhibits the highest conductivity of all the oxide ion conducting doped binary oxides, refer Figure 1.12.

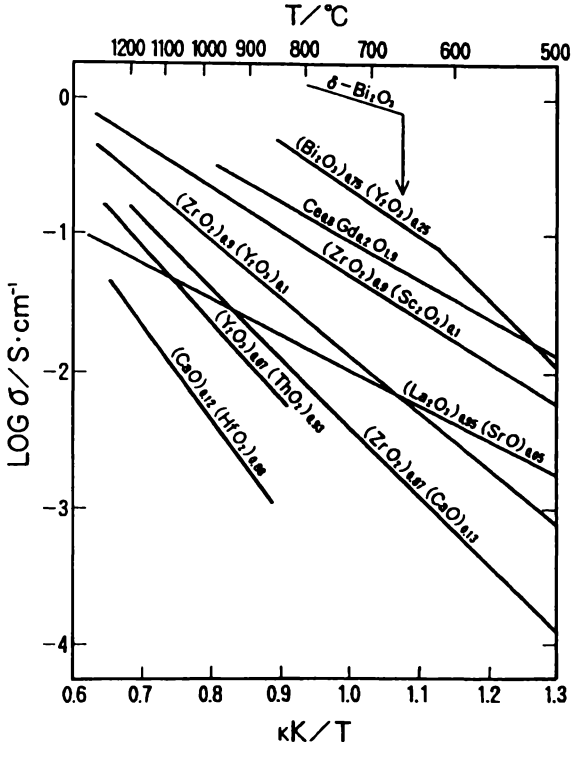

Figure 1.12 Ionic Conductivity of Fluorite Oxides[77].

*Reciprocal temperature units are K^{-1}x1000 or kilo(K^{-1})

The reason that the bismuth-based oxides are not employed is their restricted ionic domains, δ-Bi_2O_3 being reduced to Bi metal at $P_{O_2} \leq 10^{-8}$ Pa[21]; it is also known to be too mechanically weak for most applications. Ceria, doped with calcia, yttria or rare earth oxides, is an excellent oxygen ion conductor, with higher conductivity and a lower activation energy for ionic conduction than doped zirconia[21].

1.7.1 Benefits and Drawbacks of Ceria as a Solid State Electrolyte

Ceria-based electrolytes have been studied as alternatives to zirconia-based electrolytes. The main advantage that ceria electrolytes have over their zirconia counterparts is a higher ionic conductivity. Doped ceria exhibits higher conductivities at 700 °C than does doped zirconia at 700 °C[66]. Many problems associated with the high operating temperature required for zirconia would be solved by using ceria in place of zirconia (refer to the following list).

Effects of Lowering SOFC Operating Temperature:

- At high temperatures, many reactions occur at the interfaces between different cell components[78, 79]. By lowering the operating temperature inter-component reactions could be minimised[36].
- As the generation of electricity from gaseous fuels is a non-cyclic process, the lower the operating temperature the higher the thermodynamic efficiency[67].
- The high operating temperature of zirconia-based fuel cells severely restricts the choice of metallic materials that can be used in the stack and the balance of plant[43]. This has meant that most stacks have been entirely ceramic. Stacks constructed solely of ceramics are difficult to scale up to cost effective sizes[66]. By lowering the temperature to 700 °C metallic components could be used in the stack as interconnects[69].
- Reduction of the operating temperature would increase the stack lifetime and lower the overall cost[68], as well as reducing the maintenance costs[65].

In addition to lowering the operating temperature of the stack, the use of ceria-based electrolytes would allow more flexibility in the selection of electrode materials[65]. For example the high conductivity perovskite type cathode $La_{0.6}Sr_{0.4}Co_{0.98}Ni_{0.02}O_3$ undergoes a reaction with zirconia at 1000 °C to form other oxide phases, meaning the lower conductivity material, $La_{0.6}Sr_{0.4}MnO_3$, has to be used as a cathode instead[80]. However, when the cobalt-based oxide is heated with ceria there is no observed reaction below 1200 °C[80].

The use of ceria-based electrolytes also seems to enhance the anodic reaction of nickel-based anodes, producing a higher cathodic polarisation conductivity. It is thought that the oxide materials accelerate the activation process or the mass transfer processes[80].

Although there are advantages of using ceria in place of zirconia-based electrolytes, there are also disadvantages.

- Ceria is a more expensive material than zirconia.
- Ceria is a mixed conductor under normal conditions, with an ionic transference number, t_i, less than unity. This being due to the reduction of a portion of the Ce^{4+} ions to Ce^{3+}, pure ceria more correctly being $CeO_{2-\delta}$. While some doping systems are less reducible than others, reduction still poses a problem at the fuel side of the electrolyte where low oxygen partial pressures are found[43].
- Ceria is mechanically weaker than zirconia.

Mixed Conductivity in Ceria

Pure ceria is a mixed conductor, $t_i = 0.4$[81], with ionic and n-type conductivity under standard conditions. The addition of suitable dopant ions can increase t_i to almost unity up to 800 °C[81]. However, in doped ceria, at higher temperatures or low oxygen partial pressures, reduction of Ce^{4+} to Ce^{3+} still occurs, with subsequent generation of electronic charge carriers. The introduction of electronic conduction in the electrolyte is detrimental to fuel cell performance[82], acting to short circuit the cell. While the addition of dopant ions increases the oxygen ion conductivity a number of researchers have found that the doped materials are more reducible than pure ceria[83-85]. Not all dopants increase the reducibility of ceria to the same extent. Eguchi *et al.*[86] found that generally those dopants that give the greatest ionic conductivity also produce the least reducible materials. Mogensen[87] found that as dopant concentration is increased so was the resistance to reduction.

1.7.2 Ceria as an SOFC Electrolyte

Ceria based electrolytes have been used in a number of experimental fuel cells. Zheng[69] investigated the differences between self-supporting (~300 μm) and thick film (5-10 μm) gadolinia doped ceria electrolytes. The two electrolytes were tested in the fuel cell set up:

Air, $La_{0.4}Sr_{0.6}Co_{0.2}Fe_{0.8}O_3|Ce_{0.9}Gd_{0.1}O_{1.95}|$Ni/YSZ, fuel, run at 650 °C.

It was found that the self-supporting electrolyte produced a higher terminal voltage (0.888 V compared with 0.67 V for the thick film). However, due to its thickness, the self-supporting electrolyte had a higher cell resistance (resistance of 4.1 Ωcm^2 compared to 0.8 Ωcm^2 for the thick film). This higher resistance meant that the cell incorporating the self-supporting electrolyte, produced a lower maximum power output (45 mW/cm^2 compared to 125 mW/cm^2 for the thick film). There was no mention of reduction of the ceria electrolyte at the anode.

Eguchi[86] investigated the use of doped ceria electrolytes in an experimental cell with the configuration O_2, $Pt|(CeO_2)_{0.8}(MO_{1.5})_{0.2}|Pt$, H_2O+H_2, where M=Gd, Sm or Y. A theoretical open circuit voltage under the experimental conditions was calculated at 1.07 V. The observed open circuit voltages for M=Gd, Sm and Y were 0.82, 0.82 and 0.72 V respectively. The difference between the theoretical and observed open circuit voltages is attributed to the reduction of the doped ceria under the hydrogen atmosphere leading to electronic conduction. This means that the ionic transference number was less than unity.

Coating the surface of the ceria electrolyte closest to the anode with a thin layer of yttria stabilised zirconia, YSZ, prevents the ceria from being reduced[86] as YSZ is less reducible than ceria. In order to maintain a low overall resistance, the YSZ layer needs to be as thin as possible while still remaining pinhole free.

Mehta[67] advocated the coating of the cathode side rather than the anode side. The reasoning being, that rather than using YSZ to protect ceria from being reduced, it is better used as a barrier to electronic conduction.

If YSZ is on the fuel side of the electrolyte, there is a possibility of it becoming electronically conducting if the P_{O_2} falls low enough, refer Figure 1.13(a). However if the YSZ is on the oxidant side, the P_{O_2} should always fall within the range where YSZ exhibits no electronic conduction, refer Figure 1.13(b).

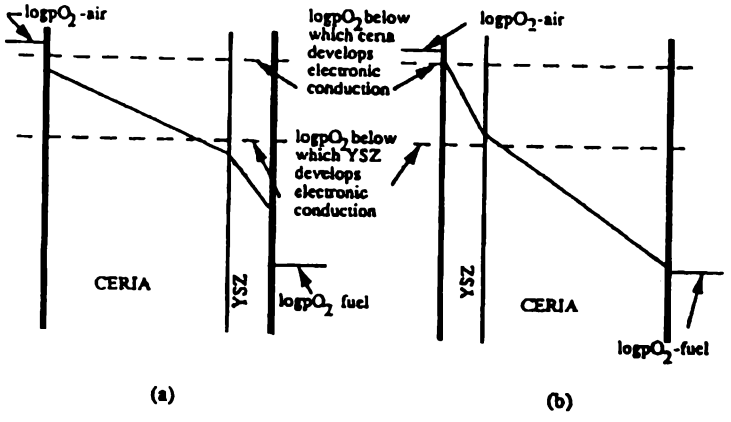

Figure 1.13 Use of YSZ Coatings on Ceria.[67]

YSZ coated ceria electrolyte-based fuel cells have performed well under experimental conditions[67, 86]. For example, YSZ coated samaria (20 cation% Sm) doped ceria showed an open circuit voltage close to the theoretical (unlike the uncoated samaria doped ceria). While the coated sample did exhibit a slightly higher internal resistance, the maximum power density produced was greater than that for the uncoated doped ceria. In fact, the fuel cell using the YSZ coated ceria at 800 °C produced a higher power density than that of YSZ at 1000 °C[86]. However, other researchers[73] have suggested that there is no intrinsic advantage of having a thin layer of YSZ on a ceria electrolyte over having an equally thin YSZ electrolyte. This is likely the case as the ceria is acting more as a support than an electrolyte, though some benefit may be gained through the ability to use a wider range of electrode materials, some of which would react if in direct contact with YSZ[78, 79]. While the coating method is one way of effectively applying ceria electrolytes to SOFC systems, it is not a substantial improvement of the ceria electrolyte[88].

Wachsman[73] investigated the feasibility of a ceria/bismuth oxide bilayered electrolyte. In this case ceria was acting as an anolyte, an anolyte being a material varying from an anode to an electrolyte through its thickness. Providing there was sufficient relative thickness of anolyte, the P_{O_2} at the anolyte/electrolyte interface was high enough to prevent the reduction of bismuth oxide. As it is the relative, rather than absolute, thickness of the components employed that is critical, high performance cells can be produced by reducing the cell thickness.

An alternate method for reducing the electronic conductivity of ceria at low partial pressure is by tailoring the dopant system, particular dopants or dopant combinations having been shown to increase the electrolytic domain boundary, EDB, of ceria[66, 89]. These doping strategies are covered in the following section.

While some workers have concentrated on suppressing the electronic conduction of ceria at low P_{O_2}, others have proposed that if ceria based electrolytes were used at temperatures of ca. 500 °C, then the ionic transference number would be in excess of 0.9[90]. It is now believed that ceria based electrolytes could be employed as SOFC electrolytes in the temperature range of 500-700 °C without substantial loss of efficiency[40, 43, 91].

1.7.3 Doping Ceria

Unlike zirconia, ceria naturally possesses the cubic fluorite-type structure from room temperature to its melting point, refer Figure 1.5, p19. This means that doping is not required to stabilise the oxygen ion conducting cubic fluorite phase. The addition of doping elements to ceria is still beneficial though, as they can increase the ionic conductivity[92]. The increase in conductivity is achieved by the formation of oxygen ion vacancies that act to maintain electroneutrality when lower valence dopant cations are added[93].

A number of dopants have been successfully used with ceria. These include alkaline earth oxides and rare earth oxides. It has been noted that the magnitude of ionic conduction varies with the dopant species[94]. Of the alkaline earth oxides, CaO gives the highest oxygen ion conductivity[36]. When ceria was doped with rare earths, it was found[86] that Sm_2O_3 and Gd_2O_3 gave some of the highest conductivities, with 20 cation% Sm giving the highest conductivity of any of the dopant systems investigated[36]. The explanation for the effect of different dopants on conductivity has been put down to dopant size.

Dopants that have an ionic radius that closely matches that of the host, generally give higher conductivities than those where there is a large mismatch. It is postulated that the size of the dopant cation has an effect on the activation energy by affecting the binding enthalpy between the dopant cation and the anion vacancy.

Interactions Between Dopant Cations and Anion Vacancies.

In doped ceria, the simplest model for oxygen ion conduction is one of thermally activated oxygen ions 'hopping' through the lattice via oxygen ion vacancies, $V_O^{\bullet\bullet}$ [95], known as the 'Random Walk Theory'. This is represented in Equation 1.16.

$$\sigma_i = 2\left[V_O^{\bullet\bullet}\right]|e|\,\mu_i \qquad 1.16$$

$\left[V_O^{\bullet\bullet}\right]$ = the number of vacancies per cm^3

e = the charge on an electron

μ_i = the mobility of $V_O^{\bullet\bullet}$

Note: Equation 1.16 is the oxygen ion vacancy specific form of equation 1.8, p 21, knowing that $\mu = v_d/E$ from equation 1.9, p 21.

According to Equation 1.16, the ionic conductivity, σ_i, should vary linearly with $[V_O^{\bullet\bullet}]$, assuming that the ion mobility, μ_i, is independent of dopant concentration. This relationship is only valid at low vacancy concentration and varies with temperature. At higher vacancy concentrations, the ionic conductivity exhibits a non-linear relationship with dopant concentration[65]. This non-linear relationship is postulated as being due to defect interactions, such as defect pair formation and clustering or vacancy ordering[95]. It is assumed that at low dopant concentrations, anion vacancies are isolated, that is, they are not associated with a dopant ion. As the dopant concentration increases, it becomes more probable that a vacancy will exist in close proximity to a dopant ion. This can lead to the formation of dopant ion-vacancy pairs[95], refer Equation 1.17.

$$M'_{Ce} + V_O^{\bullet\bullet} \rightarrow \left(M'_{Ce}V_O^{\bullet\bullet}\right)^{\bullet} \qquad 1.17$$

As dopant concentrations increase beyond the optimum level ionic conductivity decreases. As the solubility limit is approached, it has been proposed that a measure of vacancy ordering takes place[93]. C-type rare earths, for example Gd_2O_3 and Sm_2O_3, have a crystal structure that is regarded as being a fluorite type structure with ordered oxygen vacancies.

The formation of defect pairs reduces the overall mobility of $V_O^{\bullet\bullet}$. The strength with which the defect pair is bound is termed the binding enthalpy. The binding enthalpy is mainly due to coulombic attractions between the defects caused by their effective charge in the lattice. The binding enthalpy is also affected by the relaxation of the lattice around the defect, the relaxation depending on effective charge, cation polarisability and dopant size[36]. Even a small binding energy will create a marked decrease in conductivity[96]. Kilner[96] has shown that the binding enthalpy depends on the size of the dopant, approaching a minimum when the dopant ion is approximately the same size as the host. The dependence on size is greater for dopant ions that are smaller than the host, rather than larger, as shown in Figure 1.14.

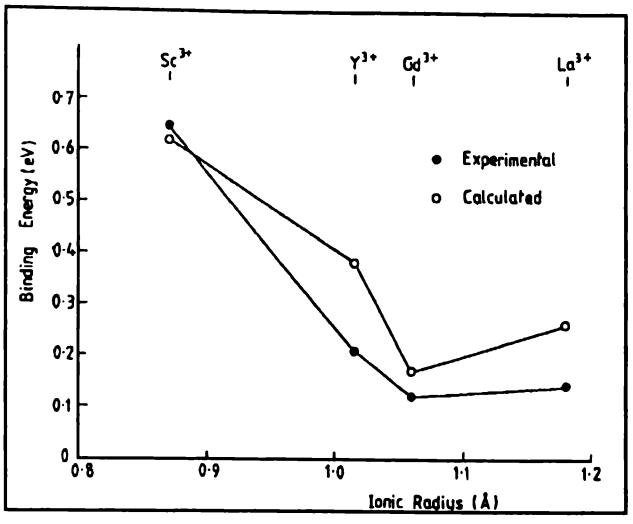

Figure 1.14 Variation of Binding Energy with Dopant Radius[97].

Maximum conductivity is achieved for dopant ions that cause very little expansion or contraction in the fluorite lattice. It should be kept in mind that the introduction of an oxygen vacancy causes a contraction in the lattice[98, 99]. Therefore, when a dopant with a smaller radius than the host is introduced, not only is there a contraction due to the smaller ion, but also that attributed to the oxygen vacancy formed. When a dopant with a larger radius than the host is introduced, there is a tendency for the two effects to neutralise each other. That is, the expansion due to the larger ion is offset by the contraction due to the oxygen vacancy. It has been proposed that this simple matching of dopant ionic radius is insufficient to fully explain the effect of dopant size on conductivity[94]. Kim[94] put forward the concept of the critical radius, r_c, being the ionic radius of the dopant whose substitution for the host cation causes neither expansion nor contraction of the fluorite lattice[36]. Values for r_c have been calculated for divalent and trivalent dopant cations in ceria, these are 0.1106 nm and 0.1038 nm respectively[36].

Table 1.4 Ionic Radii of Common Dopant Species.

Dopant ion	Ionic radius, r_i (nm)[a]	r_c-$r_{i\ (nm)}$
Ce^{4+}	0.097	
Y^{3+}	0.102	-0.0018
Gd^{3+}	0.105	0.0012
Sm^{3+}	0.108	0.0042
Mg^{2+}	0.089	-0.0216
Ca^{2+}	0.112	0.0014
Sr^{4+}	0.126	0.0154

[a] from reference [100]

By comparing the values in Table 1.4, it is apparent why ceria doped with Gd_2O_3 gives a higher conductivity than when doped with Y_2O_3. Although Y^{3+} has an ionic radius that is closer to that of Ce^{4+}, Gd^{3+} has an ionic radius closer to the r_c value for trivalent species in ceria. The table fails to explain why doping with Sm_2O_3 gives a higher conductivity than Gd_2O_3 or Y_2O_3.

Effective index calculations

Mori *et al.*[101, 102] suggested an 'effective index' based on crystallographic considerations. The intent of this effective index is to predict if a material will exhibit significant oxide ion conductivity. From Pauling's first rule, the crystallographic coordination number of a cation is determined by the radius ratio between cation and anion. The fluorite structure is one of the preferred crystal structures for oxide ion conduction. In a non-distorted fluorite lattice, where the cation is coordinated by eight anions the ratio of cation radius to anion radius is 1. Taking into account the work of Kilner *et al.*[96, 103], Mori also incorporated the effect of dopant/host radius mismatch. The effective index expression is given by Equation 1.18.

$$Effective\ Index = (avg.r_c / eff.r_o) \times (r_d / r_h) \qquad 1.18$$

$avg.r_c$ is the average cation radius

$eff.r_o$ is the effective oxygen ion radius, containing the concept that the effective oxygen ion radius decreases with increasing oxygen vacancy level according to Equation 1.19

$$eff.r_o = 1.4 \times \left[\frac{(2-\delta)}{2}\right] \qquad 1.19$$

1.4 is the radius of oxygen in oxides

δ is the level of oxygen vacancies

r_d is the average ionic radius of the dopant ions

r_h is the radius of the host cation

The efficacy of the effective index to predict high ionic conductivity was tested by Mori *et al.*[101]. A number of materials were fabricated having dopant regimes yielding a range of effective index values, it was found that with increasing effective index a higher ionic conductivity was exhibited.

In addition to increasing the ionic conductivity of a material, dopant selection can also influence the EDB of a material[89]. In an effort to extend the EDB of ceria based electrolytes, alternative doping strategies, beyond the standard single dopant, have been investigated.

1.7.4 Co-Doping of Ceria

It seems that Maricle *et al.*[104] first proposed the double doping of ceria to extend its EDB. Maricle *et al.*[66] investigated the effect of the addition of praseodymia to gadolinia doped ceria. It was found that the oxygen partial pressure below which n-type conductivity became significant reached a minimum at 1-3 atom% praseodymium; the oxygen partial pressure being lower by two orders of magnitude with respect to gadolinia doped ceria. It appears that the effect on the EDB was due to the reduction of electronic conductivity, rather than an increase in ionic conductivity. It was postulated that Pr traps the electronic charge carriers through the reduction of Pr^{4+} to Pr^{3+}.

Other researchers have also proposed doping ceria with more than one dopant. Mori and Yamamura[88] theorised that pre-expanding the ceria lattice would cause an increase in the materials' ability to resist reduction. The theory is based on the observation that the ceria lattice can accommodate the larger Ce^{3+} ion, radius 1.14 Å, compared with Ce^{4+}, radius 0.97 Å. Based on this observation it was assumed that the lattice can accommodate dopant systems where the average ionic radius of the dopants was less than or equal to 1.14 Å. Further to this, it was thought that utilising dopants with an average ionic radius approaching this value would expand the lattice and make further expansion due to Ce^{4+}/Ce^{3+} conversion unfavourable. This approach led to the electrolyte material $Ce_{0.75}(Sm_{1-x-y}Cs_xLi_y)_{0.25}O_{2-\delta}$, which not only was less reducible than $Ce_{0.75}Sm_{0.25}O_{2-\delta}$ but also showed a higher conductivity.

Steele[57] has also commented on the use of multiple dopant systems. In this case, the intent was to obtain an exact match between the average dopant radius and the critical radius. By exactly matching the critical radius the association energy of defect clusters would be minimised. It was found that there was a small improvement at temperatures below 350 °C. At 500 °C there was no advantage over the standard material, the presumption being that at this temperature all the defect associates are dissociated in the standard material.

1.7.5 Pr Double Doping of Gd_2O_3 doped CeO_2

After the initial reporting of the praseodymia double doping of ceria, a number of other researchers investigated the material. Navarro *et al.*[105], while agreeing that there was an improvement in the EDB, as reported by Maricle *et al.*[66], could not substantiate an improvement of two orders of magnitude, stating that overall differences between materials were quite small. Further, Navarro considered the thought of Maricle *et al.*[66] that the effect of Pr double doping was due to trapping of the small polarons responsible for electronic conduction. It was concluded that while the addition of Pr to the doped electrolyte does favour the reduction of electronic conduction, the reduction is not significant enough to generate a two-order of magnitude lowering of the EDB. More likely the increase in ionic conductivity noted is also responsible for the lowering of the EDB.

Lubke[40] also investigated the effect of double doping with praseodymia; again a slight increase in overall ionic conductivity was confirmed. On further investigation it was found that the addition of Pr increased the grain boundary conductivity and hence the overall ionic conductivity. The idea that this increase was due to reduction of dopant segregation to grain boundaries was put forward, though not confirmed.

Huang *et al.*[92], investigated the effect of praseodymia double doping in samaria doped ceria, which at equivalent dopant levels is equal to or possibly superior to gadolinia doped ceria[93]. It was found that the addition of Pr increased the overall conductivity of the material, however this was due to increased electronic conductivity, the ionic conductivity of the material remained unchanged. Extension of the EDB was found at low, 2 cation%, double dopant level.

Of interest is the work of Shuk and Greenblatt[106] on praseodymia doped ceria. While the addition of praseodymia increased the ionic conductivity with respect to pure ceria, there was still significant electronic conduction. This was expected as it is known that Pr exhibits mixed valency at atmospheric pressure[107], and hence an equilibrium would exist dependant on the oxygen partial pressure. Therefore, one would expect that a material double doped with praseodymia could exhibit electronic conductivity depending on the oxygen partial pressure.

Steele[57] commented on the results of Huang *et al.*[92], positing the idea that the increase in EDB they obtained was a function of increased grain boundary conductivity. Further, Steele questioned whether the addition of praseodymia to high purity, in his words 'clean', gadolinia doped ceria gave any benefit. One must remember that while lattice conductivity is considered an intrinsic property, the grain boundary conductivity is influenced by the presence of impurities, fabrication method and processing variables. Thus, if praseodymia is in some way influencing the grain boundary conductivity of the materials not all researchers may see the effect, due to differences in impurity levels and fabrication methods.

Maffei *et al.*[82] incorporated an electrolyte of composition $Ce_{0.8}Gd_{0.19}Pr_{0.01}O_{1.905}$ into a fuel cell set-up. They concluded the double doping scheme was not effective in reducing the electronic conduction present in the ceria electrolyte.

It becomes apparent, with sometimes contradictory results, that the effect of praseodymia double doping is not fully understood and further investigation would be beneficial.

1.8 This Thesis

The purpose of this research was to investigate the double doping of $Ce_{0.8}Gd_{0.2}O_{2-\delta}$ with praseodymia and also samaria. Praseodymia double doping was considered due to the controversy and general lack of consensus on its effectiveness. Samaria was considered as it was the other co-dopant proposed by the paper first reporting double doping[66]. While the initial paper reported the results of one samaria containing sample, there appears to have been little further work looking at the use of samaria as a double dopant in $Ce_{0.8}Gd_{0.2}O_{2-\delta}$. Further, some effects of the fabrication method are also investigated.

The remainder of this thesis is arranged as follows:

Chapter 2 - Methodology

The Methodology chapter provides the theoretical background for the fabrication, characterisation and analysis methods employed in this study. Included are variables known to affect the co-precipitation method and a discussion on aspects affecting consolidation and sintering.

Chapter 3 - Experimental Method

The Experimental Method chapter details the actual experimental procedures and parameters employed during the course of this research.

Chapter 4 - Results and Discussion

The Results and Discussion chapter presents the results obtained from this research. The results for the different samples are compared with and contrasted against one another and also results from literature.

Chapter 5 - Conclusions and Recommendations

Based on the results and discussions in the previous chapter conclusions regarding the properties and use of the materials investigated are drawn. From these conclusions recommendations for further work are made.

Bibliography

[1] Anderson, H. U., Chen, C.C., Wang, J.C., Pennell, M.J., Synthesis of Conducting Oxide Films and Powders from Polymeric Precusors., in *Third International Conference on Powder Processing Science,* p.749-755, (1990). San Diego, USA.

[2] Appleby, A. J., Fuel Cell Electrolytes: Evolution, Properties and Future Prospects., *Journal of Power Sources,* **49**:p.15-34, (1994).

[3] Sammes, N. M., Energy Conversion Using Solid Oxide Fuel Cells., *Current,* **3**(3): p.17-19, (1993).

[4] Appleby, A. J., The Electrochemical Engine for Vehicles., *Scientific American,* **July**:p.74-79, (1999).

[5] Hirshenhofer, J. H., Stauffer, D.B., Engleman, R.R., Klett, M.G., Fuel Cell Handbook, Fourth Edition., U.S. Department of Energy, (1998)

[6] Milliken, C., Guruswamy, S., Khundkar, A., Evaluation of Ceria Electrolytes in Solid Oxide Fuel Cells Electric Power Generation., *Journal of the Electrochemical Society.,* **146**(3): p.872-882, (1999).

[7] Singhal, S. C., Advances in Solid Oxide Fuel Cell Technology., *Solid State Ionics,* **135**:p.305-313, (2000).

[8] Steele, B. C. H., Materials for IT-SOFC Stacks; 35 Years R&D: The Inevitability of Gradualness?, *Solid State Ionics,* **134**:p.3-20, (2000).

[9] Grove, W. R., On Voltaic Series and the Combination of Gases by Platinum., *Philosophical Magazine,* **14**:p.127-130, (1839).

[10] World Fuel Cell Council, *Will Fuel Cells Power our Future?*, 15 October 1999, Presentation to EquipAuto '99, Paris

[11] Lloyd, A. C., The Power Plant in Your Basement., *Scientific American,* **July**:p.80-86, (1999).

[12] Sammes, N. M., Fuel Cell Possibilities., *New Zealand Science Monthly,* **3**(9): p.12, (1992).

[13] Campbell, C. J., *The Coming Oil Crisis.*, Petroconsultants, (1997).

[14] Thomas, S., Zalbowitz, M., Fuel Cells - Green Power., Los Alamos National Laboratory, (1999)

[15] Appleby, A. J., Fuel Cell Technology: Status and Future Prospects., *Energy,* **21**(7/8): p.521-653, (1996).

[16] Boersma, R. J., Sammes, N.M., Fuel Cell Handbook, Centre for Technology, University of Waikato, (1998)

[17] Ackermann, T., Distributed Power Generation in a Deregulated Market., *Energy-Wise News,* **September**:p.33, (1999).

[18] Barlow, R., Residential Fuel Cells: Hope or Hype?, *Home Power,* **72**:p.20-29, (1999).

[19] Baur, E., Preis, H., *Z. Elektrochem.*, **43**:p.727-732, (1937).

[20] Nernst, W., *Z. Elecktrochem.*, **6**:p.41-43, (1899).

[21] Minh, N. Q., Ceramic Fuel Cells., *Journal of the American Ceramic Society*, **76**(3): p.563-588, (1993).

[22] Song, R.-H., Kim, E.-Y., Shin, D.R., Yokokawa, H., Fabrication and Characteristics of Anode-Supported Tube for Solid Oxide Fuel Cell., in *Sixth International Symposium on Solid Oxide Fuel Cell (SOFC VI)*, p.845-848, (1999). Honolulu, Hawaii.

[23] Singhal, S. C., Progress in Tubular Solid Oxide Fuel Cell Technology., in *Sixth International Symposium on Solid Oxide Fuel Cells. (SOFC VI)*, p.39-51, (1999). Honolulu, Hawaii.

[24] Diethelm, R., Schmidt, M., Status fo the Sulzer Hexis Product Development., in *Solid Oxide Fuel Cells (SOFC VI)*, p.60-67, (1999). Honolulu, Hawaii.

[25] Yamamoto, O., Applications., p.292-332, in *Solid State Electrochemistry*, Bruce, P. G. (ed.), Cambridge University Press, (1995).

[26] Goodenough, J. B., Ceramic Solid Electrolytes., *Solid State Ionics*, **94**:p.17-25, (1997).

[27] Van Herle, J., Horita, T., Kawada, T., Sakai, N., Yokokawa, H., Dokiya, M., Sintering Behaviour and Ionic Conductivity of Yttria-Doped Ceria., *Journal of the European Ceramic Society*, **16**:p.961-973, (1996).

[28] Steele, B. C. H., Oxygen Transport and Exchange in Oxide Ceramics., *Journal of Power Sources*, **49**:p.1-14, (1994).

[29] Yoshimura, M., Phase Stability of Zirconia., *Ceramic Bulletin*, **67**(12): p.1950-1955, (1988).

[30] Badwal, S. P. S., Zirconia -based Solid Electrolytes: Microstructure, Stability and Ionic Conductivity., *Solid State Ionics*, **52**:p.23-32, (1992).

[31] Sorensen, O. T., Johannesen, O., Clausen, K., Oxygen Ion Conduction in Solid Oxide Electrolytes with the Fluorite Structure., in *6th Riso International Symposium on Metallurgy and Materials Science*, p.93-117, (1985). Roskilde.

[32] Rickert, H., *Electrochemistry of Solids, An Introduction.*, (1982).

[33] West, A. R., Crystalline Solid Electrolytes I: General Considerations and the Major Materials., p.7-42, in *Solid State Electrochemistry*, Bruce, P. G. (ed.), Cambridge University Press, (1995).

[34] Goodenough, J. B., Crystalline Solid Electrolytes II: Material Design., p.43-73, in *Solid State Electrochemistry*, Bruce, P. G. (ed.), Cambridge University Press, (1995).

[35] Gao, W., Sammes, N.M., *An Introduction to Electronic and Ionic Materials.*, World Scientific, (1999).

[36] Inaba, H., Tagawa, H.,, Ceria-based Solid Electrolytes., *Solid State Ionics*, **83**:p.1-16, (1996).

[37] Kroger, F. A., *Journal of the American Ceramic Society*, **49**:p.415, (1966).

[38] Chebotin, V. N., Mezrin, V.A., Ordering of Defects, Thermodynamic and Transport Properties of Solid Oxide Electrolytes with Fluorite Structure., *Physica Status Solidi (a),* **89**:p.199-211, (1985).

[39] Duran, P., Moure, C., Jurado, J. R., Sintering and Microstructural Development of Ceria-Gadolinia Dispersed Powders., *Journal of Materials Science,* **29**:p.1940-1948, (1994).

[40] Lubke, S., Wiemhofer, H. D., Electronic Conductivity of Gd-Doped Ceria with Additional Pr-Doping., *Solid State Ionics,* **117**(3-4): p.229-243, (1999).

[41] Badwal, S. P. S., Grain Boundary Resistivity in Zirconia Based Materials: Effect of Sintering Temperatures and Impurities., *Solid State Ionics,* **76**:p.67-80, (1995).

[42] Badwal, S. P. S., Ciacchi, F.T., Drennan, J., Investigation of the Stability of Ceria-Gadolinia Electrolytes in Solid Oxide Fuel Cell Environments., *Solid State Ionics,* **121**:p.253-262, (1999).

[43] Christie, G. G., van Berkel, F.P.F., Microstructure - Ionic Conductivity Relationships in Ceria-Gadolinia Electrolytes., *Solid State Ionics,* **83**:p.17-27, (1996).

[44] El Adham, K., Hammou, A., "Grain Boundary Effect" on Ceria Based Solid Solutions., *Solid State Ionics,* **9-10**:p.905-912, (1983).

[45] Gerhardt, R., Nowick, A.S., Grain-Boundary Effect in Ceria Doped with Trivalent Cations: II, Microstructure and Microanalysis., *Journal of the American Ceramic Society,* **69**(9): p.647-651, (1986).

[46] Gerhardt, R., Nowick, A.S., Grain Boundary Effect in Ceria Doped with Trivalent Cations: I, Electrical Measurements., *Journal of the American Ceramics Society,* **69**(9): p.641-646, (1986).

[47] Guo, X., Yuan, R.-Z., Grain Boundary Ionic Conduction of Zirconia-based Solid Electrolyte: Idea and Practice., *Journal of Materials Science Letters,* **14**:p.499-502, (1995).

[48] Hong, S. J., Mehta, K., Virkar, A.V., Effect of Microstructure and Composition on Ionic Conductivity of Rare-Earth Oxide-Doped Ceria., *Journal of the Electrochemical Society,* **145**(2): p.638-647, (1998).

[49] Lang, H.-J., Kunstler, K., Tomandl, G., Oxygen Exchange Behaviour and Electrical Conductivity of Polycrystalline Oxide-ion Conductors Based on $Ce_{1-n}La_nO_{2-0.5n}$., *Solid State Ionics,* **119**:p.127-130, (1999).

[50] Mogensen, M., Lindegaard, T., Hansen, U.R., Mogensen, G., Optimalizing Mixed Conductor SOFC Anodes of Doped CeO_2., in *Symposium on Ionics and Mixed Conducting Ceramics,* (1994). San Francisco.

[51] Tian, C., Chan, S.-W., Ionic Conductivities, Sintering Temperatures and Microstructures of Bulk Ceramic CeO_2 Doped with Y_2O_3., *Solid State Ionics,* **134**:p.89-102, (2000).

[52] Badwal, S. P. S., Rajendran, S., Effect of Micro- and Nano-Structures on the Properties of Ionic Conductors., *Solid State Ionics,* **70/71**:p.83-95, (1994).

[53] Hughes, A. E., Badwal, S.P.S., Impurity and Yttrium Segregation in Yttria-tetragonal Zirconia., *Solid State Ionics,* **46**:p.265-274, (1991).

[54] Theunissen, G. S. A. M., Winnubst, A.J.A., Burggraaf, A.J., Surface and Grain Boundary Analysis of Doped Zirconia Ceramics Studied by AES and XPS., *Journal of Materials Science,* **27**:p.5057-5066, (1992).

[55] Wang, D. Y., Nowick, A.S., The "Grain Boundary Effect" in Doped Ceria Solid Electrolytes., *Journal of Solid State Chemistry,* **35**:p.325-333, (1980).

[56] Bauerle, J. E., Study of Solid Electrolyte Polarization by a Complex Admittance Method., *Journal of Physics and Chemistry of Solids,* **30**:p.2657-2669, (1969).

[57] Steele, B. C. H., Appraisal of $Ce_{1-y}Gd_yO2_{-y/2}$ Electrolytes for IT-SOFC Operation at 500 °C., *Solid State Ionics,* **129**:p.95-110, (2000).

[58] Lee, W. E., Rainforth, W.M., *Ceramic Microstructures, Property Control by Processing.*, Chapman and Hall, (1994).

[59] Whalen, P. J., Reidinger, F., Correale, S.T., Marti, J., *Journal of Materials Science,* **22**:p.4465, (1987).

[60] Frenkel, J., *Kinetic Theory of Liquids.*, Claredon Press, (1946).

[61] Duffy, D. M., Tasker, P.W., *Philosophical Magazine,* **A54**(6): p.1266, (1986).

[62] Service, R. F., New Tigers in the Fuel Cell Tank., *Science,* **288**(5473): p.1955-1957, (2000).

[63] Godickemeier, M., Gauckler, L.J., Engineering of Solid Oxide Fuel Cells with Ceria-Based Electrolytes., *Journal of the Electrochemical Society,* **145**(2): p.414-421, (1998).

[64] Godickemeier, M., Sasaki, K., Gauckler, L.J., Operation Principles for Fuel Cells with Mixed Ionic Electronic Conductors., p.717-725,

[65] Dirstine, R. T., Blumenthal, R. N., Kuech, T. F., Ionic Conductivity of Calcia , Yttria and Rare earth-Doped Cerium Dioxide., *Journal of the Electrochemical Society: Solid-State Science and Technology,* **126**(2): p.262-269, (1979).

[66] Maricle, D. L., Swarr, T.E., Karavolis, S., Enhanced Ceria - a Low-Temperature SOFC Electrolyte., *Solid State Ionics,* **52**:p.173-182, (1992).

[67] Mehta, K., Hong, S.J., Jue, J-F., Virkar, A.V., Fabrication and Characterization of YSZ-coated Ceria Electrolyte., in *Third International Symposium of Solid Oxide Fuel Cells,* (1993).

[68] Van Herle, J., Horita, T., Kawada, T., Sakai, N., Yokokawa, H., Dokiya, M., Low Temperature Fabrication of (Y, Gd, Sm)-doped Ceria Electrolyte., *Solid State Ionics,* **86-88**:p.1255-1258, (1996).

[69] Zheng, K., Steele, B.C.H., Sahibzada, M., Metcalfe, I.S.,, Solid Oxide Fuel Cells Based on $Ce(Gd)O_{2-x}$ Electrolytes., *Solid State Ionics,* **86-88**:p.1241-1244, (1996).

[70] Watanabe, W., Uchida, H., Yoshida, M., Effect of Ionic Conductivity of Zirconia Electrolytes on the Polarization Behaviour of Ceria-Based Anodes in Solid Oxide Fuel Cells., *Journal of the Electrochemical Society,* **144**(5): p.1739-1743, (1997).

[71] Chen, C. C., Nasrallah, M.M., Anderson, H.U., Synthesis and Characterization of $(CeO_2)_{0.8}(SmO_{1.5})_{0.2}$ Thin Films from Polymeric Precursors., *Journal of the Electrochemical Society,* **140**(12): p.3555-3560, (1993).

[72] Lewis, G. S., Atkinson, A., Steele, B.C.H., Sintering of Gadolinia-Doped Ceria at Reduced Temperature., in *Fourth European SOFC Forum,* p.773-782, (2000). Lucerne, Switzerland.

[73] Wachsman, E. D., Jayaweera, P., Jiang, N., Lowe, D.M., Pound B.G., Stable High Conductivity Ceria/Bismuth Oxide Bilayered Electrolytes., *Journal of the Electrochemical Society,* **144**(1): p.233-236, (1997).

[74] Kharton, V. V., Yaremchenko, A.A., Naumovich, E.N., Marques, M.B., Research on the Electrochemistry of Oxygen Ion Conductors in the Former Soviet Union. III HfO_2-, CeO_2- and ThO_2-based Oxides., *Journal of Solid State Electrochemistry,* **4**:p.243-266, (2000).

[75] Worrell, W. L., Solid Oxide Electrolytes., in *Solid Electrolytes*, Gellar, S. (ed.), Springer-Verlag, (1977).

[76] Subbarao, E. C., Maiti, H.S., Solid Electrolytes with Oxygen Ion Conduction., *Solid State Ionics,* **11**:p.317-338, (1984).

[77] Steele, B. C. H., Oxygen Ion Conductors., in *High Conductivity Solid Ionic Conductors*, Takahashi, T. (ed.), World Scientific, (1988).

[78] Kindermann, L., Das, D., Nickel, H., Hilpert, K., Chemical Compatibility of the $LaFeO_3$ base Perovskites $(La_{0.6}Sr_{0.4})_zFe_{0.8}M_{0.2}O_{3-d}$ (z=1, 0.9; M=Cr, Mn, Co, Ni) with Yttria Stabilized Zirconia., *Solid State Ionics,* **89**:p.215-220, (1996).

[79] Kawada, T., Sakai, N., Yokokawa, H., Dokiya, M., Anzai, I., Reaction Between Solid Oxide Fuel Cell Materials., *Solid State Ionics,* **50**:p.189-196, (1992).

[80] Eguchi, K., Inoue, T., Setoguchi, T., Arai, H., Activities of Rare-earth-containing Oxides as Electrodes for Oxide Ion Conductor., *Journal of Alloys and Compounds,* **193**:p.59-61, (1993).

[81] Inoue, T., Setoguchi, T., Eguchi, K., Arai, H., Study of a Solid Oxide Fuel Cell with a Ceria-Based Solid Electrolyte., *Solid State Ionics,* **35**:p.285-291, (1989).

[82] Maffei, N., Kuriakose, A.K., Solid Oxide Fuel Cells of Ceria Doped with Gadolinium and Praseodymium., *Solid State Ionics,* **107**:p.67-71, (1998).

[83] Bernal, S., Blanco, G., Cifredo, G., Perez-Omil, J.A., Pintado, J.M., Rodriguez-Izquierdo, J.M., Reducibility of Ceria-Lanthana Mixed Oxides Under Temperature Programmed Hydrogen and Inert Gas Flow Conditions., *Journal of Alloys and Compounds,* **250**:p.449-454, (1997).

[84] Griffiths, T. R., Hubbard, H.V.St.A., Davies, M.J., Electron Transfer Reactions in Non-Stoichiometric Ceria and Urania., *Inorganica Chimica Acta,* **225**:p.305-317, (1994).

[85] Steele, B. C. H., Floyd, J.M., *Proceedings of the British Ceramic Society,* **19**:p.55, (1971).

[86] Eguchi, K., Setoguchi, T., Inoue, T., Arai, H., Electrical Properties of Ceria-Based Oxides and their Application to Solid Oxide Fuel Cells., *Solid State Ionics,* **52**:p.155-172, (1992).

[87] Mogensen, M., Lindegaard, T., Hansen, U.R., Physical Properties of Mixed Conductor Solid Oxide Fuel Cell Anodes of Doped CeO_2., *Journal of the Electrochemical Society,* **141**(8): p.2122-2128, (1994).

[88] Mori, T., Yamamura, H., Preparation of an Alkali-Element-Doped CeO_2-Sm_2O_3 System and its Operation Properties as the Electrolyte in Planar Solid Oxide Fuel Cells., *Journal of the American Ceramic Society,* **79**(12): p.3309-3312, (1996).

[89] Yahiro, H., Eguchi, K., Arai, H., Electrical Properties and Reducibilities of Ceria-Rare Earth Oxide Systems and their Application to Solid Oxide Fuel Cell., *Solid State Ionics,* **36**:p.71-75, (1989).

[90] Steele, B. C. H., State-of-the-Art SOFC Ceramic Materials., in *1st European SOFC Forum.,* p.375-398, (1994). Lucerne.

[91] Scanlon, P. J., Bink, R.A.M., Van Berkel, F.P.F., Christie, G.M., Van Ijzendoorn, L.J., Brongersma, H.H., Van Welzenis, R.G., Surface Composition of Ceramic CeGd-Oxide., *Solid State Ionics,* **112**:p.123-130, (1998).

[92] Huang, W., Shuk, P., Greenblatt, M., Hydrothermal Synthesis and Properties of Terbium- or Praseodymium-doped $Ce_{1-x}Sm_xO_{2-x/2}$ Solid Solutions., *Solid State Ionics,* **113-115**:p.305-310, (1998).

[93] Yahiro, H., Eguchi, Y., Eguchi, K., Arai, H., Oxygen Ion Conductivity of the Ceria-Samarium Oxide System with Fluorite Structure., *Journal of Applied Electrochemistry,* **18**:p.527-531, (1988).

[94] Kim, D.-J., Lattice Parameters, Ionic Conductivities and Solubility Limits in Fluorite-Structure MO_2 Oxide (M=Hf^{4+}, Zr^{4+}, Ce^{4+}, Th^{4+}, U^{4+}) Solid Solutions., *Journal of the American Ceramic Society,* **72**(8): p.1415-1421, (1987).

[95] Hohnke, D. K., Ionic Conduction in Doped Oxides with the Fluorite Structure., *Solid State Ionics,* **5**:p.531-534, (1981).

[96] Kilner, J. A., Fast Anion Transport in Solids., *Solid State Ionics,* **8**:p.201-207, (1983).

[97] Butler, V., Catlow, C.R.A., Fender, B.E.F., Harding, J.H., Dopant Ion Radius and Ionic Conductivity in Cerium Dioxide., *Solid State Ionics,* **8**:p.109-113, (1983).

[98] Li, P., Chen, I-W., Penner-Hahn, J.E., Tien, T-Y., X-ray Absorption Studies of Ceria with Trivalent Dopants., *Journal of the American Ceramic Society,* **74**(5): p.958-967, (1991).

[99] Hasegawa, M., Kato, Y., Kagawa, M., Syono, Y., Effect of Additive Oxides on Ultrafine CeO_2 Particles Synthesized by the Spray-ICP Technique., *Journal of Materials Science Letters,* **15**:p.1608-1611, (1996).

[100] Shannon, R. D., Revised Effective Ionic Radii and Systematic Studies of Interatomic Distances in Halides and Chalcongenides., *Acta Crystallographica, Section A,* **A32**(5): p.751-767, (1976).

[101] Mori, T., Ikegami, T., Yamamura, H., Application of a Crystallographic Index for Improvement of the Electrolytic Properties of the CeO_2-Sm_2O_3 System., *Journal of the Electrochemical Society.,* **146**(12): p.4380-4385, (1999).

[102] Mori, T., Lee J.-H., Li, J., Ikegami, T., Auchterlonie, G., Drennan, J., Improvement of the Electrolytic Properties of Y_2O_3-based Materials Using a Crystallographic Index., *Solid State Ionics,* **138**:p.277-291, (2001).

[103] Kilner, J. A., Brook, R.J., A Study of Oxygen Ion Conductivity in Doped Non-stoichiometric Oxides., *Solid State Ionics,* **6**:p.237-252, (1982).

[104] Maricle, D. L., Swarr, T.E., Tuller, H.L., Ceria Electrolyte Composition., Patent# 5,001,021, United States of America, (1991)

[105] Navarro, L., Marques, F., Frade, J., n-Type Conductivity in Gadolinia-Doped Ceria., *Journal of the Electrochemical Society,* **144**(1): p.267-273, (1997).

[106] Shuk, P., Greenblatt, M., Hydrothermal Synthesis and Properties of Mixed Conductors Based on $Ce_{1-x}Pr_xO_{2-d}$Solid Solutions., *Solid State Ionics,* **116**:p.217-223, (1999).

[107] Inaba, H., Naito, K., *Solid State Chemistry,* **50**:p.100, (1983).

Chapter Two

2 Methodology

2.1 Overview

This chapter provides a discussion of the experimental procedures employed during the course of this research. Powder fabrication aspects are considered with discussion devoted to the two powder production methods used. The steps for preparing a solid body sample, namely consolidation and sintering, are discussed. Finally the theoretical aspects of the sample characterisation techniques used are presented.

2.2 Powder Fabrication

A number of researchers[1-7] have commented on the importance of powder fabrication; the properties of the powder can significantly affect the final item. The effects are varied and can be profound. The introduction of impurities from raw materials and during processing can enhance the phenomenon known as the grain boundary effect (as mentioned in Chapter One). The particle size of the powder and the presence of agglomerates affect the ability of the powder to densify during the sintering process. A large particle size powder will lead to a large grain size sintered item, large grain sizes cause the material to be mechanically weaker[8]. Poor dopant distribution in the starting powder can adversely affect the performance of the sintered item, possibly causing the presence of second phases and properties other than those expected.

When fabricating doped-ceramic powders one of the main concerns is that the material produced is the targeted composition.

In the case of ceria based ceramics, for fuel cell electrolyte use, this requires that the dopant and ceria should form a solid solution in the appropriate structural phase, cubic fluorite. The cubic fluorite phase is the phase associated with high oxide ion conduction.

Traditionally such ceramics have been produced by solid state methods. This involves the intimate mixing of the different oxide materials followed by prolonged heating at high temperature, typically 10 hours at 1300 °C[9]. The prolonged heating at elevated temperatures associated with the solid state method has a number of drawbacks: the powders produced often have large grain sizes due to the elevated firing temperatures[10]; the powders often have poor chemical homogeneity[10], particularly when dopant oxides are used at low levels; the calcination regime often converts the soft agglomerates present in the starting powder to hard agglomerates[4, 11, 12], which are much more difficult to eliminate from the powder.

The preparation of ceramic oxide materials by wet chemical methods offers a number of advantages, such as high purity, chemical homogeneity, small and uniform particle size[13]. Also, as there is no need to force a solid state reaction to occur, the materials produced by wet chemical methods can be calcined at lower temperatures, leading to a smaller oxide powder particle size with less hard agglomerates present. It has also been found that the oxide powders produced through the wet chemical methods are more sinterable than the powders produced though the traditional solid state method. Two such wet chemical methods of preparing oxide ceramics are co-precipitation and the Pechini method.

2.2.1 Co-precipitation

The purpose of co-precipitation is to prepare a multi-component oxide ceramic through the formation of an intermediate oxalate, which is subsequently calcined to produce the oxide powder. The process involves the mixing of a solution of metal salts with a precipitant solution. For this work oxalic acid was used as the precipitant.

The oxalates produced have advantages over the intermediates produced using other precipitants: they are reported to be insensitive to washing and drying conditions, unlike hydroxide precipitates[14, 15] and production of oxalates gives close to 100% yield, unlike carbonate precipitates[16].

There are two general ways in which co-precipitation can be performed, termed 'forward strike' and 'reverse strike'. The forward strike method involves the addition of the precipitant solution to the metal ion containing solution. There is a concern though, that the difference in solubilities of the potential precipitates can lead to the preferential precipitation of one metal ion over the other. The reverse strike method overcomes this problem by slowly adding the metal ion solution to the precipitant. By adding a small amount of the metal solution to an excess of precipitant all of the metal ions are simultaneously precipitated from solution. The ideal situation is shown in Equation 2.1, where a mixed metal oxalate precipitate is formed, rather than oxalates of the individual metals ions.

$$2\left(0.8Ce(NO_3)_3 + 0.2Gd(NO_3)_3\right) + 3(C_2O_4H_2) \rightarrow (Ce_{0.8}Gd_{0.2})_2(C_2O_4)_3 + 6HNO_3 \qquad 2.1$$

Van herle *et al.*[17] has investigated the effect varying the co-precipitation process parameters has on oxalate formation and the final oxide powder properties. The parameters investigated were oxalic acid concentration, metal ion solution concentration and pH. Their findings are summarised below.

Oxalic Acid Concentration

- When oxalic acid concentration was increased the average size of the particles present in the oxide powder also increased.
- Sintered pellets prepared from powders produced at high oxalic acid concentrations had a relative density lower than those pellets prepared using powder produced employing lower oxalic acid concentrations.
- As oxalic acid concentration was increased separate metal oxalates were formed rather than the preferred mixed metal oxalate.

Metal Ion Concentration

- When the metal ion solution concentration was increased the average particle size decreased.
- Sintered pellets prepared from powders prepared at high metal ion solution concentrations yielded higher density pellets than their low metal ion concentration counterparts.

pH Effect

- When pH was unadjusted (initial pH 2, falling to 1.7) the oxide powder produced had a slightly higher average particle size and produced lower density sintered pellets.
- Above pH 3 the effect of pH was negligible on particle size and sintered density.
- Low pH caused the formation of separate metal oxalates, rather than a single mixed metal oxalate.

The recommendations from the work of Van herle *et al.* are that the following parameters be employed: oxalic acid concentration of 0.06 M or less, metal ion solution concentration of 1 M and maintain the pH of the reaction mixture at 6.9.

Metal nitrates are the preferred source of metal ions, rather than metal chlorides, as it is known[18] that nitrates are less problematic with respect to removal of the salt anion during precipitate washing. Washing with distilled water to remove the salt anion was followed by washing with alcohol as it has been shown in other systems[14, 19] that washing with water can produce hard agglomerates, while washing with alcohol tends to produce soft agglomerates. Hard agglomerates are undesirable as they do not break-up during pressing, producing an inhomogeneity in the green compact that affects the later sintering process.

2.2.2 Modified Pechini Method

Although the method used by Chen *et al.*[20] has been termed a sol-gel technique by some[21, 22], it is more correctly a variation of the Pechini method[10]. The sol-gel term refers to the formation of gels from colloidal oxides or hydrated oxide dispersions; or the hydrolytic reactions of metal-organic compounds such as metal alkoxides[10]. In the Pechini method chelates are formed between citric acid and metal ions. The chelate then undergoes polyesterification when heated with ethylene glycol. The resulting polymer yields an oxide powder on further heating.

Pennell[23] altered the basic Pechini method by omitting citric acid and adding nitric acid. This change is more than swapping one acid for another, as the two act in different ways, citric acid acts as a chelating agent where nitric acid acts to oxidise the ethylene glycol present in the mixture. Although the exact reaction scheme is not known it is believed that the nitric acid oxidises a portion of the ethylene glycol to form oxalic acid, this acts as a chelating agent for the metal ions, on heating the acid undergoes a condensation reaction with the remaining ethylene glycol to form a polyester, refer Figure 2.1.

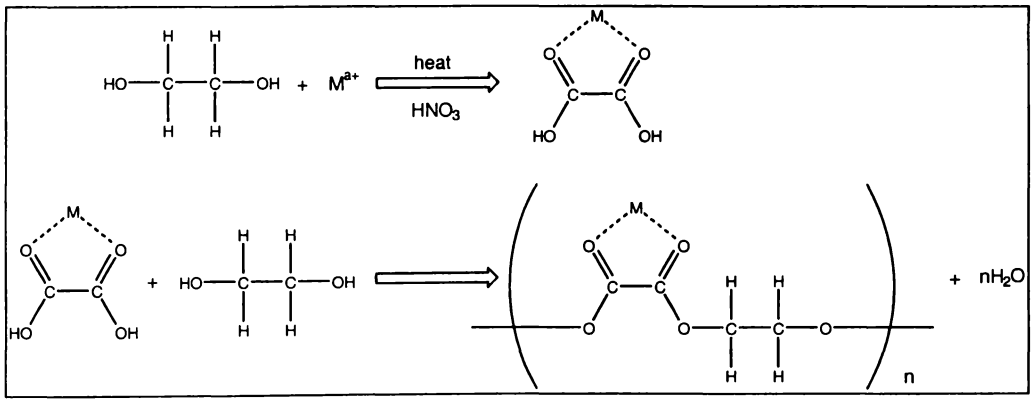

Figure 2.1 Possible Reaction Mechanism for Ethylene Glycol Reaction.

2.2.3 Calcination

Calcination is the process whereby a solid material is heated to drive off volatile chemically-combined substances, oxidise materials or cause particle growth[24]. In this work the purpose of calcination is to decompose the prepared intermediate products, to the desired oxide material. The reactions involved in the calcination of oxalates are not well understood, the major reactions thought to occur[25] are given in Equations 2.2-2.4.

$$(CeGd)_2(C_2O_4)_3.xH_2O \rightarrow (CeGd)_2(C_2O_4)_3 + xH_2O \quad 2.2$$

$$(CeGd)_2(C_2O_4)_3 \rightarrow (CeGd)O_{2-\delta} + CO + CO_2 \quad 2.3a$$

$$(CeGd)_2(C_2O_4)_3 \rightarrow (CeGd)_2(CO_3)_3 + CO \quad 2.3b$$

$$(CeGd)_2(CO_3)_3 \rightarrow (CeGd)O_{2-\delta} + CO_2 \quad 2.4$$

The calcination reactions of the gel derived from the modified Pechini method are expected to be complex, involving the oxidation of the polyester backbone with the production of H_2O, CO_2, the metal oxide and possibly CO and C. There may possibly be nitrogen oxides produced due to the presence of NO_3^-.

2.3 Sample Preparation

Once an oxide powder has been fabricated it needs to be formed into a shape suitable for further use. For example, the fabrication of a fuel cell would typically require the fabrication of a gas impermeable electrolyte, on which suitable anode and cathode materials can be coated, this would most likely be as an extruded tube or a flat plate. For experimental examination the powder is usually fabricated into a pellet or billet appropriate for the desired testing. The process of creating this solid shape occurs in two steps, initial consolidation of the powder to form a green compact, followed by firing the compact to form a sintered body. The term green density is used when referring to the density of the un-sintered green compact.

2.3.1 Consolidation

The purpose of consolidation is to form the fabricated powder into a solid shape suitable for further processing and analysis. Generally consolidation is achieved by the application of pressure. Consolidation takes place through two processes. Initially particles slide past one another to fill pores of a size similar to the particles themselves; at higher pressures the pores with a size smaller than the original particles are filled by plastic deformation and particle fragmentation[26].

The main factor when considering consolidation is the production of a homogenous compact, a secondary factor is the production of a compact with adequate green density[27]. Inhomogeneities in the powder compact can cause mechanical weaknesses in the final product and also affect the sintering of the object. Sintering generally amplifies rather than diminishes compaction defects[28] and if there are density variations in the compact then differential shrinkage may occur leading to cracking of the sample on sintering[29]. The green density of the compact is important as a high green density can improve the sintered density of the material[30]. However having a uniform distribution of void space without agglomerates is more important than achieving a high green density by employing a powder with a range of particle sizes[2].

Effect of the Starting Powder Properties

Yan[28] has stated that the ideal powder should have the attributes of small particle size, non-agglomerated, equiaxed particle shapes, small size distribution and controlled dopant content. Not all of these attributes impact on the consolidation of the powder.

A small particle size generally has a more profound effect on sintering rather than consolidation, though there are some effects that relate to compact formation. For small particles, <10 μm, the interparticle cohesion exceeds the influence of weight[29]. This means that particles stick to one another and initial particle packing is low.

As force is applied the cohesion between particles is overcome and the packing of the particles improves. Also as a consequence of their high cohesion/weight ratio, powders with a small particle size are not free flowing, this can affect their ability to fill a mould[29]. Some powders are agglomerated through spray drying to improve their flowability[27].

If agglomerates present in the starting powder are too hard, the pressures employed during compaction will be insufficient to destroy them. This means that the agglomerates will still be present in the green compact. The presence of agglomerates is detrimental to the sintered density of the sample.

The shape of the particles present in the powder affects the efficiency of their packing. The poor alignment of needle-like particles, that is particles with a high aspect ratio, during compaction leads to their failing to attain an adequate sintered density[28]. The aspect ratio of a particle is the ratio of its length to breadth. Equiaxed particles, having an aspect ratio less than two[4], are able to attain good alignment during compaction and subsequently lead to a higher sintered density. In addition Cahn *et al.*[31] have shown that powders containing angular particles exhibit torque and shear forces between the constituent particles which contributes to particle rearrangement, an essential part of the initial sintering process[28].

While powders containing a range of particle sizes can pack more effectively, producing denser compacts, it is generally preferable to have a narrow size distribution, either monomodal or bimodal[32]. If large particle size range powders are employed powder-packing inhomogeneities are more likely. In addition to the effect of inhomogeneities, compacts produced from large particle size range powders fail to achieve a high sintered density due to pores separating from the grain boundaries[28]. Once pores have separated from the grain boundary they are very difficult to eliminate from the material.

Uniaxial Pressing

In uniaxial pressing, force is applied to a punch in a mould with rigid sides, commonly referred to as a die. Density variations almost always occur, these variations are due to inhomogenous filling of the die and the pressing process itself[27]. These density variations increase with increasing height of the compact. When force is applied from above the upper corners of the profile show a higher density than the main body; the lower corners of the profile show a lower density, refer Figure 2.2.

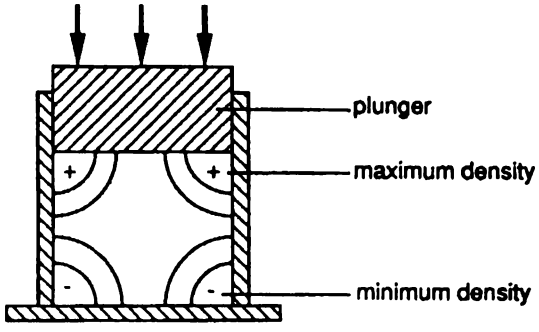

Figure 2.2 Density Variations with Uniaxial Pressing[33].

Irregularities on the surface of the punch will also cause density variations, with projections causing a higher density directly below them and indentations producing a lower density area. Density variations will also be caused by friction against the walls of the die[29], which can be lowered by using an appropriate lubricant.

Cold Isostatic Pressing

In cold isostatic pressing, CIP, pressure is applied by a liquid surrounding an object sealed in an impermeable covering; the term cold is used to distinguish the process from hot isostatic pressing, HIP, where the sample is heated simultaneously with the pressure application. There are two modes in which CIP can be performed: dry-bag tooling and wet-bag tooling (Figure 2.3). In wet-bag tooling a preformed shape is placed in a disposable envelop and isostatically pressed. Dry-bag tooling involves the use of a pre-shaped reusable mould into which the powder is placed and then isostatically pressed.

Density variations can occur in isostatically pressed samples due to friction between the sample and the rubber mould.

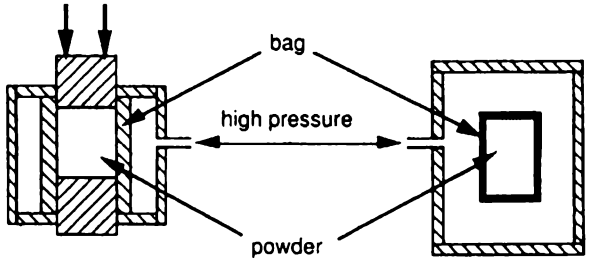

Figure 2.3 Dry-bag (left) and Wet-bag (right) Tooling[33].

2.3.2 Sintering

The purpose of sintering is to densify a powder compact. The driving force for the densification is the reduction of the Gibbs free energy by replacing particle surfaces with lower energy grain boundaries[34]. The greater the surface area of the powder, that is the smaller the particle size, the greater the thermodynamic potential for densification[35]; densification being a shrinkage process, requiring the centres of particles to approach each other[36].

There are three stages of sintering[4, 34, 35]: initial maximisation of contact points between grains; growth of the necks between grains and elimination of closed pores.

Initial Stage

During this first stage grains are reordered though rotational and translational movement to maximise the contact points between grains. When the sintering temperature is high enough to facilitate diffusion, mass transport will occur with material being transported to the contact region between grains, forming a 'neck'.

Intermediate Stage

The grains present in the material are now in contact with their nearest neighbours. Shrinkage can only occur by transfer of material from the grain boundaries to the neck area. Material will be removed from the grain boundaries, by lattice or grain boundary diffusion, and transported to the neck region, reducing the surface energy and causing shrinkage. This process is called densification. There are also competing mass transport mechanisms such as evaporation-condensation and surface diffusion. These mechanisms move material from the particle surface to the neck area, reducing the surface energy but not affecting the distance between particle centres; this process of reducing surface energy without shrinkage is known as coarsening and leads to grain growth. The pores present in the material form a network of continuous channels. The intermediate stage ends when the channels become narrow and undergo Rayleigh break-up to form closed pores[36].

Final Stage

The closed pores present in the material are mainly sited at the junction of three grains. In the final stage of sintering these isolated pores are removed by mass transport from the grain boundary to the pore surface. Lange[35] showed that there is a critical number of particles required to be in contact with a pore to allow its complete removal. If no coarsening of the material occurs a pore will be eliminated if the number of particles contacting it is less than or equal to a critical number. If a greater number of particles are contacting the pore than the critical number it will shrink to an equilibrium size but will not be eliminated. The critical number, n_c, is given by Equation 2.5, where φ_e is the dihedral angle. The dihedral angle is the angle formed where the grain boundary intersects the particle's surface, refer Figure 2.4.

$$n_c = \frac{2\pi}{(\pi - \varphi_e)} \qquad 2.5$$

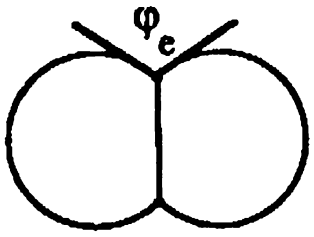

Figure 2.4 Illustration of φ_e, the Dihedral Angle[35].

During sintering coarsening may occur through interparticle mass transport; large particles will grow at the expense of smaller particles[35]. Coarsening being the reduction of surface energy without shrinkage, leading to particle growth[35]. Coarsening can therefore reduce the number of particles coordinating a pore and possibly, by reducing the number of particles below the critical number, lead to the pore being eliminated. Thus while coarsening is generally to be avoided, due to the disadvantages of larger grain sizes, it can increase the sintered density of the material[19].

While discussions on sintering so far have focused on individual particle contacts, neck growth and elimination of closed pores, there are other factors that influence the sintering of real powders, the main one being the presence of agglomerates.

Effect of Agglomerates on Sintering

Agglomerates are small masses of primary particles bound together[26]. Agglomerates can be classified as either hard or soft; hard agglomerates are strongly bonded, possibly sintered together and are sometimes called aggregates; soft agglomerates are bound together by surface forces such as van der Waals attractions. The surface force per unit weight is inversely proportional to particle size[28], hence agglomeration is more pronounced in submicron powders. Soft agglomerates are inherent in dry, fine-particle-size powders and can be transformed to hard agglomerates during heat treatments[19].

Soft agglomerates are preferable over hard agglomerates; while often causing a lower green density, powders containing soft agglomerates sinter to a higher density than those containing hard agglomerates[19]. Agglomerates cause problems during sintering primarily by preferential sintering[2], The preferential sintering is due to the particles making up the agglomerate being more tightly packed than the particles making up the remainder of the powder[28]. The shrinkage associated with sintering means that the agglomerate contracts away from the neighbouring particles, enhancing the voids already present around the agglomerate. The enlargement of these voids makes it more difficult to obtain a fully dense sample for a given sintering regime.

2.4 Sample Characterisation

The powders produced by the two methods and the sintered pellets were characterised using a number of techniques. These included x-ray diffraction, electron and x-ray microscopy, surface area and particle size measurements, Raman spectroscopy and impedance spectroscopy.

2.4.1 Powder X-ray Diffraction

Powder x-ray diffraction is a useful technique for determining the crystalline forms, known as phases, of a material and also the phase purity of the sample. The data obtained from powder x-ray diffraction can also be used to calculate the lattice parameters of the crystalline form present and the crystallite size of powders where the crystallite size is small enough to cause peak broadening.

X-rays interact primarily with the electrons in matter; when x-rays strike an inorganic material x-rays are scattered in all directions by the electrons present in the material. Where the scattering centres are separated by a distance comparable to the wavelength of the x-rays interference between the diffracted x-rays can occur. Where there is ordering of the scattering centres, such as in a crystal lattice, the interference of the scattered x-rays will give rise to a set of intensity maxima and minima.

Maxima will occur when the Bragg condition is satisfied, that is, the extra distance travelled by x-rays striking a family of crystal planes is equal to 2dsinθ, refer Figure 2.5 and Equation 2.6.

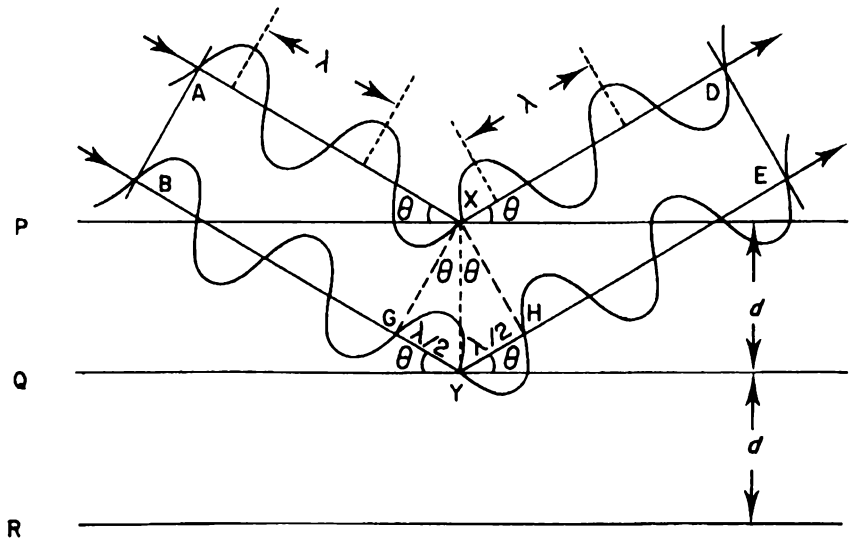

Figure 2.5 The Bragg Condition[37].

P, Q and R are the edges of a family of lattice planes, distance *d* apart.

X-rays, wavelength λ, strike the planes with an incident angle θ.

The lower of the beams, B-Y-E, travels a greater distance than beam A-X-D by an amount equal to 2(*d*sinθ).

Constructive interference will occur when 2(*d*sinθ) is equal to the wavelength, λ, or an integer multiple of it, refer equation 2.6, the Bragg Equation.

$$n\lambda = 2d\sin\theta \qquad 2.6$$

When this condition is met constructive interference occurs, if the condition is not met destructive interference occurs and no peak is produced.

The positions of the maxima are related to the lattice parameters, the Miller indices and the x-ray wavelength. Refer to Appendix 2 for an explanation of basic crystallography, including Miller indices.

A powder sample contains a large number of small crystallites, which randomly adopt all possible orientations. When struck by an x-ray beam the crystallites will diffract the beam in all possible directions simultaneously, as determined by the Bragg equation (equation 2.6). This data can be collected using a Debye-Scherrer camera or a diffractometer. The data collected from the XRD pattern can be used to ascertain the phase purity of the sample by comparison to the literature or indexing of the pattern (outside the scope of this research). The data can also be used to calculate the lattice parameters of the material.

Lattice Parameter Determination

It is possible to calculate the lattice parameters of a material providing that Miller indices can be assigned to the various reflections present in the powder diffraction pattern. For a cubic structure such as fluorite the following expression is used, (Equation 2.7).

$$a^2 = \frac{\lambda^2}{4\sin^2\theta}\left(h^2 + k^2 + l^2\right) \qquad 2.7$$

Equation 2.7 is obtained by combining the Bragg equation (Equation 2.6) with the expression for d of a cubic system expressed in terms of Miller indices, hkl, and the lattice parameter, a, Equation 2.8. For cubic systems there is only one lattice parameter as all lattice sides are of equal length, with all angles 90°.

$$\frac{1}{d^2} = \frac{h^2 + k^2 + l^2}{a^2} \qquad 2.8$$

While Equation 2.7 can be used to determine the actual lattice parameter of a sample, the theoretical lattice parameter for the material can also be calculated. The theoretical lattice parameter, a, of an ideal cubic fluorite structure is given by Equation 2.9, where r_{cation} and r_{anion} are the ionic radii of the cation and anion respectively.

$$a = \frac{4}{\sqrt{3}}(r_{cation} + r_{anion}) \qquad 2.9$$

When dopant elements are added to the material the average radius of the cation has to used and, if applicable, the effect of vacancies accounted for. Incorporating these aspects into equation 2.9 yields equation 2.10, which is specific to the doping of $MO_{1.5}$ into CeO_2.

$$a = \frac{4}{\sqrt{3}} xr_m + (1-x)r_{Ce} + (1-0.25x)r_O + 0.25xr_{V_o} \qquad 2.10$$

Where x is the dopant concentration and r_M, r_{Ce} and r_O are the ionic radii of the dopant metal ion, Ce^{4+} and O^{2-} respectively. The effective ionic radius of an oxygen vacancy, r_{VO}, was determined by Hong and Virkar[38] to be 1.164 Å, and represents a contraction compared to the ionic radius of the oxide ion, 1.42 Å[39].

Crystallite Size Determination

The size of crystallites present in a powder can be determined by peak broadening in the x-ray diffraction pattern. The term crystallite size should not be confused with particle size; crystallite implies a small single crystal, a particle may be an agglomerate of crystallites[40].

To obtain a sharp peak in powder x-ray diffraction crystallites need to be sufficient size to cause destructive interference away from the 2θ maximum. This is by virtue of their having a large number of crystallographic planes, each successively slightly out of phase, the summation of these numerous planes eventually produces destructive interference[41].

Where there is a small crystallite size, there are insufficient planes to cause total destructive interference away from the 2θ maximum; this leads to broadening of the peak. It should be noted that even materials with very large crystallites will still produce peaks with a measurable breadth due to broadening caused by the instrumentation and other factors such as temperature[42].

Crystallite size, t, can be determined from the Scherrer formula, Equation 2.11.

$$t = \frac{K\lambda}{\sqrt{B_M^2 - B_S^2}\cos\theta} \qquad 2.11$$

K is a shape factor, for cubic materials a value of 0.9 is used
λ is the wavelength of the x - rays
B_m is the observed halfwidth of the sample
B_s is the halfwidth of the standard material (crystallite size greater than 1μm)
θ is the diffraction angle

The term 'halfwidth' (or more correctly full width half maxima, FWHM) refers to the width of the peak at a position of half the peak's maximum intensity, refer Figure 2.6.

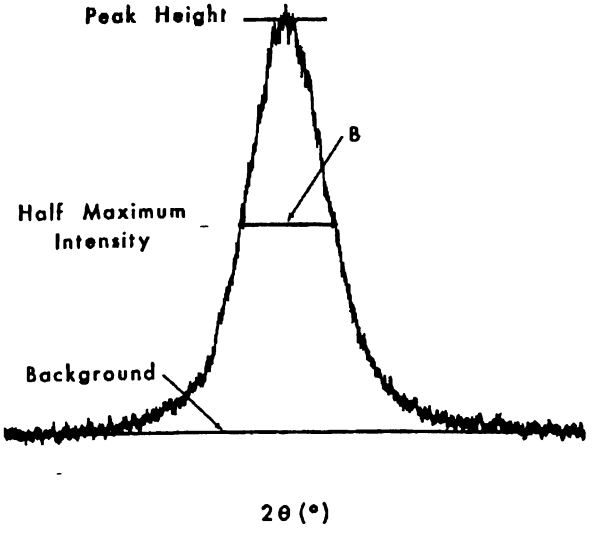

Figure 2.6 Halfwidth Determination[42].

The standard material needs to have a crystallite size in excess of 1 μm, so that the sole cause of broadening for its peak is due to instrumental and other intrinsic factors.

2.4.2 High Temperature X-ray Diffraction

Combining a furnace with x-ray diffraction instrumentation allows the collection of diffraction patterns over a wide range of temperatures. This can enable the identification of phase changes with temperature. The data can also be used to calculate lattice parameters at different temperatures and hence the thermal expansion of the material. The average thermal expansion, $\bar{\alpha}$, of a material over the temperature range T_0 to T is determined using Equation 2.12, where a_T is the lattice parameter at temperature T and a_{T_0} is the lattice parameter at T_0[43].

$$\bar{\alpha} = \frac{a_T - a_{T_0}}{a_{T_0}(T - T_0)} \qquad 2.12$$

2.4.3 X-ray Microscopy

X-ray microscopy gives an image showing density variations within a sample. This is achieved by passing an x-ray beam from a small focus through the sample, the conical beam is then detected by an x-ray-sensitive camera, creating an enlarged radiograph of the sample. The magnification is simply the ratio of the distances from the x-ray source to the detector and from source to sample. When an x-ray passes through a medium, the intensity of the transmitted beam, I, is attenuated logarithmically. If the incident beam, intensity I_0, has travelled a distance x cm, the linear absorption coefficient, μ_l can be expressed as follows (Equation 2.13).

$$\mu_l = \frac{1}{x} \ln \frac{I}{I_0} \qquad 2.13$$

From equation 2.13 it can be seen that the units of μ_l are reciprocal centimetres and represents the attenuation of the beam per unit length travelled. The linear absorption coefficient depends on the wavelength of the x-rays, the atomic numbers of the constituent atoms and their state of aggregation[44]. The calculation of the linear absorption coefficient is complicated by particle aggregation, making it more convenient to use a mass absorption coefficient, μ_m. The relationship between mass and linear absorption coefficients is shown in Equation 2.14, where ρ is the density of the material.

$$\mu_m = \frac{\mu_l}{\rho} \qquad 2.14$$

By combining Equations 2.13 and 2.14 an expression for the effect of density, ρ, on transmitted beam intensity, I, can be obtained, refer Equation 2.15.

$$I = I_0 \exp(-\mu_m x \rho) \qquad 2.15$$

As a consequence of Equation 2.15 denser areas of material appear as darker regions on the radiograph, while less dense areas appear as lighter areas.

2.4.4 Surface Area Determination

The surface area of a powder sample can be determined by measuring the amount of a known material required to form a single layer of molecules on the surface of the powder. If the area per molecule adsorbed is known then the surface area can be calculated. The most commonly used method is the adsorption of an inert gas at the boiling point of the corresponding liquid. The most frequently used gas is nitrogen, due to its inertness and the ready availability of liquid nitrogen. The model usually used to relate gas adsorption to surface area is the BET model from the work of Brunauer, Emmett and Teller[45].

There are a number of assumptions underpinning the simplest BET isotherm, these are presented in the following list:

- ❖ Gas adsorbs on the flat, uniform surface of the solid with a uniform heat of adsorption due to van der Waals forces between the gas and the solid.
- ❖ There is no lateral interaction between the adsorbed molecules.
- ❖ After the surface has become partially covered by adsorbed gas molecules additional gas can adsorb either on the remaining free surface or on top of the already adsorbed layer.
- ❖ The adsorption of the second and subsequent layers occurs with a heat of adsorption equal to the heat of liquefaction of the nitrogen.
- ❖ There is no limit to the number of layers which can adsorb.

The BET isotherm equation based on the simplest BET model is given in Equation 2.16.

$$\frac{V}{V_m} = \frac{c\left(P/P_0\right)}{\left(1-P/P_0\right)\left(1+(c-1)P/P_0\right)} \qquad 2.16$$

where:

V=volume of gas adsorbed at pressure P

V_m=the volume of gas which would cover the entire surface assuming monolayer coverage

P_0=the saturation pressure

c is a constant for the gas solid combination, given by Equation 2.17.

$$c = \exp((q_1 - q_L)/RT) \qquad 2.17$$

q_1=the heat of adsorption for the first layer

q_L=the heat of liquefaction

R=the universal gas constant

T=temperature

Before samples can have their surface area measured they need to be outgassed, where the gases already adsorbed to the surface are removed; this is accomplished by heating the sample under vacuum. This outgassing procedure can cause problems when the material in question undergoes some sort of change, such as loss of structural water, during the procedure.

2.4.5 Particle Size Analysis

Particle size analysis was performed using a forward laser light scattering instrument, as shown in Figure 2.7.

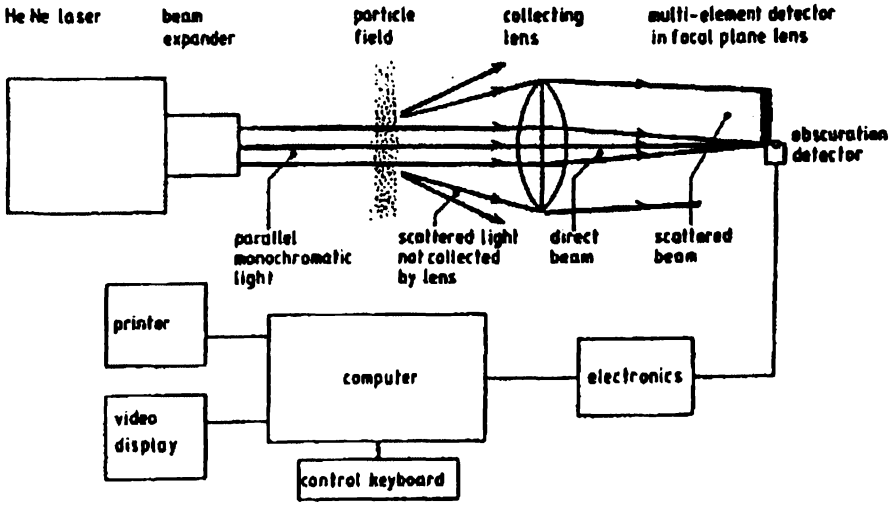

Figure 2.7 Schematic of a Forward Laser Light Instrument[6].

The scattering of light by small particles can be used to calculate the size distribution of the particles. A general law of light scattering was published by Mie in 1908. For a spherical particle the intensity, I, of the scattered light is given by Equation 2.18.

$$\frac{I}{I_0} = \frac{\lambda^2}{8\pi R^2}(i_{\parallel} + i_{\perp}) \qquad 2.18$$

Where:

λ = wavelength of the light

I_0 = the intensity of the incident light

R = the distance from the scatterer to the detector

$i_{\parallel}$ and $i_{\perp}$ are the components polarised parallel and perpendicular to the incident plane. These are a complex function of the angle of incidence, θ; the complex refractive index, m, of the particle relative to the medium; the particle diameter, x, and the wavelength of the light, λ.

While not all particles are spherical, a size value can be determined using equivalent sphere theory; where a one dimensional property is measured and related to a sphere to derive a single size parameter.

2.4.6 Raman Spectroscopy

Raman spectroscopy makes use of the Raman effect, where light is inelastically scattered from a material. When a material is struck by a beam of light of a single wavelength, the majority of it is scattered at the same wavelength as the incident beam, termed Rayleigh scattering; however a portion of the incident light is scattered with a wavelength different from the incident beam, Raman scattering. The change in wavelength is due to changes in molecular motion. The difference in energies between the incident light and the scattered light is termed the Raman shift. Several different Raman shifted signals will be detected, each due to different vibrational or rotational states of the molecules in the sample, the molecular symmetry and the environment will determine the Raman signals observed.

Raman scattering exhibits two forms, caused by molecular or crystal lattice vibrational transitions, Stokes scattering and anti-Stokes. Stokes scattering results in a light of a lower energy than the incident beam being scattered, while anti-Stokes scattering produces light of higher energy than the incident beam being produced[46], refer to Figure 2.8.

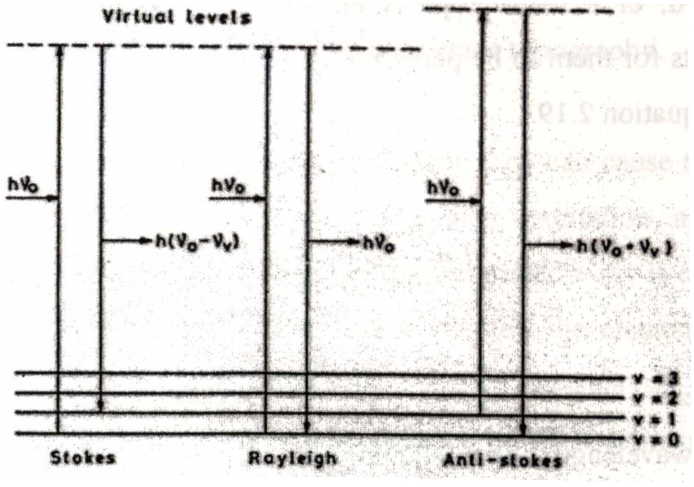

Figure 2.8 Energy Transitions Associated with Raman Spectroscopy[47].

Typically Stokes transitions are studied in Raman spectroscopy due to their greater intensity[47].

First order scattering occurs where a single vibrational transition occurs, second order scattering occurs when two vibrational transitions occur.

The number and type of vibrations observed by Raman spectroscopy can be determined using factor group analysis. In this method the space group and number of formula units in the unit cell are used to calculate the irreducible representations of the vibrational modes. Factor group analysis for CeO_2 predicts a single first order vibrational mode[48]. The doped cerias used in this work have the same cubic symmetry as CeO_2 and hence the same Raman spectrum.

2.4.7 Scanning Electron Microscopy and Energy Dispersive X-ray Analysis

Scanning electron microscopy, SEM, is routinely used in the investigation of the microstructure of materials. The main reason for its use is that the resolving power of an electron microscope is far superior to that of a light microscope. Resolving power, d, of a microscope is the minimum distance that must be between two objects for them to be perceived as separate objects and is given by Abbe's formula, Equation 2.19.

$$d = \frac{0.612\lambda}{n \sin \alpha} \qquad 2.19$$

Where:

λ = wavelength of the radiation

n = index of refraction of the medium through which the radiation travels

α = aperture angle

For an electron the wavelength, λ, is given by Equation 2.20.

$$\lambda = \sqrt{\frac{h^2}{2Vem}} \qquad 2.20$$

Where:

V = accelerating voltage

E = charge of an electron

m = mass of an electron

h = Planks constant

For a light microscope using green light, λ = 5000 Å and the best possible numerical aperture of 1.4, the resolving power (d) is 2500 Å. For an electron microscope using an accelerating voltage of 10, 000 V, λ = 0.37 Å and d = 0.2 Å.

SEM imaging in this work was performed using the emissive mode, whereby secondary electrons are detected. Secondary electrons are produced by either primary electrons knocking out loosely held electrons in the sample which then escape the surface of the material; or primary electrons being deflected a number of times by elastic and inelastic scattering events, losing most of their energy. In either case the secondary electrons are of low energy (typically 20 eV[4]). As they are of low energy, secondary electrons only escape from the outermost regions of the sample and hence provide information on surface topography.

When high energy electrons impinge on a sample they can cause the emission of x-rays from the constituent atoms due to their excitation and subsequent relaxation. The energy, and wavelength, of the generated x-ray is characteristic of the element generating it and can be used to identify the elements present in a sample. This is the basis of Energy Dispersive X-ray analysis, EDX. Lower atomic number elements are unable to be detected by EDX as insufficient energy is able to be supplied to them to cause electron excitation.

2.4.8 Impedance Spectroscopy

This technique involves the application of an alternating voltage across a material while the frequency of the signal is varied. The magnitude and phase change of the resulting current output is compared to the voltage input allowing calculation of the impedance of the system.

The applied electric signal, U, is given by Equation 2.21, where U_0 is the signal amplitude, i is the imaginary number equal to $\sqrt{-1}$, ω is the angular frequency and t is the time constant.

$$U = U_0 \exp(i\omega t) \qquad 2.21$$

The current output of the system, I, is also sinusoidal with the same angular frequency, ω, but differences in amplitude, I_0, and phase angle, ϕ, (Equation 2.22) may occur depending on the sample being analysed.

$$I = I_0 \exp i(t\omega + \phi) \qquad 2.22$$

The impedance of the cell, Z, is thus determined by Equation 2.23, where Z_0 is the modulus of the impedance of the sample

$$Z = \frac{U}{I} = \frac{U_0 \exp(-i\phi)}{I_0} = Z_0 \exp(-i\phi) \qquad 2.23$$

Equation 2.23 can be expressed using Euler's theorem, as shown in Equation 2.24.

$$\begin{aligned} Z &= Z_0 \cos\phi - iZ_0 \sin\phi \\ &= Z_R - iZ_I \end{aligned} \qquad 2.24$$

where:

Z_R is the real impedance

Z_I is the imaginary impedance

As each electrolyte process has a different time constant they relax over different frequency ranges. Providing the applied frequency range is large enough then the contribution of the individual processes can be separated. When the data from a typical solid electrolyte is plotted on a Nyquist plot, also called a complex plane plot, a graph similar to Figure 2.9 is produced.

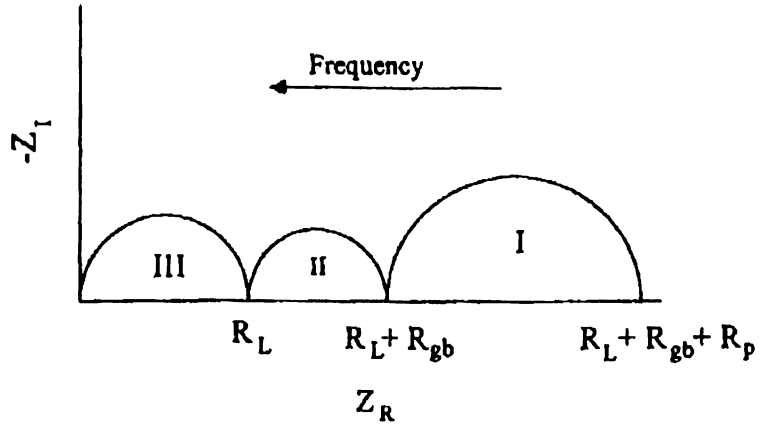

Figure 2.9 Typical Impedance Diagram[49].

In Figure 2.9 arc I is attributed to electrode processes, arc II to grain boundary processes and arc III to electrolyte lattice (intragrain) processes[50]. The intercepts on the x-axis correlate to the resistances of the components, where R_L is the resistance of the lattice processes, R_{gb} is the resistance of the grain boundaries and R_p is the resistance of the electrode processes. The peak of each arc corresponds with the capacitance associated with the different processes.

The response from a solid electrolyte can be considered the same as a response from a circuit containing resistance, R, and capacitance, C, components, therefore for a well-resolved impedance diagram an equivalent circuit can be constructed. The equivalent circuit for the impedance diagram shown in Figure 2.9 is shown below in Figure 2.10.

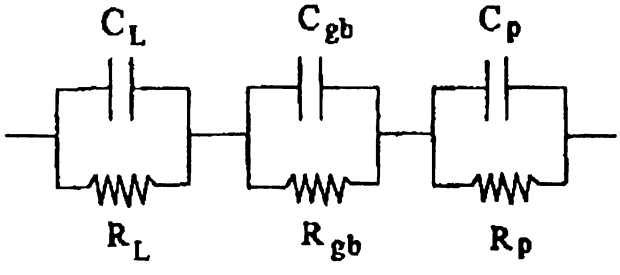

Figure 2.10 Equivalent Circuit Representing a Solid Electrolyte Cell[49].

The ability to separate grain boundary from lattice impedances is useful in solid electrolytes as the lattice impedance is considered to be an intrinsic property related to the composition of the material, while the grain boundary impedance is thought to be a process related variable, strongly influenced by impurity content and fabrication method.

By housing the sample under investigation in a vessel supplied with a gas mixture of known oxygen partial pressure, impedance spectroscopy can be used to determine the effect oxygen partial pressure has on the resistivity, and hence conductivity, of the sample.

Oxygen Partial Pressure Generation

Samples were tested at a range of oxygen partial pressures below atmospheric, as it is at low oxygen partial pressures that ceria is known to exhibit electronic conductivity. Electronic conductivity in the electrolyte material is detrimental to the operation of a fuel cell. Oxygen partial pressures were generated by passing a N_2/H_2 mixture through a distilled water bubbler held at a set temperature.

The low oxygen partial pressures were generated from the reaction shown in Equation 2.25.

$$H_2O \leftrightarrow H_2 + \tfrac{1}{2}O_2 \qquad 2.25$$

Equation 2.25 has the equilibrium constant shown in Equation 2.26.

$$K = \frac{P_{H_2}\left(P_{O_2}\right)^{\frac{1}{2}}}{P_{H_2O}} \qquad 2.26$$

At any given temperature water in the bubbler will generate a vapour pressure, P_{H_2O}; knowing the P_{H_2} of the gas mixture supplied to the bubbler and the equilibrium constant at the temperature of testing (obtainable from data sources such as Thermodynamic and Transport Properties of Fluids[51]) one can calculate the P_{O_2} of the post-bubbler gas stream.

2.4.9 Differential Thermal Analysis

Differential thermal analysis, DTA, is a method where the difference in temperature between a sample and a reference are recorded when both sample and reference are subjected to identical heating regimes. A series of peaks will be produced, provided the sample is thermally active in the temperature range employed. The position of the peaks will depend on the chemical composition and crystal structure of the material. Thermal events such as endothermic or exothermic reactions will cause a peak, either negative or positive, to be produced at a characteristic temperature, dependent on the particular operating conditions.

2.4.10 Ion Beam Analysis

Ion beam analysis, IBA, is based on the interactions that occur between accelerated charged particles and the atoms that make up the material under investigation. The technique involves the bombardment of the sample with a beam of high energy light element ions, generally provided by an ion accelerator. When an accelerated charged particle impinges on the sample it interacts with the electrons and nuclei of the material's atoms, slows down and possibly deviates from the original trajectory. This can lead to the emission of particles and radiation with energies characteristic of the elements present in the sample. Particles may: penetrate the nucleus, causing a nuclear reaction to occur (Nuclear Reaction Analysis); scatter in a backward direction (Rutherford Backscattering Spectrometry) or excite the electron shell, causing the emission of x-rays (Particle Induced X-ray Emission). There are also other interactions (and associated analytical techniques) that may occur though the three mentioned are those employed in the course of this research.

A typical IBA setup is shown in Figure 2.11.

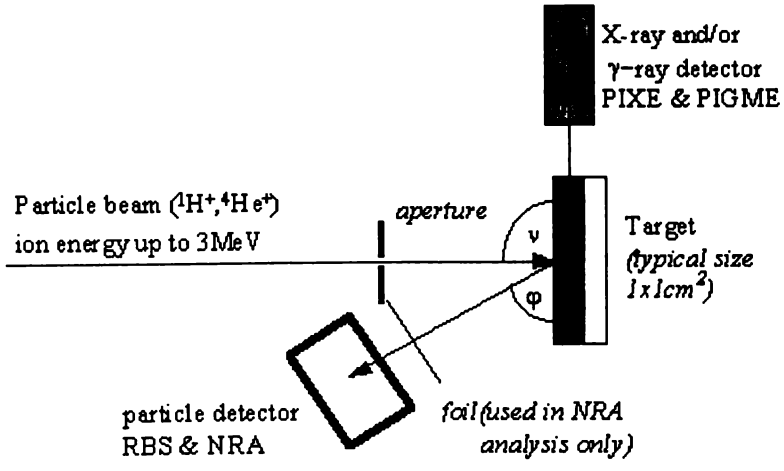

ν = *incident ion angle (tilting increases the depth resolution)*
φ = *backscattering angle (normally about 160°-170°)*

Figure 2.11 Setup for IBA[52].

(PIGME = Particle Induced Gamma-ray Emission)

Nuclear Reaction Analysis, NRA

This technique is used to detect O, N and C with a low detection limit[53], though only O was investigated for this research. The technique is based on the detection of secondary charged particles produced from a nuclear reaction between an atom and the incident charged particle. The nuclear reaction for oxygen detection was $^{16}O(d,p_1)^{17}O$, where a ^{16}O hit by a deuteron, d, produces ^{17}O and a proton, p_1.

Particle Induced X-ray Emission, PIXE

PIXE is an ideal technique for the detection of impurities, minor and major elements in solid-state materials, being able to detect elements from magnesium onward in the periodic table, with a low detection limit (typically 1-10 ppm)[54]. The accelerated particle beam causes ionisation to occur near the atomic nucleus[55]. Subsequent electronic rearrangements cause the emission of x-rays having energies characteristic of the element emitting them.

Rutherford Backscattering Spectrometry, RBS

RBS detects the presence and energy of particles from the incident ion beam elastically scattered back from the sample. The majority of the incident particles are implanted in the sample, only a small fraction undergo direct collision with the nucleus of an atom present in the upper strata of the sample[56]. The collision does not involve direct physical contact between the accelerated particle and the target atom, rather energy exchange occurs through Coulombic forces between the nuclei when in close proximity. The accelerated particle loses energy through two processes, travelling through the material both pre- and post-collision and from the collision itself. Energy loss from travelling through the material is dependent on the materials stopping power. The loss of energy from the collision is dependent on the masses of the projectile ion and the target atom, the ratio of the projectile energy after collision to the projectile energy prior collision is called the kinematic factor, K, as given in Equation .

$$K = \frac{E_{scattered}}{E_{incident}} = \left[\frac{\left(1 - \left(\frac{M_1 \sin\theta}{M_2}\right)^2\right)^{\frac{1}{2}} + \frac{M_1 \cos\theta}{M_2}}{1 + \frac{M_1}{M_2}} \right]^2 \qquad 2.27$$

E = ion energy

M_1 = mass of incident ion

M_2 = mass of target atom

θ = scattering angle

Energy loss from scattering at the surface of the sample will be due to the kinematic factor alone. In addition to surface investigations, RBS is also useful in depth profiling. This requires the material density of the sample and stopping power values to be taken into consideration[54].

Bibliography

[1] Balazs, G. G., Glass, R.S., AC Impedance Studies of Rare Earth Oxide Doped Ceria., *Solid State Ionics,* **76**:p.155-162, (1995).

[2] Bowen, H. K., Processing Ceramics: Presintering Science., in *First China-Us Bilateral Seminar on Inorganic Materials Research,* p.48-58, (1983). Shanghai.

[3] Duran, P., Moure, C., Jurado, J. R., Sintering and Microstructural Development of Ceria-Gadolinia Dispersed Powders., *Journal of Materials Science,* **29**:p.1940-1948, (1994).

[4] Lee, W. E., Rainforth, W.M., *Ceramic Microstructures, Property Control by Processing.*, Chapman and Hall, (1994).

[5] Roosen, A., Seitz, K., Powder Surface Chemistry in Ceramic Powder Processing., *DKG,* **74**(5): p.230-234, (1997).

[6] Scarlett, B., Characterization of Particles and Powders., p.99-125, in *Processing of Ceramics - Part I,* Brook, R. J. (ed.), VCH, (1995).

[7] Schubert, H., Petzow, G., Preparation and Characterization of Ceramic Powders., p.45-56, in *Advanced Ceramics III,* Somiya, S. (ed.), Elsevier Science Publishers Ltd., (1990).

[8] Van Herle, J., Horita, T., Kawada, T., Sakai, N., Yokokawa, H., Dokiya, M., Sintering Behaviour and Ionic Conductivity of Yttria-Doped Ceria., *Journal of the European Ceramic Society,* **16**:p.961-973, (1996).

[9] Eguchi, K., Setoguchi, T., Inoue, T., Arai, H., Electrical Properties of Ceria-Based Oxides and their Application to Solid Oxide Fuel Cells., *Solid State Ionics,* **52**:p.155-172, (1992).

[10] Segal, D., Chemical Preparation of Powders., p.69-98, in *Processing of Ceramics - Part I,* Brook, R. J. (ed.), VCH, (1995).

[11] Dynys, F. W., Halloran, J.W., Influence of Aggregates on Sintering., *Journal of the American Ceramic Society,* **67**(9): p.596-601, (1984).

[12] Lange, F. F., Influence of Agglomerates on Sintered Ceramics., in *First China_US Bilateral Seminar on Inorganic Materials Research,* p.59-75, (1983). Shanghai.

[13] Johnson, D. W. J., Innovations in Ceramic Powder Preparation., p.3-19, in *Advances in Ceramics, Vol 21: Ceramic Powder Science*, Messing, G. L., Mazidiyasni, K.S., McCauley, J.W., Haber, R.A. (ed.), The American Ceramic Society Inc., (1987).

[14] Haberko, K., Characteristic Sintering Behaviour of Zirconia Ultrafine Powder., *Ceramics International,* **5**:p.148-154, (1979).

[15] Jordan, G. W., Berard, M.F., Production of Highly Sinterable Rare Earth Oxide Powders by Controlled Humidity Dewatering of Products., *Ceramics International,* **9**:p.87-92, (1983).

[16] Dragoo, A. L., Domingues, L.P., Preparation of High-Density Ceria-Yttria Ceramics., *Journal of the American Ceramic Society,* **65**:p.253-259, (1982).

[17] Van Herle, J., Horita, T., Kawada, T., Sakai, N., Yokokawa, H., Dokiya, M., Fabrication and Sintering of Fine Yttria Doped Ceria Powder., *Journal of the American Ceramic Society,* **80**(4): p.933-940, (1997).

[18] Roosen, A., Hausner, H., Techniques for Agglomeration Control During Wet-Chemical Powder Synthesis., *Advanced Ceramic Materials,* **3**:p.131-137, (1988).

[19] Lange, F. F., Sinterability of Agglomerates Powders., *Journal of the American Ceramic Society,* **67**(2): p.83-89, (1984).

[20] Chen, C. C., Nasrallah, M.M., Anderson, H.U., Synthesis and Characterization of $(CeO_2)_{0.8}(SmO_{1.5})_{0.2}$ Thin Films from Polymeric Precursors., *Journal of the Electrochemical Society,* **140**(12): p.3555-3560, (1993).

[21] Huang, K., Feng, M., Goodenough, J.B., Synthesis and Electrical Properties of Dense $Ce_{0.9}Gd_{0.1}O_{1.95}$ Ceramics., *Journal of the American Ceramic Society,* **81**(2): p.357-362, (1998).

[22] Anderson, H. U., Chen, C.C., Wang, J.C., Pennell, M.J., Synthesis of Conducting Oxide Films and Powders from Polymeric Precusors., in *Third International Conference on Powder Processing Science,* p.749-755, (1990). San Diego, USA.

[23] Pennell, M. J., The Development of the Ethylene Glycol Process for the Synthesis of Ceramic Oxides., Ceramic Engineering, University of Missouri-Rolla, (1988)

[24] *The Columbia Encyclopedia*, Columbia University Press, (2001).

[25] Rao, S. V. V., Rao, R.V.G., Biswas, A.B., Thermal Decomposition of Cerous Oxalate and Variation of Surface Area of the Products., *Journal of the American Ceramic Society,* **47**(7): p.356-360, (1964).

[26] Yan, M. F., Effects of Physical, Chemical, and Kinetic Factors on Ceramic Sintering., p.635-669, in *Advances in Ceramics, Vol 21: Ceramic Powder Science*, Messing, G. L., Mazidiyasni, K.S., McCauley, J.W., Haber, R.A. (ed.), The American Ceramic Society Inc., (1987).

[27] de With, G., Process Control in the Manufacture of Ceramics., p.28-67, in *Processing of Ceramics - Part I*, Brook, R. J. (ed.), VCH, (1995).

[28] Yan, M., Densification and Microstructural Development During Ceramic Processing., in *First China-Us Bilateral Seminar on Inorganic Materials Research,* p.160-124, (1983). Shanghai.

[29] Bortzmeyer, D., Die Pressing and Isostatic Pressing., p.126-151, in *Processing of Ceramics - Part I*, Brook, R. J. (ed.), VCH, (1995).

[30] Zheng, J., Carlson, W.B., Reed, J.S., Dependence of Compaction Efficiency in Dry Pressing on the Particle Size Distribution., *Journal of the American Ceramic Society,* **78**(9): p.2527-2533, (1995).

[31] Cahn, J. W., Heady, R.B., *Journal of the American Ceramic Society,* **53**(7): p.406-409, (1970).

[32] Bonekamp, B. C., Veringa, H.J., Green Microstructures and Their Characterization., p.341-387, in *Processing of Ceramics - Part I*, Brook , R. J. (ed.), VCH, (1995).

[33] Bortzmeyer, D., Dry Pressing of Ceramic Powders., p.102-146, in *Ceramic Processing*, Terpstra, R. A., Pex, P.P.A.C., de Vries, A.H. (ed.), Chapman and Hall, (1995).

[34] Eisele, U., Sintering and Hot Pressing., p.83-98, in *Processing of Ceramics - Part II*, Brook, R. J. (ed.), VCH, (1996).

[35] Lange, F. F., Contributions of Sintering and Coarsening to Densification: A thermodynamic approach., p.57-70, in *Advanced Ceramics III*, Somiya, S. (ed.), Elsevier Science Publishers Ltd, (1990).

[36] Chiang, Y.-M., Birnie, D., Kingery, W.D., *Physical Ceramics: Principles for Ceramic Science and Engineering.*, John Wiley and Sons, Inc., (1997).

[37] Whiston, C., *X-Ray Methods*, ACOL, (1987).

[38] Hong, S. J., Virkar, A.V., Lattice Parameters and Densities of Rare-Earth Oxide Doped Ceria Electrolytes., *Journal of the American Ceramic Society,* **78**(2): p.433-439, (1995).

[39] Shannon, R. D., Revised Effective Ionic Radii and Systematic Studies of Interatomic Distances in Halides and Chalcongenides., *Acta Crystallographica, Section A,* **A32**(5): p.751-767, (1976).

[40] Starbuck, J. W., Introduction to Powder Diffraction., in *Hand Book of X-rays*, Kaelble, E. F. (ed.), McGraw-Hill Book Company, (1967).

[41] Weller, M. T., *Inorganic Materials Chemistry*, Oxford University Press, (1994).

[42] Cullity, B. D., *Elements of X-ray Diffraction*, Addison-Wesley Publishing Company, Inc., (1978).

[43] McKinstry, H. A., Huang, C.-Y., McKinstry, S.T., Thermal Expansion by X-ray Diffraction., in *Thermal Expansion of Solids*, Ho, C. Y. (ed.), ASM International, (1998).

[44] Azaroff, L. V., Pease, D.M., X-ray Absorption Spectra, in *X-ray Spectroscopy*, Azaroff, L. V. (ed.), McGraw-Hill, (1974).

[45] Brunauer, S., Emmett, P. H., Teller, E., *Journal of the American Chemical Society,* **60**:p.309-319, (1938).

[46] Bulkin, B. J., The Raman Effect: An Introduction., p.1-19, in *Analytical Raman Spectroscopy*, Grasselli, J. G., Bulkin, B.J. (ed.), John Wiley and Sons, Inc., (1991).

[47] Gardiner, D. J., Graves, P.R., *Practical Raman Spectroscopy.*, Springer-Verlag, (1989)

[48] Tompsett, G. A., Characterisation and Phase Equilibria of Doped-Bi_2O_3 and Doped-CeO_2 Systems., PhD Thesis, Department of Technology, The University of Waikato, (1997)

[49] Christie, G. G., van Berkel, F.P.F., Microstructure - Ionic Conductivity Relationships in Ceria-Gadolinia Electrolytes., *Solid State Ionics,* **83**:p.17-27, (1996).

[50] Jiang, S. P., Love, J.G., Badwall, S.P.S., Electrochemical Techniques in Studies of Solid Ionic Conductors., in *Electrical Properties of Oxide Materials.*, Nowotny, J., Sorrell, C.C. (ed.), Trans Tech Publications, (1997).

[51] Rogers, G. F. C., Mayhew, Y.R., *Thermodynamic and Transport Properties of Fluids*, Basil Blackwell, (1982).

[52] Institute of Geological & Nuclear Sciences Limited (IGNS), New Zealand., Ion Beam Analysis (IBA) Methods., *http://www.gns.cri.nz/help/laboratory/ibameth.html*

[53] Sammes, N. M., Markwitz, A., Keppeler, F.M., Tompsett, G.A., The Use of Solid State NMR and Rutherford Back Scattering to Study $La_{0.8}Sr_{0.2}Ga_{0.85-x}Co_xMg_{0.15}O_{3-d}$., in *Solid Oxide Fuel Cells VI,* p.292-301, (1999). Hawaii.

[54] Markwitz, A., Materials Processing - Elemental Analysis with Ion Beams., in *First International Conference on Advanced Materials Processing.*, p.135-140, (2000). Rotorua, New Zealand.

[55] Experimental Nuclear Physics Laboratory of the University of Liège, Belgium, PIXE (Particle Induced X-ray Emission) Y (a,a'X) Y, *http://www.pne.ulg.ac.be/ipne/iba/pixe.html*

[56] Charles Evans & Associates, RBS Theory - Introduction, *http://www.cea.com/cai/rbstheo/intro.htm*

Chapter Three

3 Experimental Method

3.1 Overview

This chapter contains the details of the experimental methods performed during the course of this work. The details are divided into powder preparation, sample preparation and sample characterisation sections.

3.2 Powder Preparation

The ceramic powders used for this research were produced using two wet chemical methods, a co-precipitation technique and a modified Pechini method. The resulting intermediate products from the two methods required calcination to produce the desired oxide material.

3.2.1 Co-precipitation

A variation of the co-precipitation method, termed reverse strike was used, the method being based on work performed by Van Herle *et al.*[1].

- Stoichiometric amounts of the required metal nitrates were dissolved in distilled water and stirred for 20 minutes to form an aqueous solution of 1 M total metal ion concentration.
- The nitrate solution was added drop-wise to 0.06 M oxalic acid with constant stirring. The oxalic acid solution having previously been adjusted to a pH of 6.7-6.9 by the addition of ammonia solution.
- The precipitant solution was maintained in the pH range of 6.7-6.9 by addition of ammonia solution during the nitrate addition.

- Once the nitrate solution had been added the mixture was left stirring over night.

The resulting precipitate was filtered using a Buchner funnel and flask, washed five times with distilled water followed by five times with isopropanol. The washed powder was dried over night in a 50 °C oven. The oxalate powder produced was calcined to obtain the oxide.

3.2.2 Modified Pechini Method

A variation on the Pechini method was employed, where nitric acid is used in place of citric acid. The method used is that reported by Chen *et al.*[2], though used here to produce a bulk powder rather than a thin film.

- Stoichiometric amounts of the required metal nitrates were dissolved in distilled water to form an aqueous solution. The amount of water used was 10 mL water for each 0.02 mole of metal ions.

To this solution ethylene glycol was added at the ratio of 40 mL to each 0.02 mole of metal ions.

- Finally concentrated nitric acid was added, the volume being equal to that of the water used to dissolve the nitrates.
- The mixture was heated, with stirring, at 80 °C for 80 hours.

During the heating process volatile matter is driven off and the volume of the mixture decreases. At the end of 80 hours a viscous liquid has formed.
The gel was carefully calcined to obtain the oxide powder.

3.2.3 Materials Used

Table 3.1 gives the details and purities of the materials used for powder preparation.

Table 3.1 Raw Materials used.

Material	Manufacturer	Purity (%)
$Ce(NO_3)_3.6H_2O$	Acros Organics	99.5
$Gd(NO_3)_3.6H_2O$	Aldrich Chemical Company Inc.	99.9
$Sm(NO_3)_3.6H_2O$	Aldrich Chemical Company Inc.	99.9
$Pr(NO_3)_3.6H_2O$	Aldrich Chemical Company Inc.	99.9
Oxalic acid $(COOH)_2$	BDH Chemicals	Lab reagent grade
Ammonia solution - 28%	Ajax Chemical	Analytical reagent grade
Nitric acid - 69%	BDH Chemicals	AnalaR
Ethylene glycol	BDH Chemicals	99.5

3.2.4 Calcination

The materials produced from both of the preparation methods were calcined for 1 hour at 700 °C. However the calcining regimes were different. The gel produced by the Pechini method was found to undergo a large volume expansion on decomposition, this was thought to warrant a slower heating rate to minimise problems.

Calcinations were carried out in a muffle furnace (K2 F/L, B & L Tetflow), equipped with a Shimaden SR58 temperature controller.

Figure 3.1 shows the heating regime used for calcining the co-precipitation powder. Figure 3.2 shows the heating regime used for the Pechini Gel.

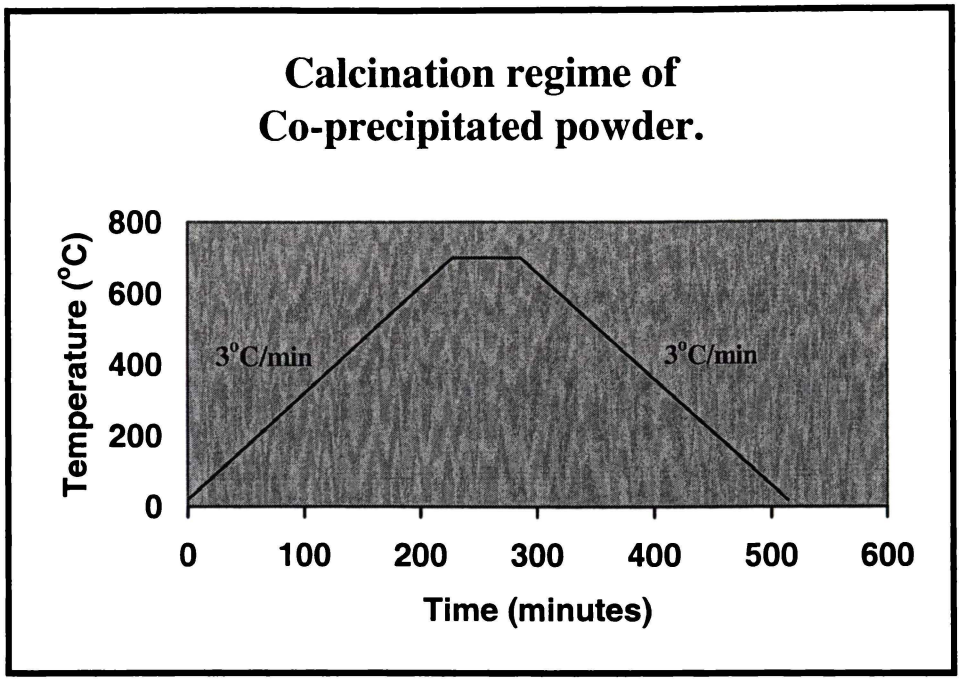

Figure 3.1 Calcination Regime of Co-precipitated Powder.

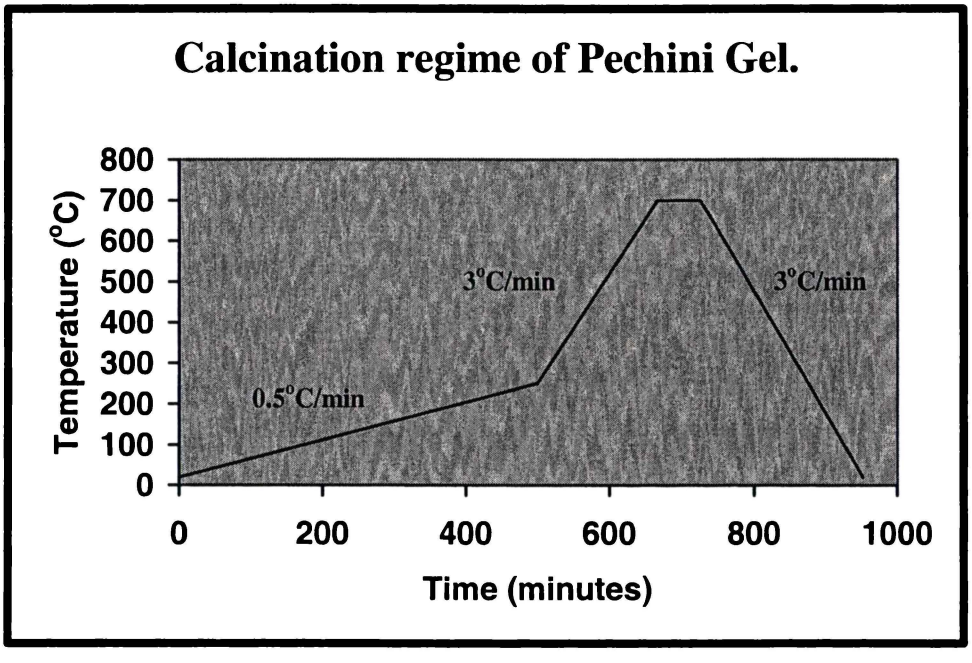

Figure 3.2 Calcination Regime of Pechini Gel.

3.3 Sample Preparation

The oxide powders produced through the calcination process were formed into solid pellets through the formation of green compacts followed by a sintering process.

3.3.1 Compact Formation

Pressed powder compacts were formed by initial uniaxial pressing at 14 MPa to produce a pellet with a diameter of approximately 14 mm. These preformed pellets were cold isostatically pressed at 200 MPa in an isostatic press (FPG2347, Stansted Fluid Power Limited). The isostatic pressing of the pellets was achieved via a 'wet-bag'[3] method, whereby the sample was placed in a disposable rubber envelope which was then evacuated, sealed and pressed.

Binder Use

A binder/lubricant was used after initial problems of poor compact strength and inability to consistently form coherent compacts through uniaxial pressing. The binder/lubricant used was oleic acid (Ajax Chemicals, laboratory reagent grade) at a level of 3 wt%. The binder was thoroughly mixed through the powder by milling the powder and binder/lubricant overnight in a high density polyethylene bottle with partially-stabilised zirconia milling media.

3.3.2 Sintering

Pressed powder compacts were sintered in a high temperature furnace (HT05/18, Ceramic Engineering), equipped with four Super Kanthal 1900 molydenum disilicide resistance heating elements, a Eurotherm 902 programmable controller and a Pt20%Rh - Pt40%Rh thermocouple. Initial sintering studies were performed to ascertain the optimum sintering regime. Pressed powder samples were sintered for either 2 or 10 hours at 1300, 1400, 1500 or 1600 °C.

Where no binder was employed the sintering regime consisted of a single step ramp to the desired temperature, refer Figure 3.3. In samples where a binder was employed an additional binder burn out step was added, refer Figure 3.4. Subsequent sinterings were performed at what was determined to be the optimum regime based on the initial study.

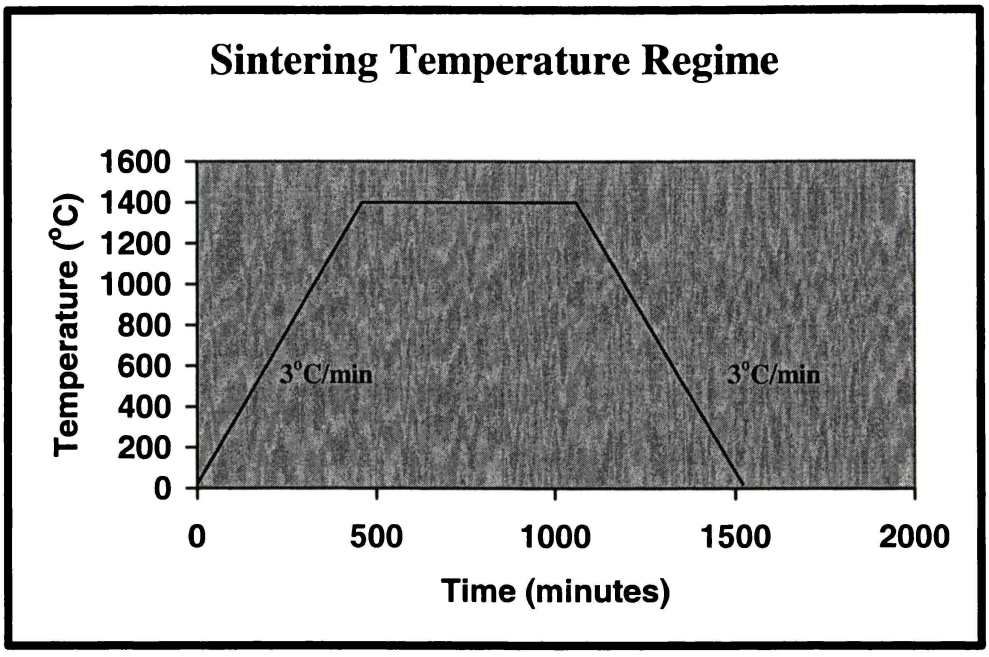

Figure 3.3 Sintering Regime for Binder Free Sample.

10 hours @ 1400 °C used as an example

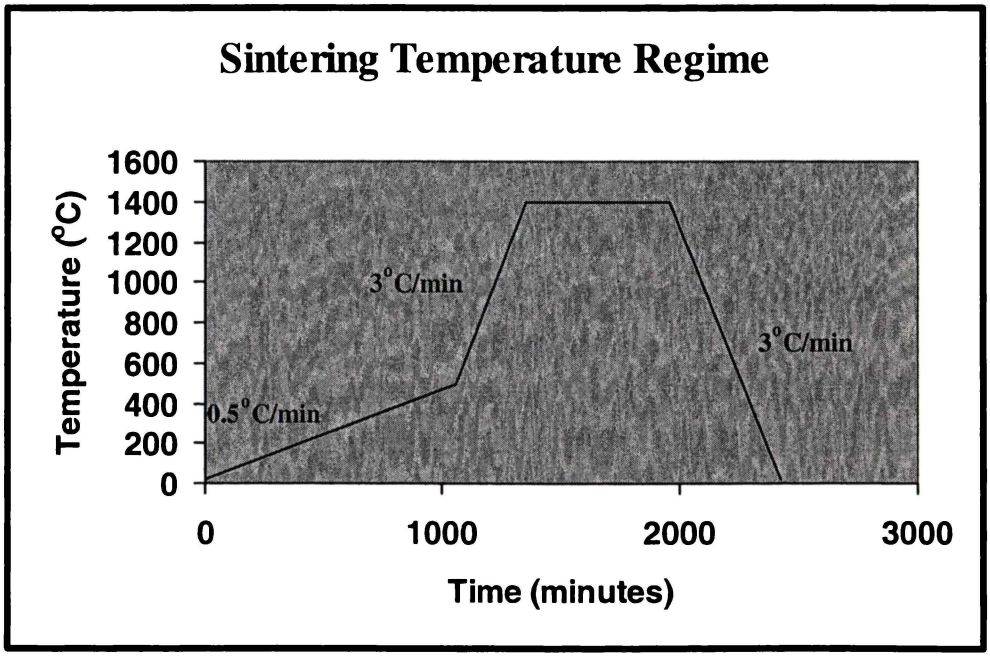

Figure 3.4 Sintering Regime for Binder Containing Sample.

10 hours @ 1400 °C used as an example

3.4 Sample Characterisation

Samples, either in powder form or as solid pellets were characterised and tested using a number of techniques. These included x-ray diffraction, electron and x-ray microscopy, surface area and particle size measurements, Raman spectroscopy and impedance spectroscopy.

3.4.1 Powder X-ray Diffraction

X-ray diffraction characterisation of powder samples was performed using a Philips X'Pert XRD system, diffractometer type PW3050/θ-2θ. Generator settings of 45 kV and 40 mA were used, with Cu Kα radiation, wavelength 1.54056 Å. Characterisation scans were run over the range of 2θ = 25-75°, step size of 0.02 °2θ, with a scan time of 1 second per step. The angle range was chosen based on literature review. Divergence and anti-scatter slits were set to automatic with a 0.20 mm receiving slit.
Philips Analytical PC-APD diffraction software (Phillips Electronics) was used for instrument control and data acquisition. Peak positions were determined from fitted profiles obtained using Phillips ProFit software (Phillips Electronics).

Crystallite size measurements were performed on the above system, using the (400) peak. A step size of 0.005 °2θ and scan time of 1.25 seconds per step was used. The Phillips ProFit software was used to obtain the half width values from which a crystallite size was calculated. A standard sample was prepared from CeO_2, calcined 10 hours at 1600 °C to ensure that the crystallite size would be greater than 1 μm.

Lattice parameters for the different compositions were determined from the peak positions in the XRD patterns and refined using the UnitCell software (Holland & Redfern).

3.4.2 High Temperature Powder X-ray Diffraction

X-ray diffraction measurements from 500 °C - 1000 °C were performed using a high temperature camera (HTK-16, Anton-Paar) fitted to the Phillips X'Pert XRD system detailed above. Temperature and scan programmes were controlled using the Phillips PC-APD software coupled with a temperature controller (TCU2000, Paar Physics). A platinum strip heating filament was used, equipped with two Pt - Pt10%Rh thermocouples. Samples were equilibrated at the scan temperature for 30 minutes prior to initiating the scan. The scan programme employed was identical to that used for room temperature characterisation scans, except that the time for each step was 1.25 seconds rather than 1 second.

3.4.3 X-ray Microscopy

X-ray microscopy was performed using a microfocus x-ray, MFX, device (HMX160, X-Tek Systems Limited), Figure 3.5. This was equipped with a 5 axis sample stage, 150mm x-ray sensitive image intensifier (TH9449, Thompson Tubes Electroniques) with a charge coupled device, CCD, camera (TM-6CN, Pulnix). Images were obtained by passing the signal through an in-line image processor (Argus 20, Hamamatsu Photonics Limited) and sampling the real-time image using PC_Image software (Foster Findlay Associates). X-ray energies employed varied depending on the sample, thicker samples requiring higher energy x-rays to discern sample features. The Argus 20 was used as a coarse image adjustment, while the PC_Image software was used for subsequent, finer, image definition and contrast adjustments.

Figure 3.5 X-Tek HMX 160 System[4].

3.4.4 Surface Area Determination

Surface areas of powders were determined using a BET method, performed on a Nova 1000 gas sorption analyser. Samples were outgassed for 18 hours at 250 °C.

3.4.5 Particle Size Analysis

Powder particle size analysis, in addition to SEM observation, was performed using a Mastersizer S laser diffraction system (Malvern Instruments) equipped with a MS17 sampler. A 300 RF mm range lens was employed, beam length was 2.40 mm. The powder sample was dispersed in water and ultrasound applied during the measurement process.

3.4.6 Raman Spectroscopy

Raman spectroscopy was undertaken on sintered samples using a Raman spectrometer (System 2000, Renshaw), equipped with a microscope stage for analysing small samples with 180° incident geometry. A 782 nm near infra-red laser line laser, with an 8 mW incident power was employed to excite laser Raman spectra. Spectra were obtained using an uncoated Olympus x50 objective lens with spectra being the averaged of 5 scans at 60 seconds per scan.

3.4.7 Scanning Electron Microscopy

Scanning electron microscopy, SEM, was performed using a Hitachi S4000 SEM. SEM was used to examine the powders produced with respect to particle size and shape. All samples were coated with a thin film of Pt/Pd using an ion sputterer (E1030, Hitachi). The surfaces of polished sintered pellets were examined to determine grain size, grain shape and visible porosity.

Backscattered electron imaging was performed on the above system, equipped with a Robinson Detector module.
Energy dispersive x-ray analysis of the samples was performed on the above system equipped with a Kevex Quantum Window x-ray detector, passed through a signal processor (Model 500, IXRF Systems Inc.) and analysed using the EDS2000 software package (version 2.4, IXRF Systems Inc.)

Sample Preparation for SEM

Sintered pellets were ground and polished using a Struers RotoPol 21 polishing machine. Samples were ground successively with 800, 1000 and 4000 grit SiC papers (Struers). Following grinding, samples were polished using 3 and 1 μm diamond fluid (Struers) retained on a cloth coated polishing plate (MD-DUR, Struers).

Subsequent to polishing the samples were thermally etched for 1 hour at 1000°C.

3.4.8 Density Measurements

Bulk Density

The density of sintered pellets was measured using an Archimedes method[5]. In this method the dry weight of the pellet was first recorded, the sample was boiled 30 minutes in distilled water. After blotting dry the sample is reweighed, the open porosity of the sample having been filled with water. The pellet was suspended in water and reweighed. The bulk density, ρ_B, can then be calculated using Equation 3.1.

$$\rho_B = \frac{W_d}{W_w - W_s} \qquad 3.1$$

where:

W_d = weight of dry sample

W_w = weight of wet sample

W_s = weight of samples suspended in water

Theoretical Density

The theoretical density was determined using the XRD data obtained for the samples. The d-spacings obtained from the diffraction patterns allowed the calculation of lattice parameters, and hence cell volume, using the UnitCell programme (T.J.B. Holland & S.A.T. Redfern). The unit cell volume was used in Equation 3.2 to calculate the theoretical density of the material.

$$\rho_T = \frac{M.z}{V.N_A} \qquad 3.2$$

where:

M = relative molar mass

z = number of formula units in the cell

V = unit cell volume

N_A = Avogardro's number

Once bulk and theoretical densities had been determined, the bulk density could be expressed as a percentage of the theoretical.

3.4.9 Impedance Spectroscopy

The pellets used for impedance spectroscopy were prepared by coating the flat surfaces of the sintered pellet with platinum ink, which was sintered at 1000 °C for 1 hour. Samples were placed in a quartz sample holder, capable of holding 4 samples simultaneously, Figure 3.6. Coiled platinum wires were pressed onto the platinised surfaces of the samples, with sintered alumina spacers used to prevent contact between adjacent samples and their associated platinum wires, lower inset of Figure 3.6.

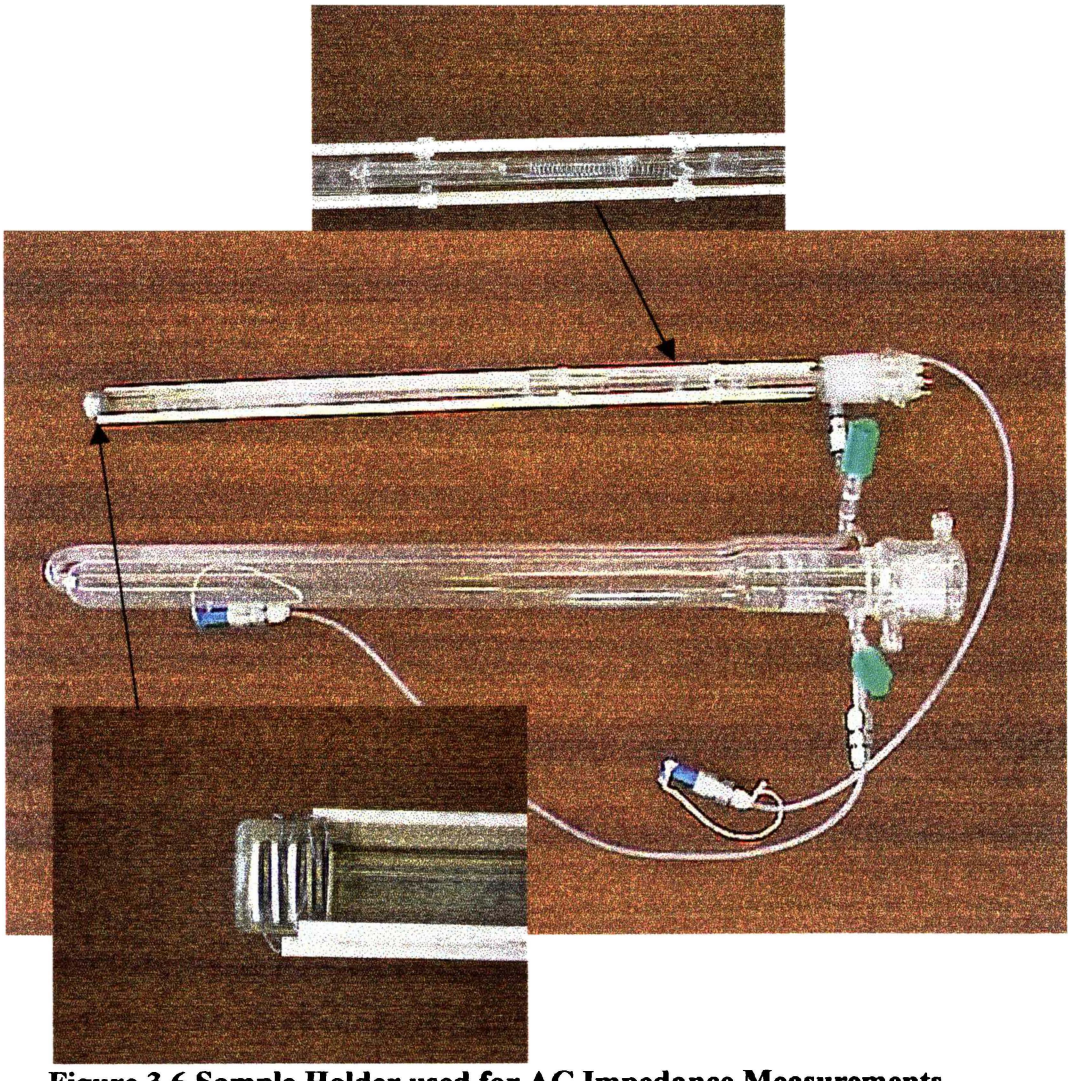

Figure 3.6 Sample Holder used for AC Impedance Measurements.

The whole sample holder assembly was spring-loaded to ensure continuing contact between the samples and platinum wires, upper inset of Figure 3.6. The quartz holder, was placed in a tube furnace (HTF 7060, Ceramic Engineering), equipped with a Eurotherm 902 programmable temperature controller.

AC impedance spectroscopy measurements were performed using a Solartron 1260 Impedance/Gain-Phase Analyser, sweeping from 0.1 Hz to 10 MHz, with a 10 mV AC amplitude applied. The ZPlot software (Scribner Associates Inc.) programme was used to control the Solartron 1260, with the ZView programme (Scribner Associates Inc.) used to collect and analyse the data.

Effect of Temperature

The effect of temperature on the impedance spectrum was evaluated by heating the samples from 300 °C to 600 °C in 50 °C steps. At each temperature the sample was equilibrated for 1 hour before taking measurements. Samples were tested as the temperature was decreased from the 600 °C maximum in 50 °C steps.

Effect of Oxygen Partial Pressure

The effect of oxygen partial pressure on the impedance spectrum was evaluated. The samples were maintained at the one temperature and supplied with gas mixtures with successively lower oxygen partial pressures. Differing oxygen partial pressures were generated by passing calibrated mixtures of N_2/H_2 through a temperature controlled distilled water bubbler and then into the quartz sample holder. Heated gas lines were used to prevent condensation of water vapour from the gas mix. Samples had an initial 8 hour equilibration time with impedance spectra collected at 4 hour intervals after the eight hours, until the sample's impedance spectrum stabilised, that is there was no difference between a spectrum and its predecessor, recorded 4 hours earlier. Due to time constraints only samples of CG, CGP015 and CGS01 were tested at different partial pressures.

3.4.10 Differential Thermal Analysis

Differential thermal analysis, DTA, and thermogravimetric analysis, TGA, were performed on a simultaneous DTA/TGA device (SDT 2960, TA Instruments). Approximately 5 mg of gently oven-dried sample was placed in an alumina sample crucible and heated from 35 °C to 950 °C at a rate of 20 °C/min in air. Device control and data collection were performed using Thermal Solutions software (TA Instruments Inc.). Subsequent data analysis was performed using the Thermal Solutions release of Universal Analysis (TA Instruments Inc.)

3.4.11 Ion Beam Analysis, IBA

Broad beam IBA measurements were performed under high-vacuum conditions using a 3 MV Van-de-Graaff accelerator.

Nuclear Reaction Analysis, NRA

In order to determine oxygen concentration in the samples 920 eV deuterium ions, $^{2}H^{+}$, were used as the incident ions. Protons from the nuclear reaction $^{16}O(D,p_1)^{17}O$ (proton energy 1.87 MeV, cross section 4.6 mb/str) were detected by means of a surface barrier detector placed at a backscattering angle of 150°. A thin, 14 μm, mylar foil was attached to the front of the detector to trap backscattered deuterons. The depth of penetration of the sample was approximately 5.8 μm. Concentration values are based on the use of standards, the limit of detection for NRA is known to be approximately 1 ppm[6].

Particle Induced X-ray Emission, PIXE

PIXE was performed using 2.5 MeV $^{1}H^{+}$. The x-rays produced were detected using a high resolution x-ray detector equipped with a thin film attachment to optimise the x-ray yield. The spectra produced were evaluated using the GUPIX code[7].

Rutherford Backscattering Spectrometry, RBS

RBS was performed using 3.0 MeV $^4He^+$. The back-scattered ions were detected using a surface barrier detector at a back-scatter angle of 150°. The backscattering spectra was evaluated using the RUMP code[8]. RBS is a 'standard free' analysis technique, spectra are simulated using the RUMP code considering different elemental compositions at different depths.

Bibliography

[1] Van Herle, J., Horita, T., Kawada, T., Sakai, N., Yokokawa, H., Dokiya, M., Low Temperature Fabrication of (Y, Gd, Sm)-doped Ceria Electrolyte., *Solid State Ionics,* **86-88**:p.1255-1258, (1996).

[2] Chen, C. C., Nasrallah, M.M., Anderson, H.U., Synthesis and Characterization of $(CeO_2)_{0.8}(SmO_{1.5})_{0.2}$ Thin Films from Polymeric Precursors., *Journal of the Electrochemical Society,* **140**(12): p.3555-3560, (1993).

[3] de With, G., Process Control in the Manufacture of Ceramics., p.28-67, in *Processing of Ceramics - Part I*, Brook, R. J. (ed.), VCH, (1995).

[4] Keele University, United Kingdom, 'X-Ray Technology' at Keele University, *http://www.keele.ac.uk/depts/ch/services/xray/new_page_2.htm*

[5] Grimshaw, R. W., *The Chemistry and Physics of Clays.*, John Wiley & Sons Inc., (1971).

[6] Sammes, N. M., Markwitz, A., Keppeler, F.M., Tompsett, G.A., The Use of Solid State NMR and Rutherford Back Scattering to Study $La_{0.8}Sr_{0.2}Ga_{0.85-x}Co_xMg_{0.15}O_{3-d}$., in *Solid Oxide Fuel Cells VI,* p.292-301, (1999). Hawaii.

[7] Maxwell, J. A., Campbell, J.L., Teesdale, W.J., The Guelph PIXE Software Package., *Nuclear Instruments and Methods in Physics Research,* **B43**:p.1989, (1989).

[8] Doolittle, L., Algorithms for the Rapid Simulation of Rutherford Backscattering Spectra., *Nuclear Instruments and Methods in Physics Research,* **B9**:p.334, (1985).

Chapter Four

4 Results and Discussion

4.1 Overview

This chapter contains the discussion of the results obtained using the experimental methods described in Chapter 3. The results are divided into three sections: Powder Characterisation, Pellet Characterisation and Impedance Spectroscopy.

4.1.1 Sample Codes

Throughout this chapter samples are referred to using abbreviated sample composition codes. The sample compositions and their corresponding codes are given in Table 4.1

Table 4.1Composition Codes Used for Sample Identification.

Composition	Code
$Ce_{0.8}Gd_{0.2}O_{2-\delta}$	CG
$Ce_{0.8}Gd_{0.195}Pr_{0.005}O_{2-\delta}$	CGP005
$Ce_{0.8}Gd_{0.19}Pr_{0.01}O_{2-\delta}$	CGP01
$Ce_{0.8}Gd_{0.185}Pr_{0.015}O_{2-\delta}$	CGP015
$Ce_{0.8}Gd_{0.17}Pr_{0.03}O_{2-\delta}$	CGP03
$Ce_{0.8}Gd_{0.15}Pr_{0.05}O_{2-\delta}$	CGP05
$Ce_{0.8}Gd_{0.19}Sm_{0.01}O_{2-\delta}$	CGS01
$Ce_{0.8}Gd_{0.17}Sm_{0.03}O_{2-\delta}$	CGS03
$Ce_{0.8}Gd_{0.15}Sm_{0.05}O_{2-\delta}$	CGS05

Samples, in addition to a composition code, may also have an indication of the preparation method employed for their fabrication - either the modified Pechini method (abbreviated to Pechini), or co-precipitation (abbreviated to coppt) – this is only applicable to the composition codes CG, CGP03 and CGS03. All other compositions have been prepared by the co-precipitation method only. If there is no indication of preparation method then the material has been prepared by co-precipitation.

4.2 Powder Characterisation

The powder characterisation section contains experimental observations of interest noted during the preparation of the powders, results of the various methods used to characterise the powders and in some cases their precursor materials. The methods used include thermal analysis, x-ray diffraction, SEM investigation, particle size and surface area measurements.

4.2.1 Experimental Observations

There was little variation noted between the differing compositions of the sample powders prepared by the co-precipitation technique with regard to how the preparation proceeded.

This was not the case for samples prepared by the Pechini method. The CG and CGP03 mixtures reduced down to a viscous brown liquid when the procedure outlined in section 3.2.2 was followed. However the CGS03 intermediate product differed from those obtained for the CG and CGP03 samples. The CGS03 mixture reduced down to a yellow 'solid', see Figure 4.1. The term solid is used loosely as on standing overnight the material would settle and fill a vessel, indicating that it was more an extremely viscous liquid. The experimental procedure was repeated to confirm this observation The second batch produced a similar precursor material to that of the first batch, it was therefore concluded that the different double dopant had caused the effect rather than some external contamination.

the different double dopant had caused the effect rather than some external contamination.

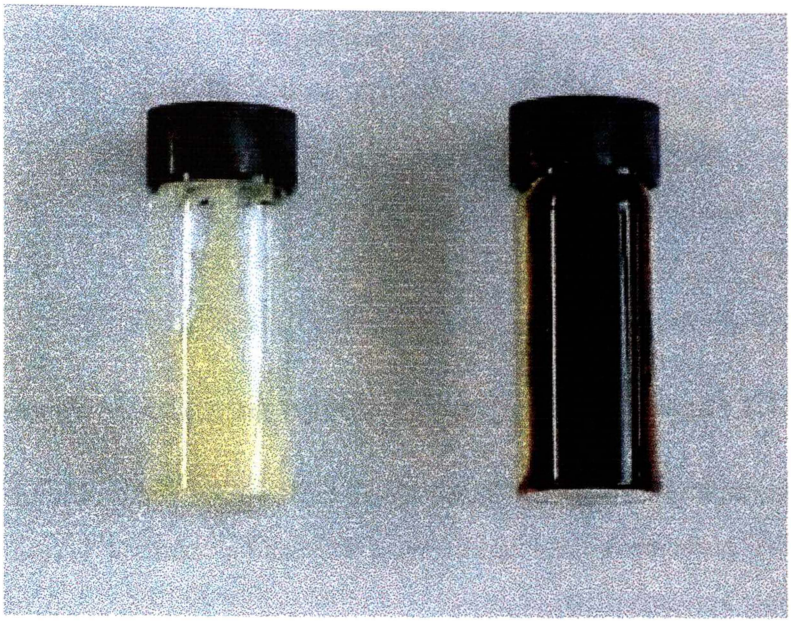

Figure 4.1 Photo of CGS03 (left) and CGP03 (right) Pechini Precursors.

On calcination, the viscous liquid precursor of the CG and CGP03 Pechini material showed a marked increase in volume occupied, expanding to fill the vessel it was calcined in; the calcined product of these two precursors appeared highly porous. In comparison the CGS03 Pechini precursor showed only a slight increase in volume occupied, occupying only a slightly larger volume than the precursor material. While still appearing porous, it was not to the same extent as that of the calcined CG and CGP03 materials.

Colour Variation

It was noted that with increasing praseodymia levels the sample powders showed a proportional darkening of colour. The, as calcined, CG material was very pale ivory/apricot in colour, with increasing praseodymia the colour darkened, with the CGP05 sample exhibiting an orange-beige colouration, see Figure 4.2.

Figure 4.2 Photo of CG (left) and CGP05 (right) Calcined Powders.

There was only a slight colour variation discernable in the samaria double doped powders. The powders being darker with increasing samaria levels but still remaining a pale apricot colour.

A similar colour variation was noted in the sintered pellets. The sintered CG pellets being an orange-brown. The pellets produced from praseodymia-containing powders were significantly darker, even at the lowest double dopant level. CGP005 pellets were dark brown in colour, with CGP05 pellets being dark grey, see Figure 4.3.

Figure 4.3 Photo of CG (left) and CGP05 (right) Sintered Pellets.

Samaria double doped pellets also showed colour variation but not as extreme as the praseodymia double doped pellets.

In undoped ceria a darkening of the sample would indicate a partial reduction of Ce^{4+} to Ce^{3+}[1]. Griffiths et al.[2] found that when undoped ceria was treated under reducing conditions it changed from a yellow colour to blue, however this blue colouration did not occur when doped with trivalent rare-earth oxides. It was also noted[2] that the addition of Pr(III) facilitated the reduction of ceria. Ceria is known to be especially sensitive to the presence of other lanthanides with respect to colour change[3]. Gao and Sammes[4] note the correlation between colour and band gap, and that lighter coloured materials are more likely to be good ionic conductors.

The colour change may simply be due to the presence of the different dopant elements; however if the colour change is due to reduction of ceria, the induced electronic conduction will be detrimental to electrolyte performance.

Effect of Milling

The only observation of note, with respect to the effect milling had on the powders, was that dry milled Pechini CG powder was more flowable and less prone to clumping. These properties are generally characteristic of a powder having a larger particle size, compared to less flowable clumping powders[5, 6].

4.2.2 Thermal Analysis

Thermal analysis was performed on the oxalate precursors of the base material - CG, CGP05 and CGS05 in order to determine the number of oxalate species present. The formation of a single mixed metal oxalate species was the desired outcome of the co-precipitation method. Van herle et al.[7] have shown that the formation of separate metal oxalates, as opposed to a single mixed metal oxalate, leads to an inferior oxide product. It was considered that these three compositions would be the most likely to exhibit the formation of separate co-precipitates as they, respectively, contain the highest concentration of a single dopant ion and the highest concentrations of the secondary dopant ions.

The presence of separate co-precipitates should give rise to an exothermic oxalate decomposition peak for each of the oxalates associated with a particular metal, rather than a single decomposition peak for the mixed metal co-precipitate.

The decomposition temperatures of the single metal oxalates are listed in Table 4.2. In Table 4.2, where two decomposition temperatures for a particular oxalate are listed, from a single reference source, then the oxalate first decomposes to an intermediate oxycarbonate ($M_2O_3.CO_2$) and then to the oxide species.

Table 4.2 Literature Oxalate Decomposition Temperatures.

Oxalate	Decomposition Temperature (°C)
Ce	275-375[1], 325-400[2]
Gd	400-500 & 575-675[2]
Pr	375-475 & 575-650[1]
Sm	380-480 & 550-650[2]

[1] from reference [8]

[2] from reference [9]

As can be seen from

Figure 4.4 all three of the samples tested show a single strong exothermic peak, indicating that the co-precipitation method employed produced mixed metal oxalates. Although the initial decomposition temperatures of the single metal oxalates could possibly overlap or mask one another, the absence of a second peak at higher temperatures is a strong indication that a cerium solid solution oxalate has been formed. This observation is based on the fact that cerium oxalate does not decompose via an intermediate oxycarbonate[8], however the other possible metal oxalates do. This two step decomposition leads to the presence of a peak at approximately 400 °C, with the second peak occurring in the range of 550 - 650 °C.

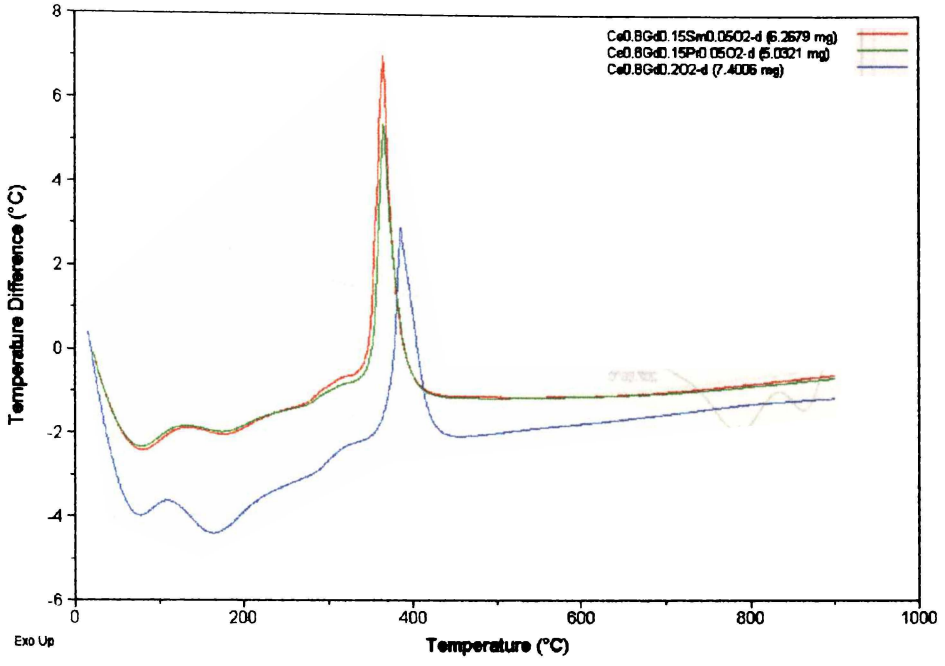

Figure 4.4 DTA Trace of Oxalate Precursors.

The peaks present in the range of 50 - 300 °C are associated with the successive loss of the water of crystallisation[9-11]. The large exothermic peak is attributed to the decomposition of the oxalate to the oxide[8, 9, 12].

The double doped samples have almost identical traces; the base material (CG), while maintaining the general form of the other traces, has a greater initial endothermic process and the strong oxalate decompostion peak occurs at a slightly higher temperature. Individual DTA traces for the three samples are shown in Figure 4.5 - Figure 4.7.

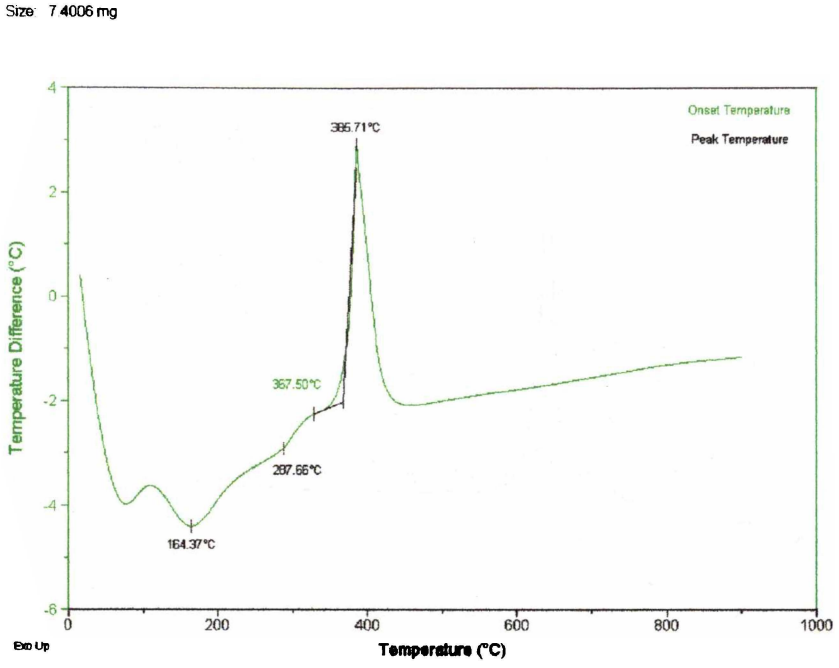

Figure 4.5 DTA Trace of CG Oxalate.

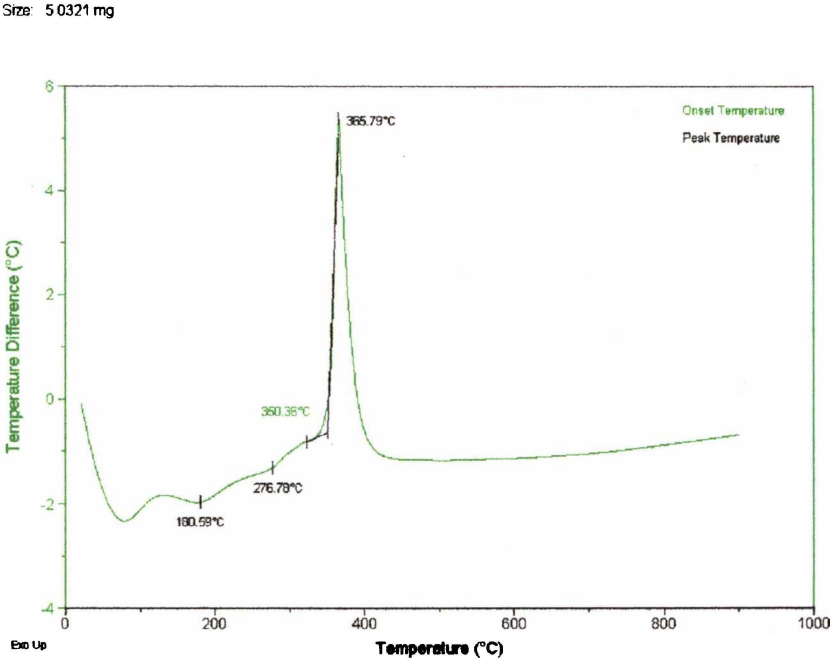

Figure 4.6 DTA Trace of CGP05 Oxalate.

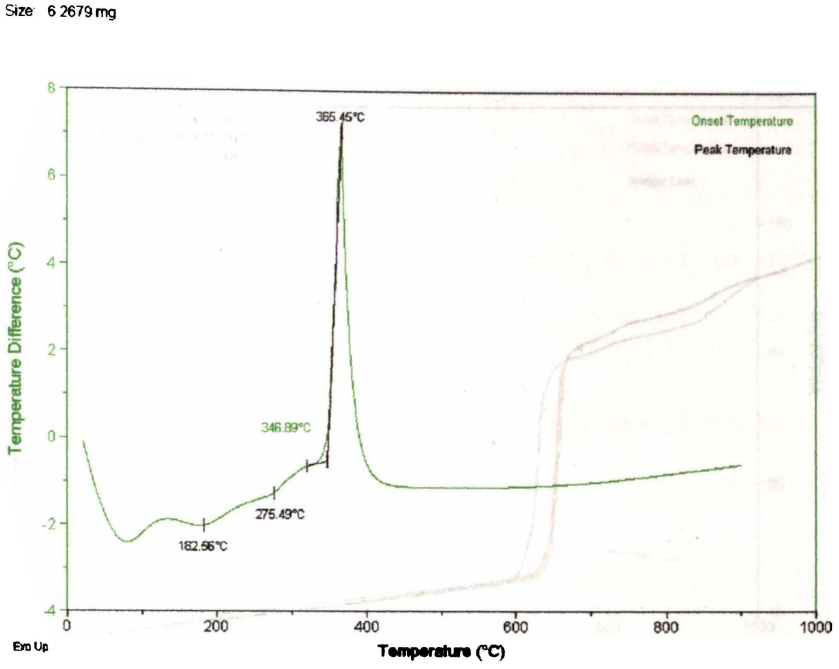

Figure 4.7 DTA Trace of CGS05 Oxalate.

Figure 4.8 shows the weight loss associated with the dehydration and decomposition of the oxalate materials. It can be seen that the weight loss of the double doped oxalates is very similar; while the CG oxalate has a higher weight loss from the initial dehydration step, there is a comparable weight loss from the decomposition of the oxalate.

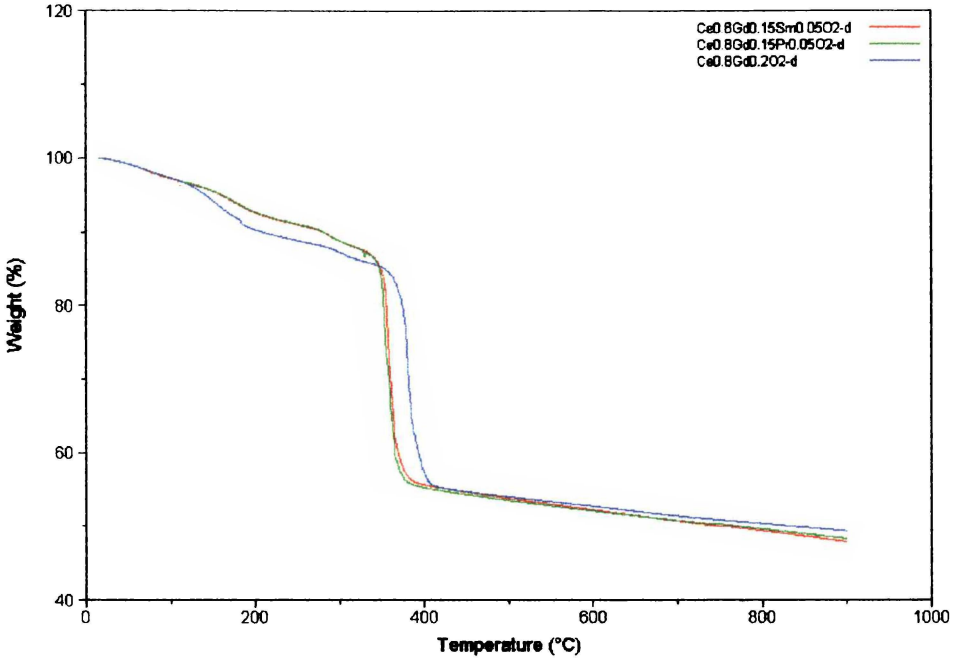

Figure 4.8 TGA Trace of Oxalate Precursors.

Individual TGA traces of the oxalate species are shown in Figure 4.9 - Figure 4.11.

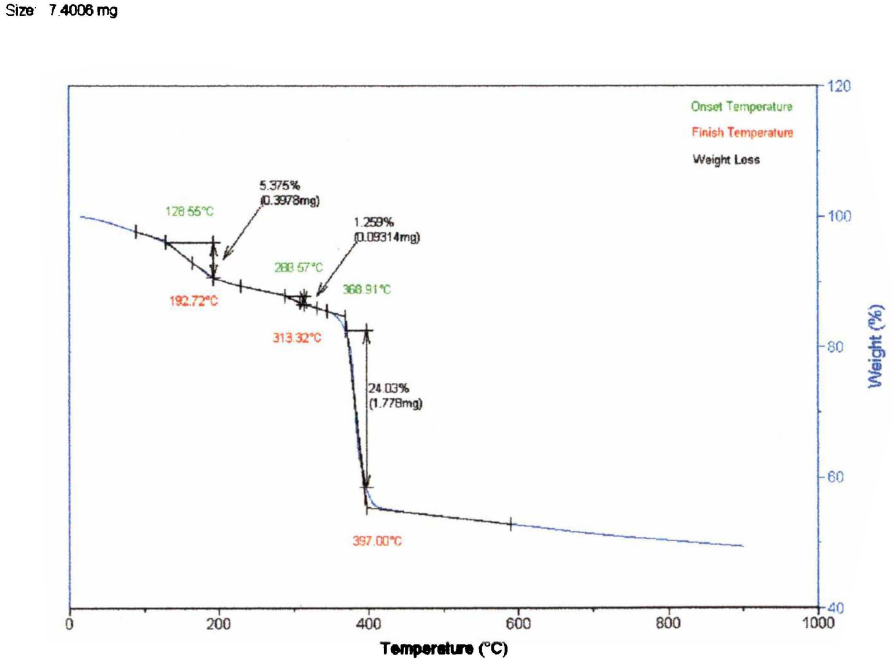

Figure 4.9 TGA Trace of CG Oxalate.

Size: 5.0321 mg

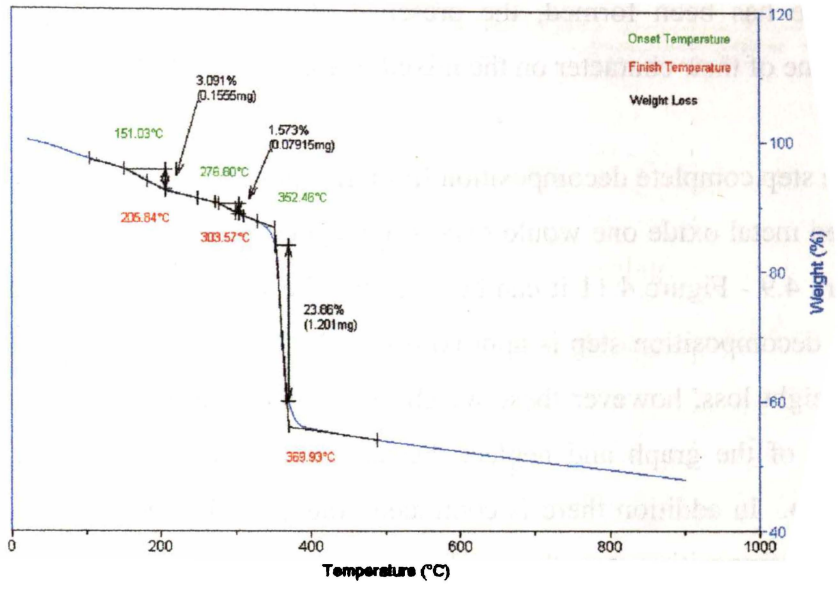

Figure 4.10 TGA Trace of CGP05 Oxalate.

Size: 6.2679 mg

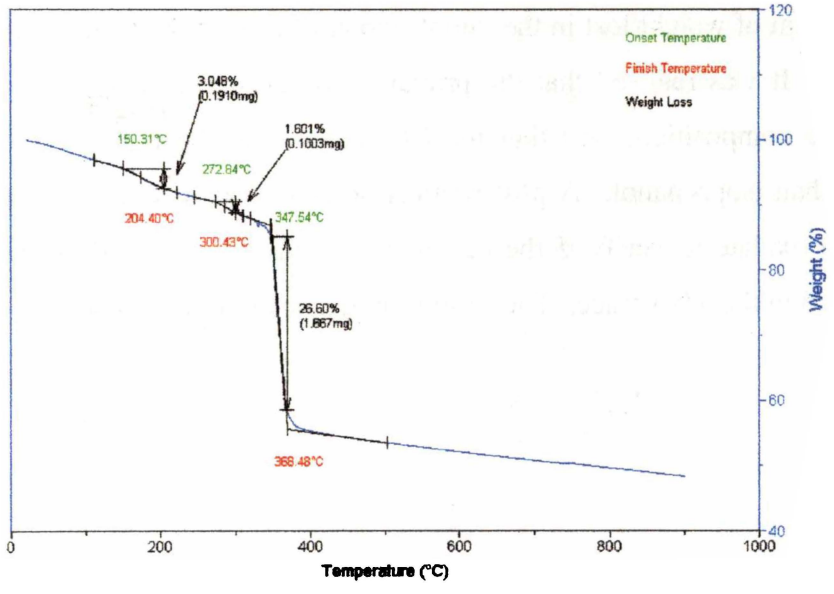

Figure 4.11 TGA Trace of CGS05 Oxalate.

The small steps present in the temperature range of 100 - 350 °C are possibly due to the formation of stable hydrated oxalate species. The phenomenon was observed by Mobius[10] for some of the single metal oxalate species.

Cerium and praseodymium oxalates did not show this but gadolinium and samarium oxalate were among those that did. It would appear, that while a mixed metal oxalate has been formed, the presence of the other metal species has imparted some of their character on the mixed oxalate.

For a single step complete decomposition from the anhydrous mixed metal oxalate to the mixed metal oxide one would expect a weight change in the order of 35%. From Figure 4.9 - Figure 4.11 it can be seen that the weight loss associated with the oxalate decomposition step is approximately 24-25%. This is lower than the expected weight loss, however these weight loss values are determined from the steepest part of the graph and neglect the lead in and tail off sections of this particular step. In addition there is continued gradual weight loss subsequent to the oxalate decomposition step; this gradual loss may be due to the decomposition of trace amounts of carbonate formed during the oxalate decomposition[8].

During preliminary thermal analysis investigations it was noted that the CG oxalate showed a significant difference to the other oxalates tested, primarily in the amount of weight lost in the initial step attributed to the loss of water from the sample. It was realised that the primary difference between the samples, other than the composition, was that the CG oxalate had been washed with ethanol rather than isopropanol. A post production isopropanol wash was performed on the CG oxalate to verify if the difference in solvents had caused the difference observed in the TGA trace. The results are displayed in Figure 4.12.

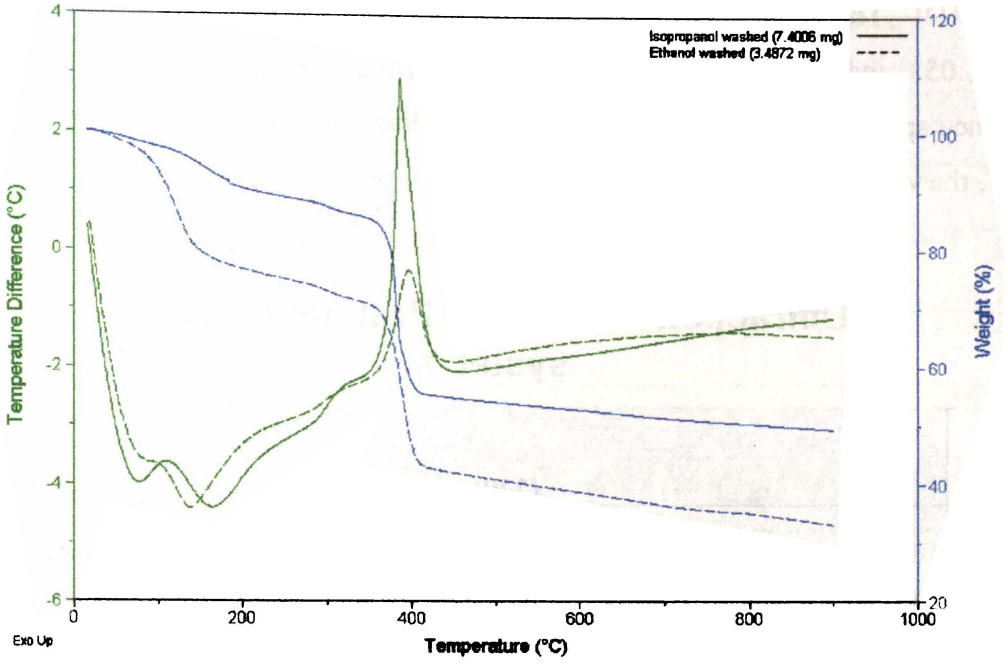

Figure 4.12 DTA/TGA Traces of CG Oxalate Washed with Different Solvents.

It can be observed that isopropanol washing reduced the weight loss attributed to the loss of water, and intensified the exothermic peak attributed to oxalate decomposition. The purpose of the solvent washing step is to de-water the powder. It appears from these results that isopropanol is more effective, removing a higher proportion of water from the oxalate material than ethanol.

4.2.3 Powder X-ray Diffraction (XRD)

XRD was undertaken to confirm that the samples produced were single phase and possessed the desired crystal structure, namely cubic fluorite. XRD patterns obtained for the samples prepared by co-precipitation, Figure 4.13 and Figure 4.14, confirmed that they were indeed single phase and conformed to the pattern expected of doped ceria compounds - maintaining the base ceria structure as set out in JCPDS file 43-1002 (Appendix 3). Comparison of the spectra obtained with the file for pure ceria, reveals that the peak positions are shifted to slightly higher (on average 0.01 Å) d-spacings.

This variation is attributable to the dissolution of dopant species with larger ionic radii than Ce^{4+}; the presence of these larger species causes expansion of the lattice[13]. The ionic radius of Ce^{4+} is 0.97 Å, while the radii of Gd^{3+} and Sm^{3+} are 1.053 and 1.079 Å respectively; praseodymia, being present as a mixed valence species will have an effective ionic radius between the radii of Pr^{4+} and Pr^{3+}, the values of which are 0.96 and 1.126 Å respectively.

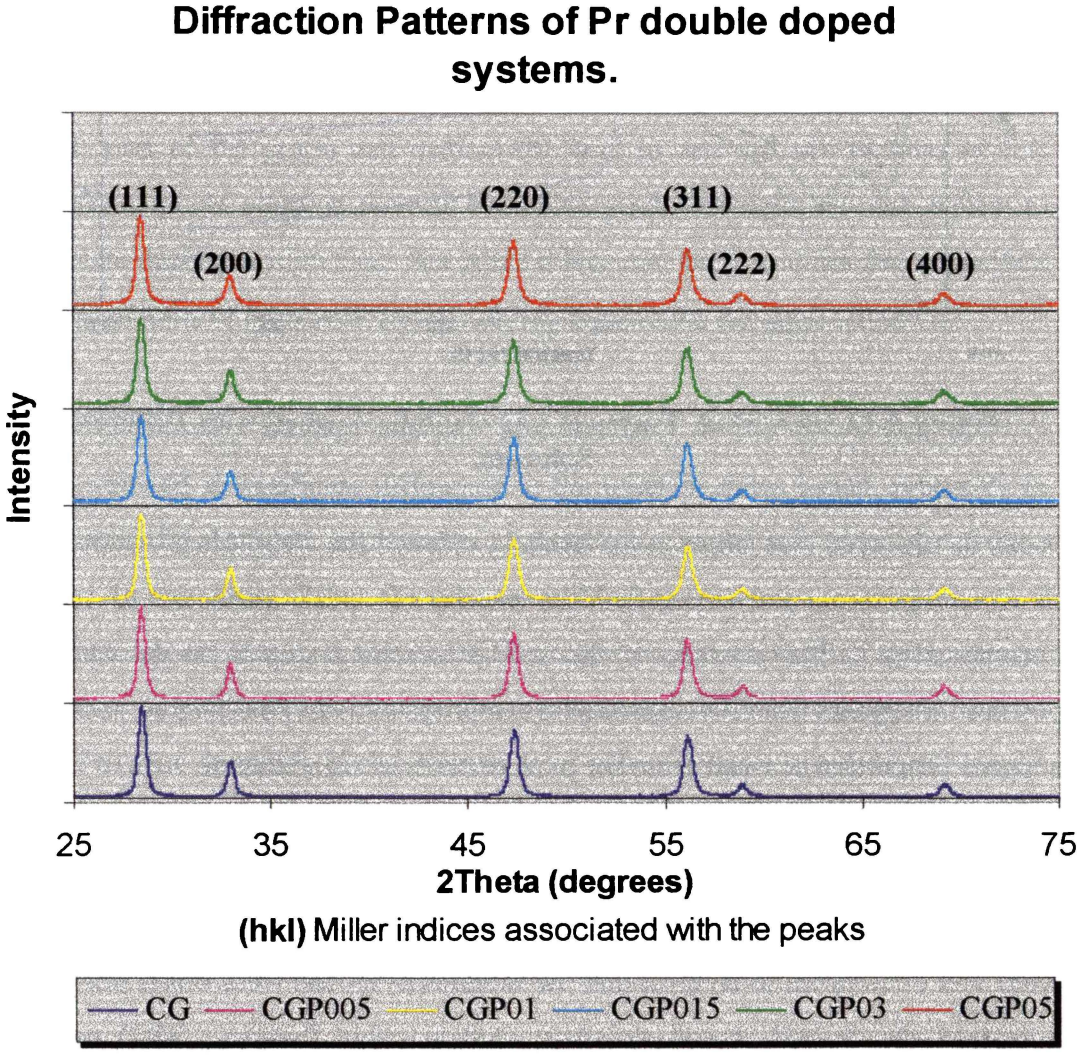

Figure 4.13 XRD Patterns of Praseodymia Double Doped Samples.

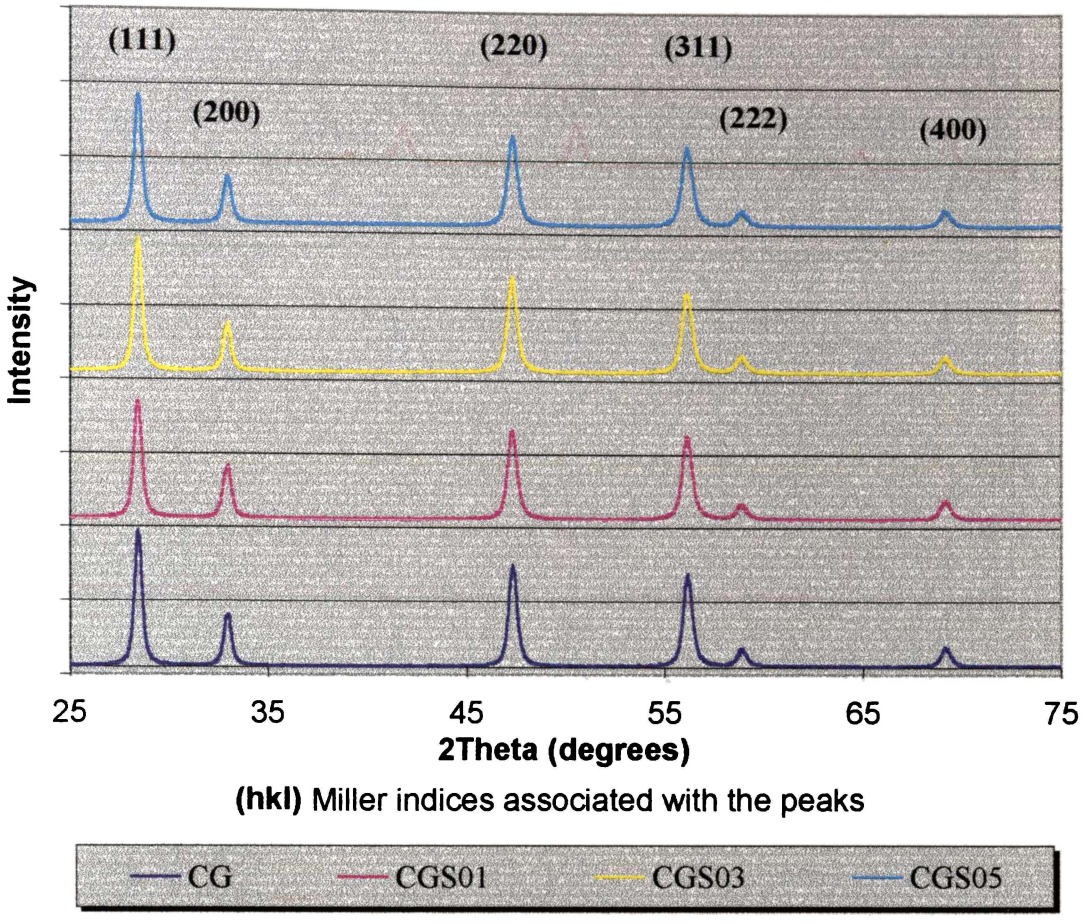

Figure 4.14 XRD Patterns of Samaria Double Doped Samples.

The powders prepared by the Pechini method were also examined by XRD. They also prove to be single phase with the fluorite structure, Figure 4.15. It can be seen that the CG and CGP03 prepared by the Pechini method show more intense, narrower peaks than their co-precipitate counterparts, this would indicate that the co-precipitated powders possess a smaller crystallite size. However with the CGS03 samples this occurrence is reversed. This reversal is consistent with the observation that the Pechini precursor for CGS03 was different from the CG and CGP03 precursors.

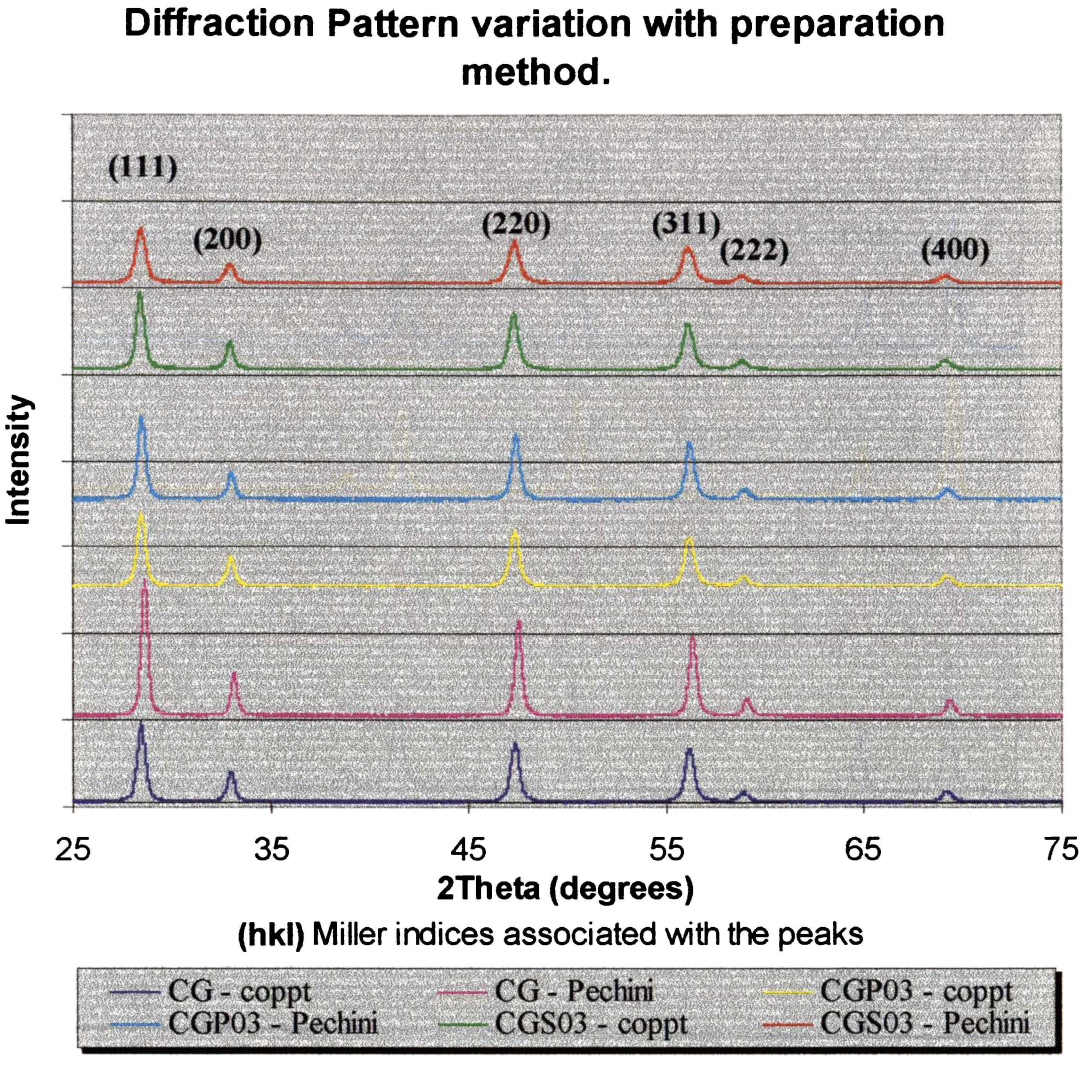

Figure 4.15 XRD Patterns of Samples Prepared by Different Methods.

High Temperature Phase Stability

High temperature XRD of the samples was performed to ascertain if the powders prepared showed evolution of secondary phases when at elevated temperatures. Literature review revealed no mention of high temperature phase evolution in the CG material; however as the double doped materials are not commonly studied no information could be found as to their high temperature phase stabilities. At the concentrations involved both praseodymia and samaria form a solid solution with ceria[3], however it was unknown if there would be additional phases formed by having three components present. Evolution of second phases at high temperatures could be detrimental to both the conductivity of the sample and its mechanical integrity[14].

Figure 4.16, Figure 4.17 and Figure 4.18 show there was no evolution of secondary phases up to the maximum temperature of testing, 1273 K, which is higher than the operating temperature envisaged for fuel cells incorporating these materials. Samples of all powders were tested, though only the patterns for the maximum Gd, Pr and Sm content are reproduced here as they are the compositions one would expect to most likely exhibit second phases. None of the compositions tested showed the evolution of secondary phases.

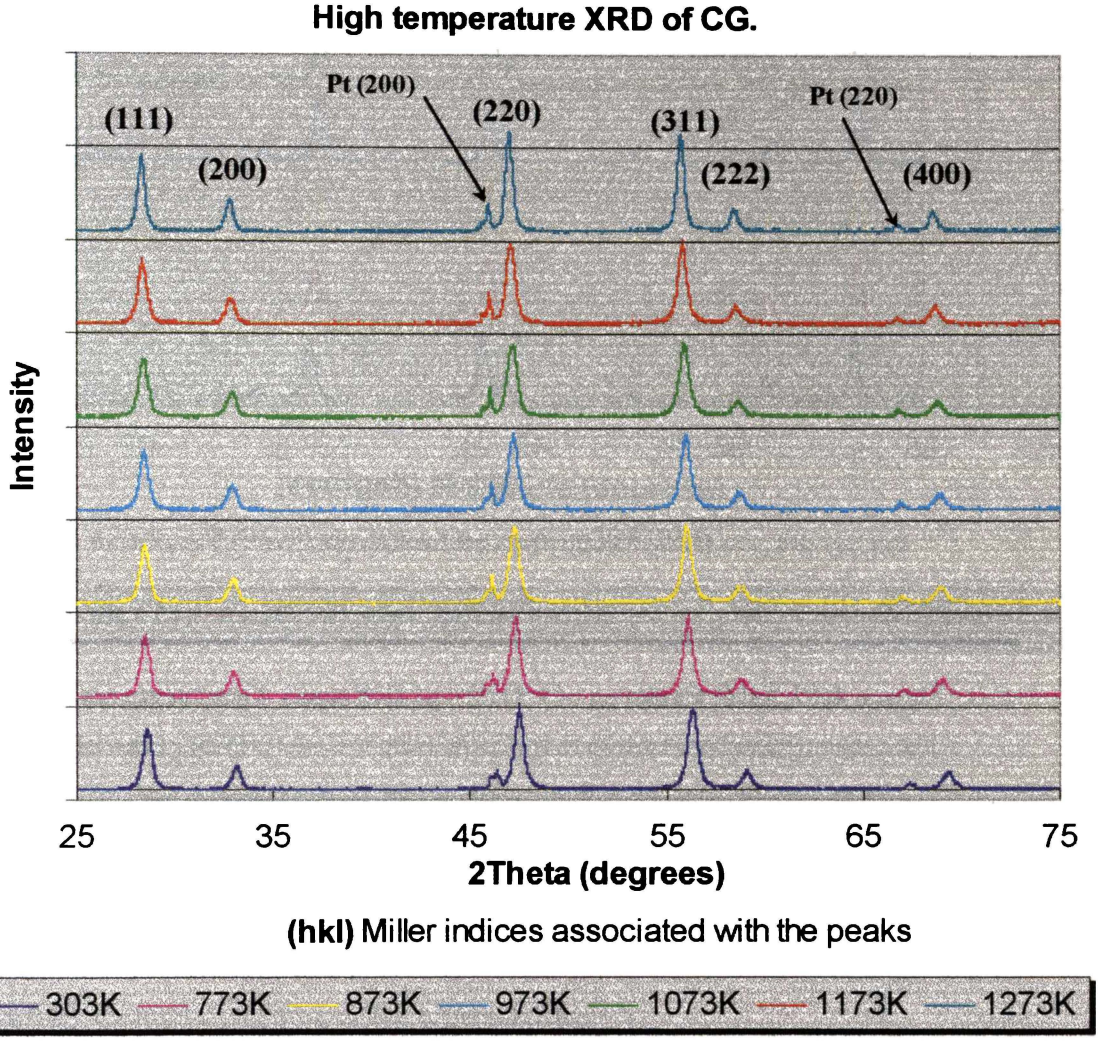

Figure 4.16 XRD Patterns of CG at Different Temperatures.

(hkl) values prefixed by Pt are for the peaks from the platinum reference material.

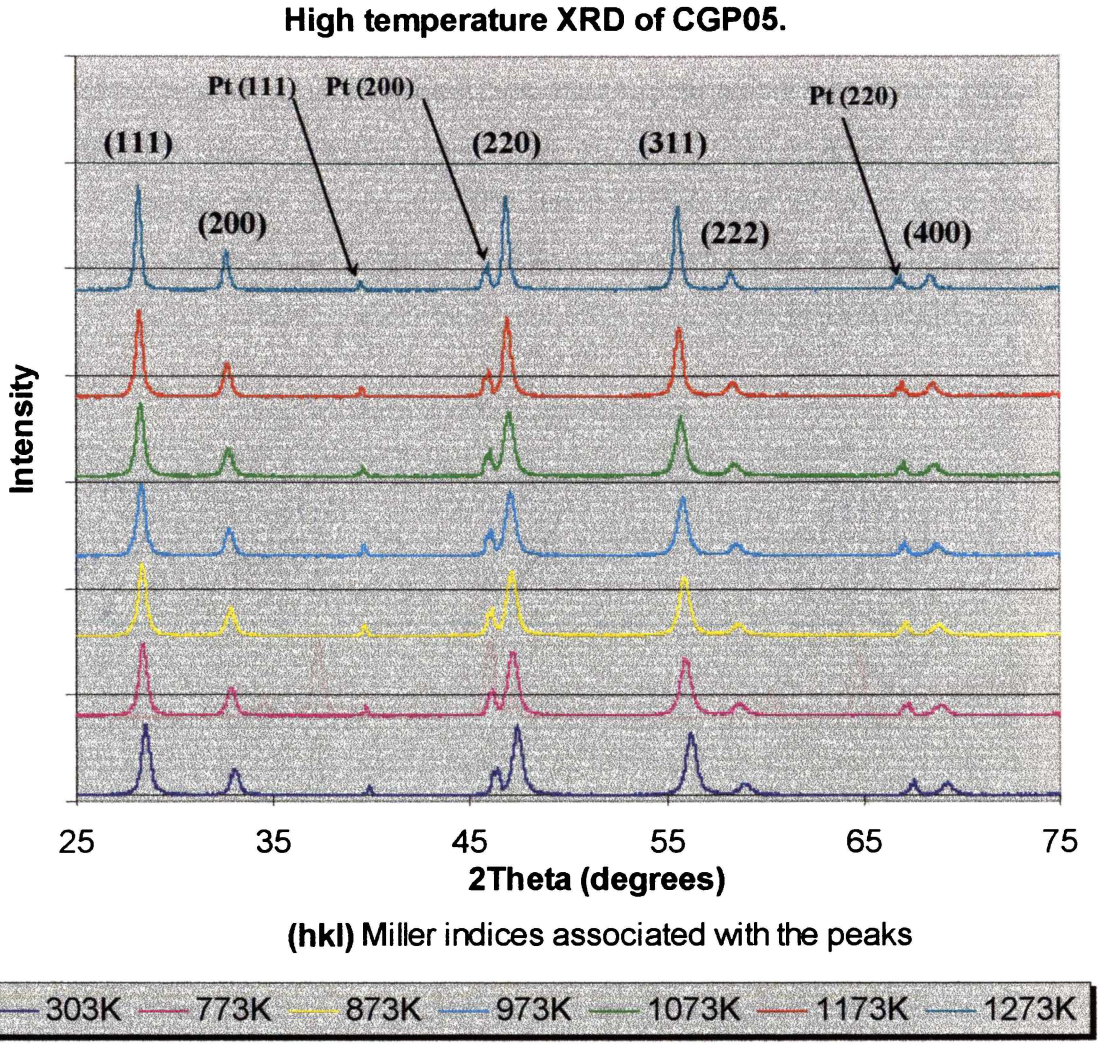

Figure 4.17 XRD Patterns of CGP05 at Different Temperatures.

(hkl) values prefixed by Pt are for the peaks from the platinum reference material.

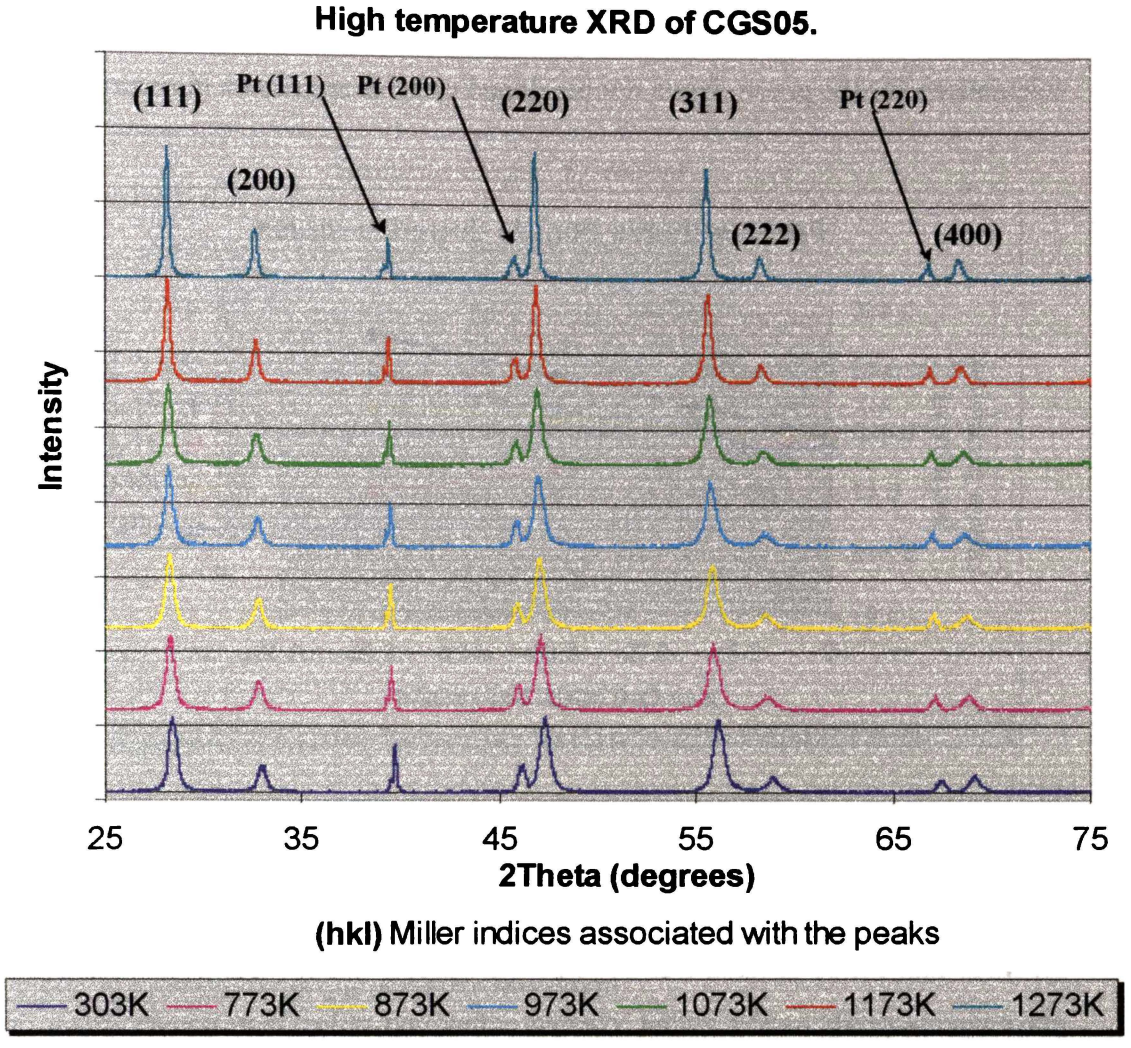

Figure 4.18 XRD Patterns of CGS05 at Different Temperatures.

(hkl) values prefixed by Pt are for the peaks from the platinum reference material.

It can be seen in Figure 4.16, Figure 4.17 and Figure 4.18 that as the temperature is increased the peak positions move to lower angles, this is as expected and is caused by thermal expansion of the crystal lattice[15].

Lattice Parameters

The experimental lattice parameter, a, was determined for each of the dopant regimes using the peak positions determined from the XRD patterns of the samples.

The theoretical lattice parameters for each composition were determined using Equation 2.10 in Chapter Two. The results of these measurements and calculations for the praseodymia double doped systems are shown in Figure 4.19.

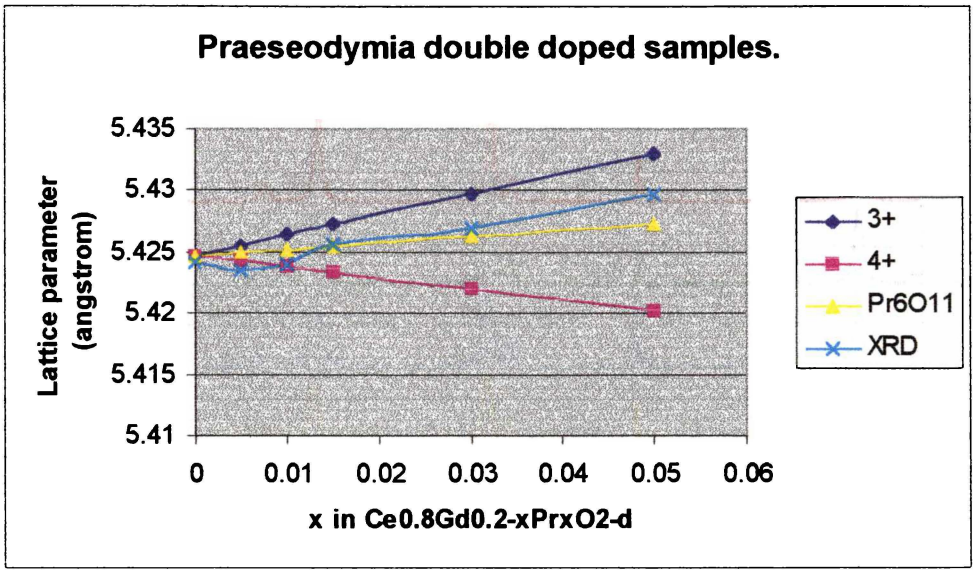

Figure 4.19 Lattice Parameter Variation with Dopant Level.

The three theoretical lattice parameter lines are based on calculations where it was assumed that the Pr present was Pr^{3+}, Pr^{4+} or mixed valence (Pr_6O_{11}). Generally praseodymia exists as the mixed valence compound rather than wholly Pr_2O_3 or PrO_2[16]. It can be seen that from Figure 4.19 that the lattice parameters determined from the XRD data fall within the range of lattice parameters possible, though do not fully match any of the theoretical values.

The lattice parameters for the samaria double doped samples are shown in Figure 4.20.

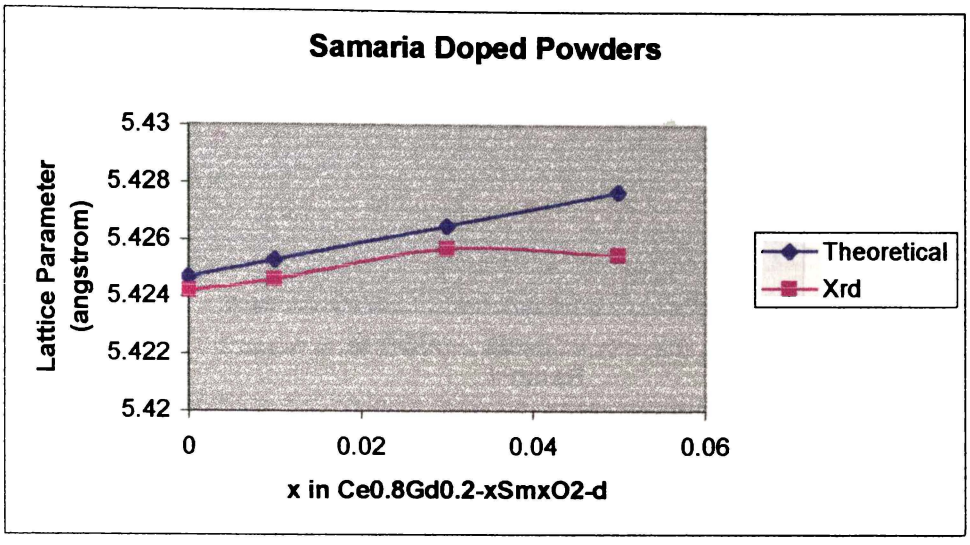

Figure 4.20 Lattice Parameter Variation with Dopant Level.

Unlike praseodymia, there is no ambiguity as to the valence of Sm and hence only one set of theoretical lattice parameter calculations. It can be seen that the lattice parameters calculated from XRD data are lower than those expected and that the CGS05 sample shows an anomalously low value.

The lattice parameters determined for the samples prepared by the Pechini method are shown in Figure 4.21, with results from the co-precipitated samples and theoretical values included for comparison. It can be seen that the only significant difference in lattice parameters is the Pechini CGP03 sample having a lattice parameter significantly lower than the theoretical or co-precipitated values. Although Pechini CGS03 intermediate looked different to the other Pechini intermediates it does not seem to have affected the lattice parameter.

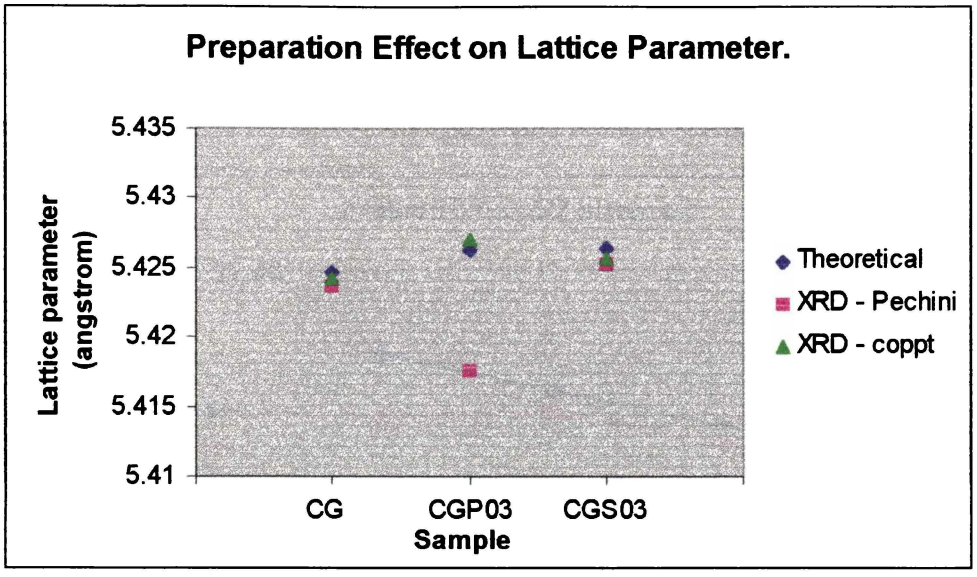

Figure 4.21 Lattice Parameter Variation.

Crystallite Size

The crystallite size of the sample powders was determined from peak broadening of the (400) peak, occurring at approximately 88° 2θ. Computed values of the width at half intensity, compared to a standard ceria sample, were inputted to the Scherrer equation. The effect of dopant concentration is shown in Figure 4.22. It can be seen that as the double dopant level is increased the crystallite size decreases, with the result for CGP01 appearing anomalously low. It has been noted by other authors [17-20] that the addition of different dopant species can affect the crystallite size of a material. Figure 4.22 indicates that the substitution of praseodymia or samaria for a percentage of the gadolinia, in gadolinia doped ceria, decreases the crystallite size of the material. It has been noted[19] that gadolinia doped ceria itself has a smaller crystallite size when compared to pure ceria.

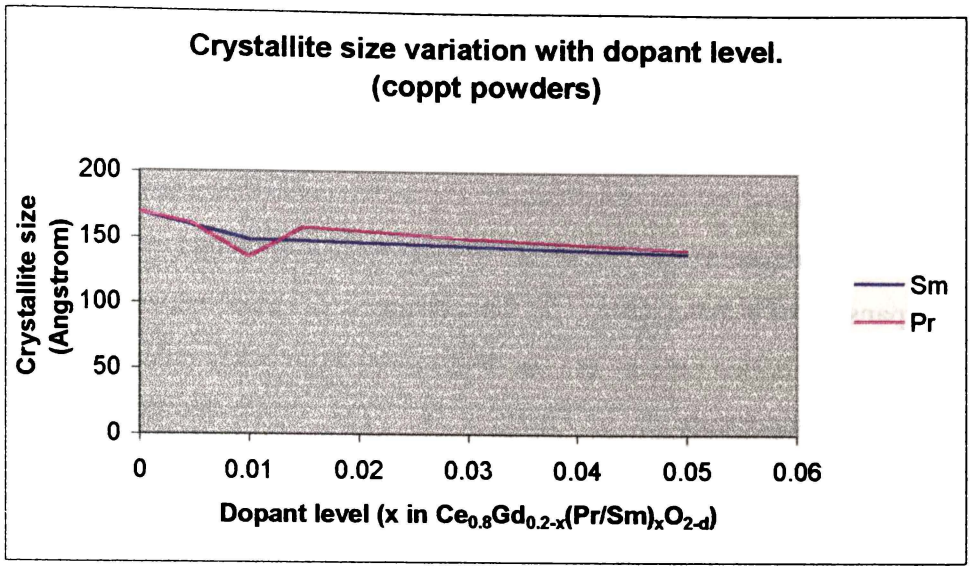

Figure 4.22 Crystallite Size, Effect of Dopant.

The effect the preparation technique has on crystallite size was also evaluated, the results of which are displayed in Figure 4.23. It can be seen that the co-precipitation method produced smaller crystallites except in the case of CGS03, however it should be recalled that the Pechini preparation of CGS03 proceeded differently from that of CG and CGP03.

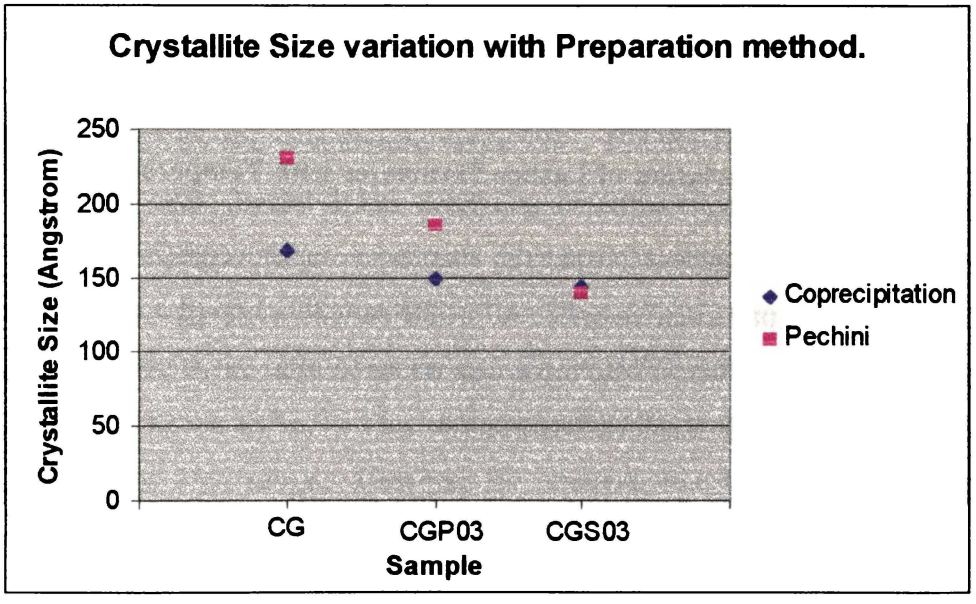

Figure 4.23 Crystallite Size, Effect of Preparation.

Thermal Expansion

Examination of the thermal expansion data reveals that over the temperature range investigated all of the samples show a change in their thermal expansion. The change may be caused by the presence of thermally generated vacancies. It is known that thermally generated vacancies will cause an anomalous increase in the thermal expansion of a material[21, 22]. This change in thermal expansion can be clearly seen when lattice parameters, as determined from XRD calculations, are plotted against temperature as in Figure 4.24. The slopes on the graph are proportional to the average coefficient of thermal expansion for the temperature range associated with those slopes.

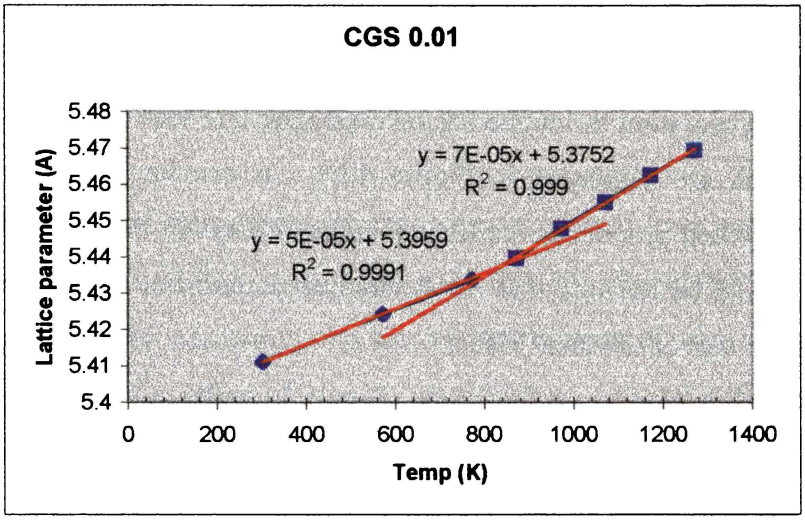

Figure 4.24 Variation of Lattice Parameter with Temperature.

It can be seen from Figure 4.24 that the change in slope occurs in the range of 800-900 K for this particular sample. All of the samples showed a change in the temperature range of 700-900 K; there was no systematic variation of transition temperature with double dopant concentration.

Figure 4.25 shows the calculated average coefficient of thermal expansion, $\bar{\alpha}$, for the praseodymia double doped samples.

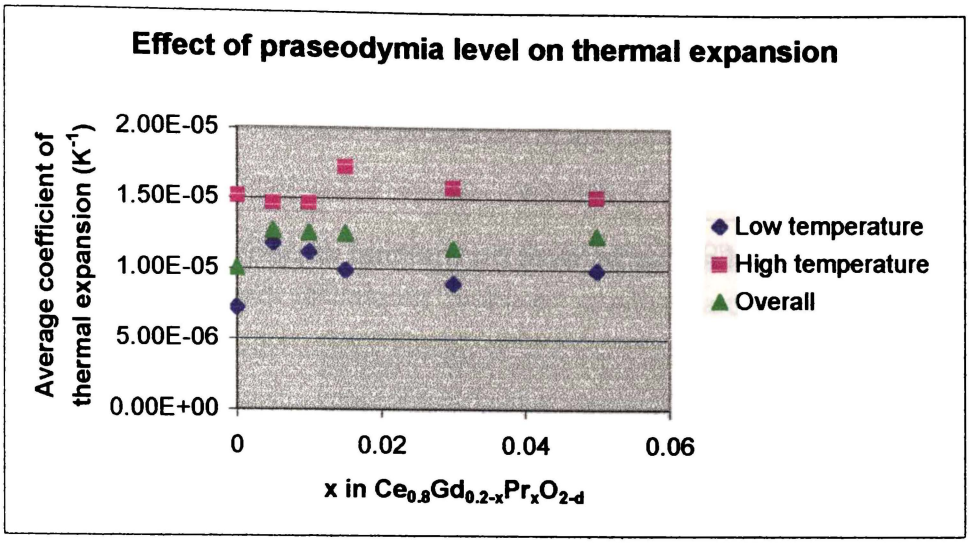

Figure 4.25 Coefficient of Thermal Expansion Variation.

In Figure 4.25 the points labelled low temperature are the $\bar{\alpha}$ values determined for the temperature range prior to the change in slope; high temperature points are the $\bar{\alpha}$ values determined for the temperature range after the change in slope; the overall $\bar{\alpha}$ values are calculated using the whole temperature range. There is no systematic variation with praseodymia concentration other than all the praseodymia containing samples show a higher overall $\bar{\alpha}$ than the base CG material. The overall $\bar{\alpha}$ value for CG of 10.0 x 10^{-6} K^{-1}, determined over the temperature range of 303 - 1273 K, is lower than that found by Mogensen et al. (12.5 x 10^{-6} K^{-1} for the temperature range 323 - 1273K)[23] or Tompsett (11.6 x 10^{-6} K^{-1} at 1273 K). Steele[22] has stated that a thermal expansion difference of up to 10% is tolerable with respect to fuel cell component mismatch. For intermediate temperature fuel cells it is envisaged that a ferritic stainless steel would be used as an interconnect material; these have a thermal expansion coefficient of 12.5 x 10^{-6} K^{-1}. This means that the CG material tested here would fall outside the 10% range. However the praseodymia doped samples, having higher $\bar{\alpha}$ values, in the range of 12.4 - 12.6 x 10^{-6} K^{-1} (with the exception of CGP03), do fall within the 10% difference range. The fact that the materials show two different $\bar{\alpha}$ values over the temperature range tested may cause thermal expansion mismatch problems during thermal cycling.

Figure 4.26 shows the effect samaria concentration has on the thermal expansion coefficient. It can be seen that the addition of samaria causes less of an increase in thermal expansion coefficient than praseodymia addition.

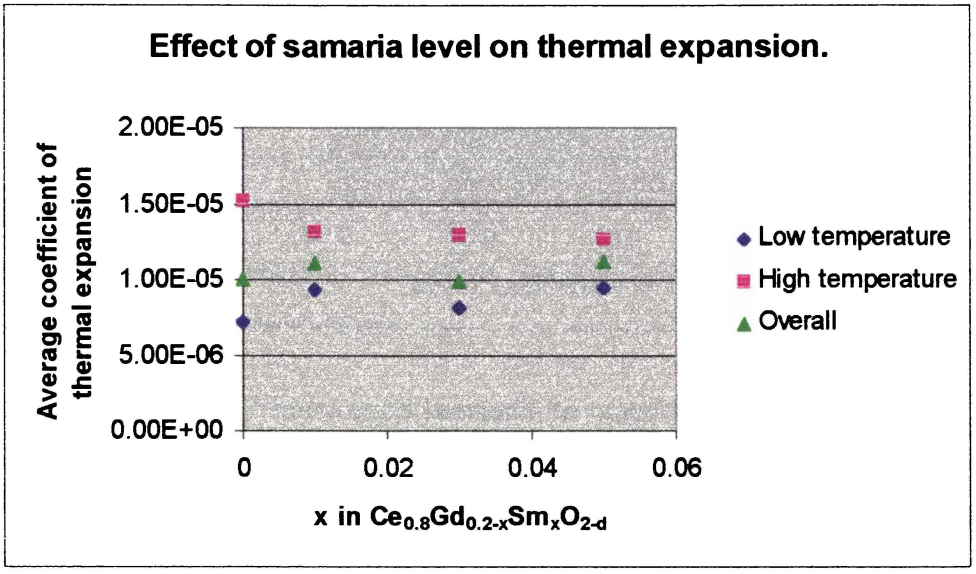

Figure 4.26 Coefficient of Thermal Expansion Variation.

Figure 4.27 shows the variation induced in the $\overline{\alpha}$ values through the different preparation techniques. The $\overline{\alpha}$ values used were determined over the temperature range of 303 - 1273 K. It can be seen that there is very little difference in thermal expansion between the materials produced by the different methods.

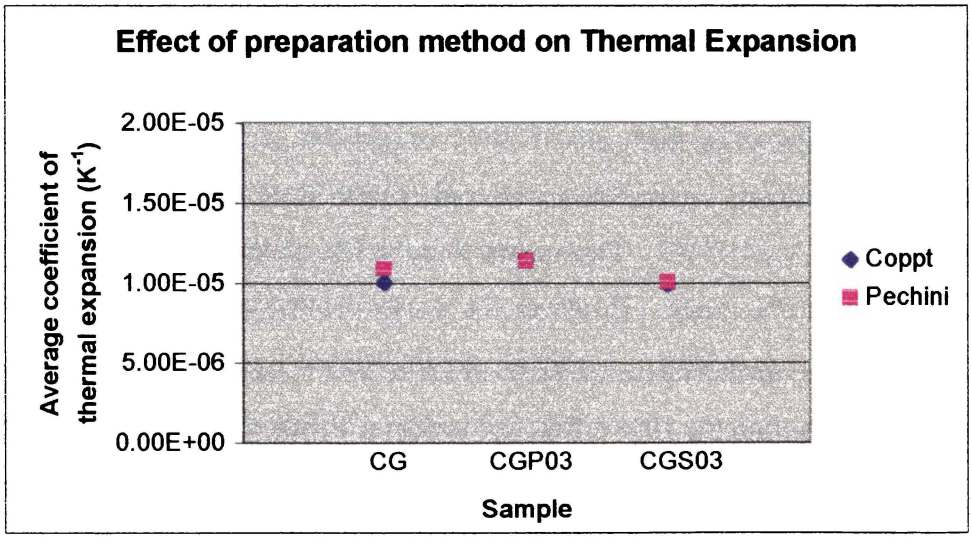

Figure 4.27Coefficient of Thermal Expansion Variation.

4.2.4 Particle Size

Particle size measurements were performed using a laser diffraction technique. The purpose of the measurements was to determine if there was any evidence of agglomeration, as indicated by a multimodal size distribution, and to detect if one of the powder preparation techniques produced smaller particles than the other. Agglomeration of a powder can be detrimental to the sintering process, preventing the attainment of closed porosity. It is also known that a smaller particle size enhances the sintering properties of a powder[24].

All of the powders showed monomodal size distributions in the sub-micron range, CG-coppt as an example in Figure 4.28, indicating that no hard agglomerates were present within the samples. As the samples were subjected to ultrasonic treatment during the measurement procedure, the presence of soft agglomerates in the original powder cannot be ruled out, however these have little impact on sintering as they are broken down during compaction. The ultrasonic treatment would be insufficient to break down any hard agglomerates.

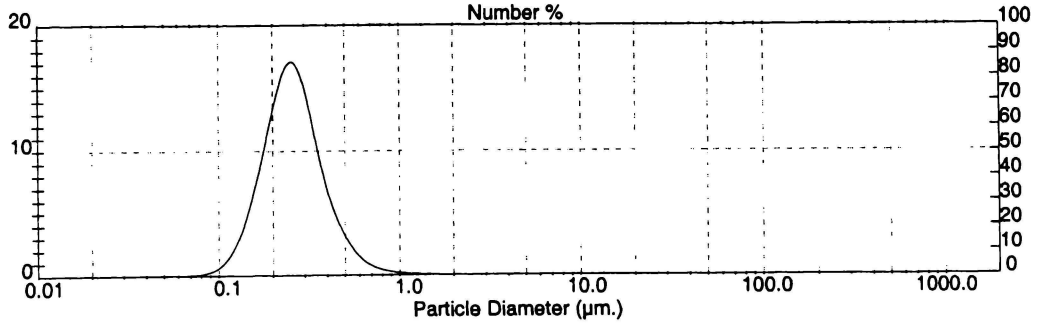

Figure 4.28 Particle Size Distribution of CG powder (coppt).

Particle sizes of the powders produced are listed in Table 4.3. It is noted that the addition of praseodymia to the coppt samples caused a slight decrease in the particle size with respect to the particle size of the CG powder. There does not seem to be a systematic variation due to the concentration of praseodymia. Samaria causes little or no change in the particle size in comparison to CG. This dopant effect is not shown by the powders prepared by the Pechini method.

All three of the Pechini powder size distributions are very similar and comparable to their co-precipitated analogs, with the exception of Pechini CG - having smaller particles than coppt CG.

Table 4.3 Particle Size Results for all Powders.

Sample	Particle size (μm)		
	10^{th} percentile	Median	90^{th} percentile
CG - coppt	0.16	0.25	0.42
CGP005 - coppt	0.13	0.22	0.39
CGP01 - coppt	0.12	0.22	0.38
CGP015 - coppt	0.12	0.22	0.38
CGP03 - coppt	0.14	0.23	0.40
CGP05 - coppt	0.13	0.23	0.39
CGS01 - coppt	0.16	0.25	0.41
CGS03 - coppt	0.16	0.25	0.42
CGS05 - coppt	0.15	0.24	0.41
CG - Pechini	0.13	0.22	0.38
CGP03 - Pechini	0.13	0.22	0.37
CGS03 - Pechini	0.14	0.22	0.36

Effect of Milling

The effect of both wet and dry milling of the powders on particle size was investigated, with results shown in Table 4.4. Dry milling of the co-precipitated powder caused a slight increase in the value of the 10^{th} percentile and median values while leaving the 90^{th} percentile unaffected. This would indicate that dry milling caused the consolidation of the smaller particles present in the powder. In contrast dry milling of the Pechini powder caused a slight increase in all three values. This would suggest that this milling regime acted to consolidate the powder.

As will be seen later, in the SEM investigation section, the laser diffraction size results for the dry milled Pechini CG powder belie the true extent of the consolidation - presumably due to the ultrasound step of the measurement breaking down the agglomerates.

Wet milling of the co-precipitated powder caused a slight decrease in the 10^{th} percentile and median values, while the 90^{th} percentile value remained the same.

Table 4.4 Effect of Milling on Particle Size.

Sample	Particle size (μm)		
	10^{th} percentile	Median	90^{th} percentile
CG - coppt	0.16	0.25	0.42
CG - coppt, dry milled	0.18	0.27	0.42
CG - coppt, wet milled	0.14	0.24	0.42
CG - Pechini	0.13	0.22	0.38
CG- Pechini, dry milled	0.16	0.25	0.40
CG - Pechini, wet milled	0.13	0.22	0.41

4.2.5 Surface Area

The surface area of the samples, determined using a three-point BET method, revealed no systematic variations with varying dopant level. The different double dopants had no apparent effect on surface area. Neither of the preparation techniques employed produced powders that were consistently of higher surface area than the alternate technique. The average surface area of the powders produced was 20 m^2/g, with a range from 15 m^2/g - 27 m^2/g.

Effect of milling

Surface area measurements were also made of the powders that underwent a milling regime. Milling of the CG-coppt powder caused a slight increase in surface area, approximately 2 m^2/g greater than the starting powder - an increase of 8%. Both wet milling and dry milling produced the same magnitude of effect.

Dry milling of the CG-Pechini powder drastically reduced the surface area of the powder to 5.5 m^2/g, a decrease of 70% from the original surface area. Based on the improved flowability of the dry milled powder, it was expected that the powder would consist of larger particles and hence have a lower surface area. Wet milling of the CG-Pechini powder had no significant effect on the surface area.

4.2.6 SEM of Powders

SEM imaging was performed to investigate the particle size and particle morphology of the oxide powders prepared. Particle size and morphology have an impact on compaction and sintering properties as well as affecting the grain size of the sintered item. SEM imaging reveals that the two different preparation techniques generate particles with dissimilar morphologies, as shown in Figure 4.29.

The powder prepared by co-precipitation has elongated angular particles that range from sub-micron up to approximately 3 micron in size (Figure 4.29A); this size range encompasses the range indicated by particle size measurements. Other researchers[25] have noted that this elongated, angular particle morphology is an artefact of the oxalate precursor, as this is the form that the oxalate crystals take. Higher magnification investigation of these particles (Figure 4.29B) shows that they have a surface texture suggesting that each particle is an aggregate of smaller particles. The main features of the surface texture are in the order of 60-130 nm, too large to be primary crystallites.

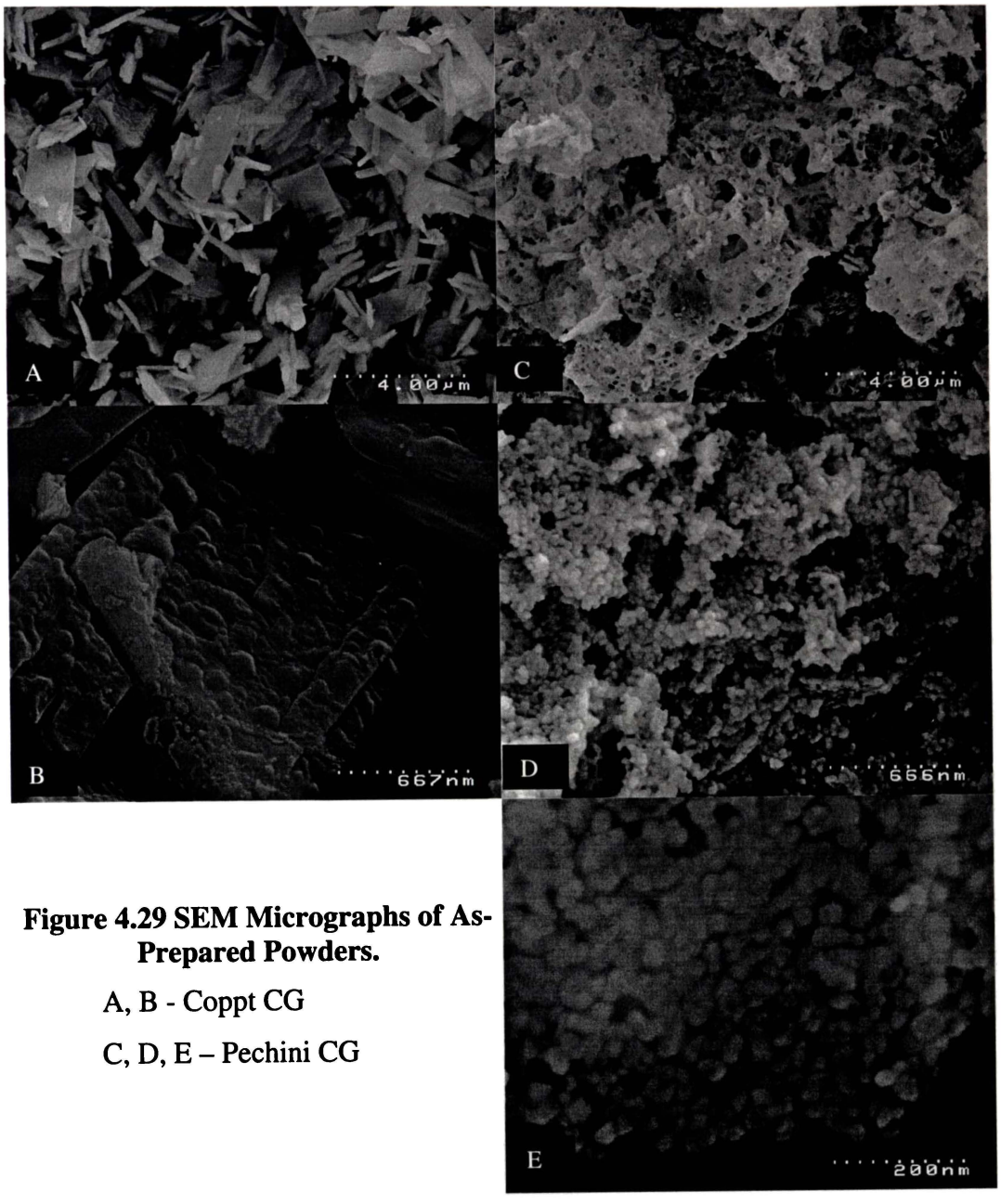

Figure 4.29 SEM Micrographs of As-Prepared Powders.

A, B - Coppt CG

C, D, E – Pechini CG

From Figure 4.30 it can be seen that on the edge of the particle there are significantly smaller items approximately 10-20 nm in size. This corresponds with the crystallite size determined from XRD peak broadening.

The Pechini powder consists of large porous fragments (Figure 4.29C). Closer inspection of these fragments (Figure 4.29D and E) reveals that they are constructed of small particles with a size 20-40 nm. This size range encompasses the crystallite size determined from peak broadening of the XRD pattern. It therefore appears that these small particles visible with SEM are in fact the primary crystallites of the powder.

There did not seem to be any appreciable difference between powders with differing dopant concentrations or species with respect to particle size or morphology. This was true for powders prepared by either of the methods.

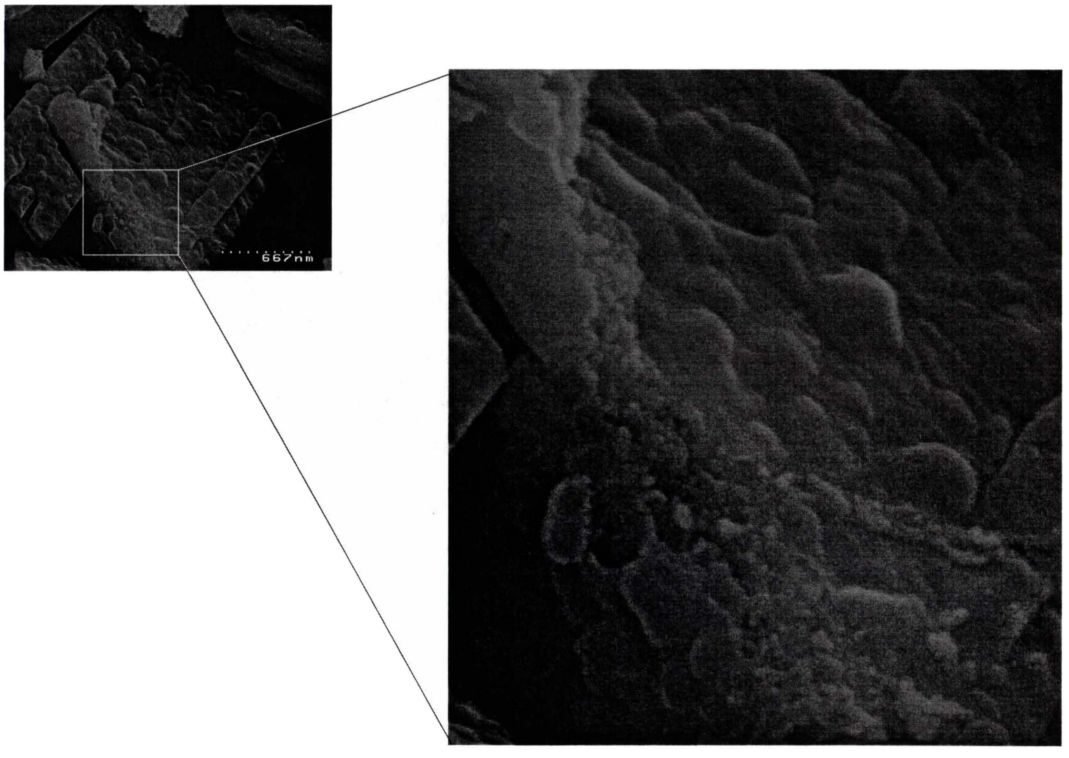

Figure 4.30 Zoomed Section of Figure 4.29B.

Effect of Milling

The base material, CG, prepared by the different methods was wet milled and also dry milled to evaluate whether this technique could be utilised to reduce the particle size of the powders. Reducing the particle size is desirable as a small particle size enhances the sintering process allowing items to obtain high density without the need for long-time/high-temperature sintering regimes.

SEM images of the milled co-precipitated powder are shown in Figure 4.31A-F. It is observed that the dry milled powder no longer contains the large angular particles present in the initial powder, as was seen in Figure 4.29A. The angular particles have been replaced by what appear to be spherical/oblong agglomerates of smaller particles, Figure 4.31A and B. These agglomerates range in size from sub micron to approximately 3 micron in size - comparable to the particle sizes observed by SEM of the starting powder. Higher magnification, Figure 4.31C, shows the small particles making up the agglomerates are approximately 20 nm in size - the same order of size as that determined for the primary crystallites. While the milling does seem to have broken down the particles, comparison of these results with the particle size determined by laser diffraction would lead one to conclude that while the angular nature of the particles has changed there has been only a slight decrease in particle size.

Wet milling of the powder also seems to have broken up the angular particles present in the original powder. Unlike the dry milled material though there do not appear to be obvious spherical or oblong agglomerates, Figure 4.31D. Further examination at higher magnifications (Figure 4.31E and F) shows that there are clusters of small particles present and that these small particles are of a size similar to that of the primary crystallite result obtained through XRD.

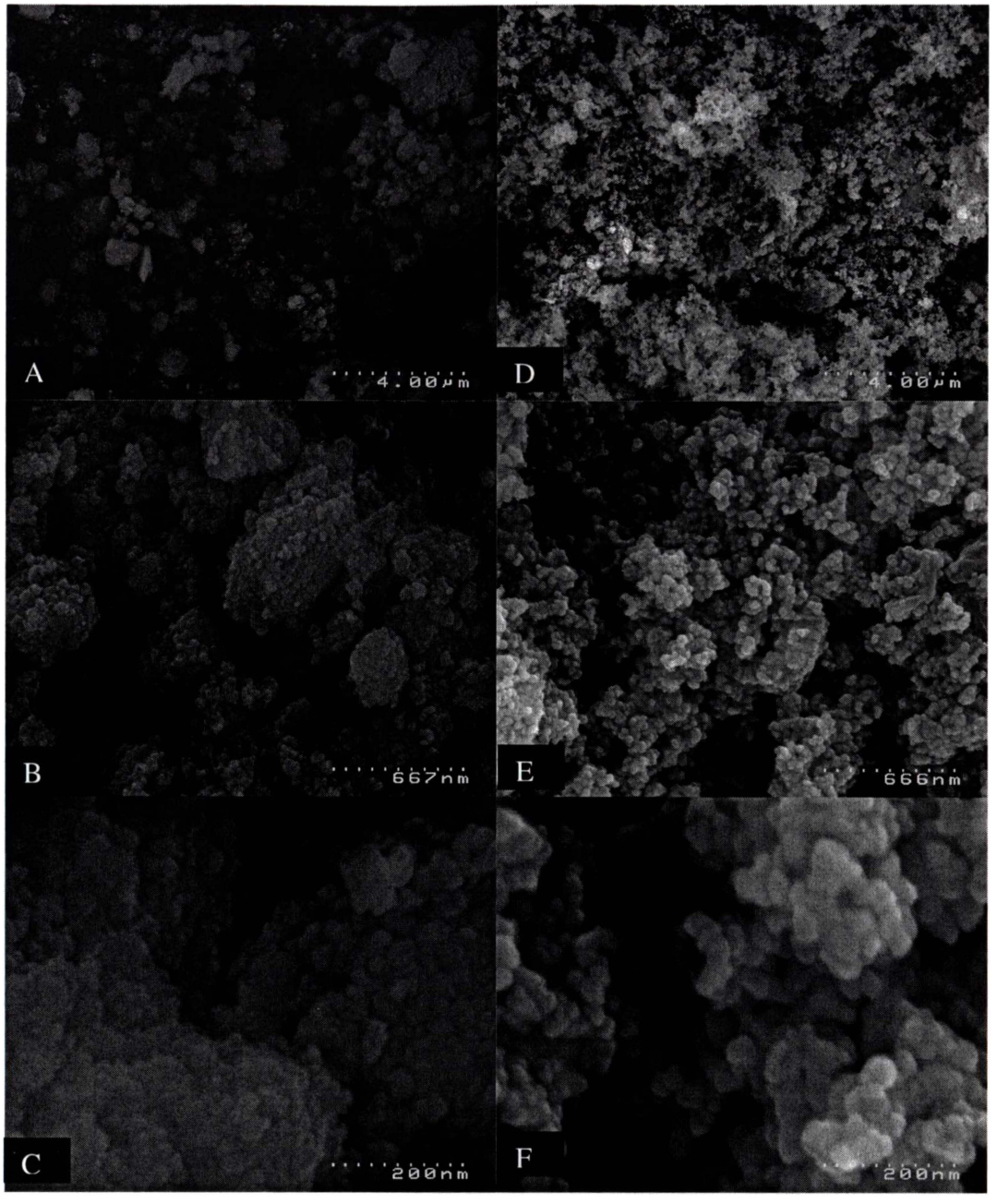

Figure 4.31 SEM Micrographs of Milled Coppt CG.

A, B, C – dry milled D, E, F – wet milled

SEM images of the milled Pechini powder are displayed in Figure 4.32A-E. If one first considers the dry milled powder, it is seen that the large porous structures present in the initial powder (as seen in Figure 4.29C) are no longer present. However there are significantly larger, approximately 30-60 micron in size, particles present.

These are presumably formed from the breakdown of the porous structures observed in the initial powder and subsequent consolidation of the resulting fragments. The formation of these larger particles is corroborated by the surface area measurements, where a large decrease in surface area was observed for the dry milled Pechini powder, refer to section 4.2.5. In Figure 4.32B and C it is observed that smaller particles can be detected and that these particles are of a size similar to that determined for the crystallite size from XRD.

Wet milling of the Pechini powder has broken up the large porous structures of the initial powder and the large consolidated particles of the dry milled powder are not present (Figure 4.32D). As with the dry milled powder, particles of a size range close to that of the primary crystallites are observed (Figure 4.32E).

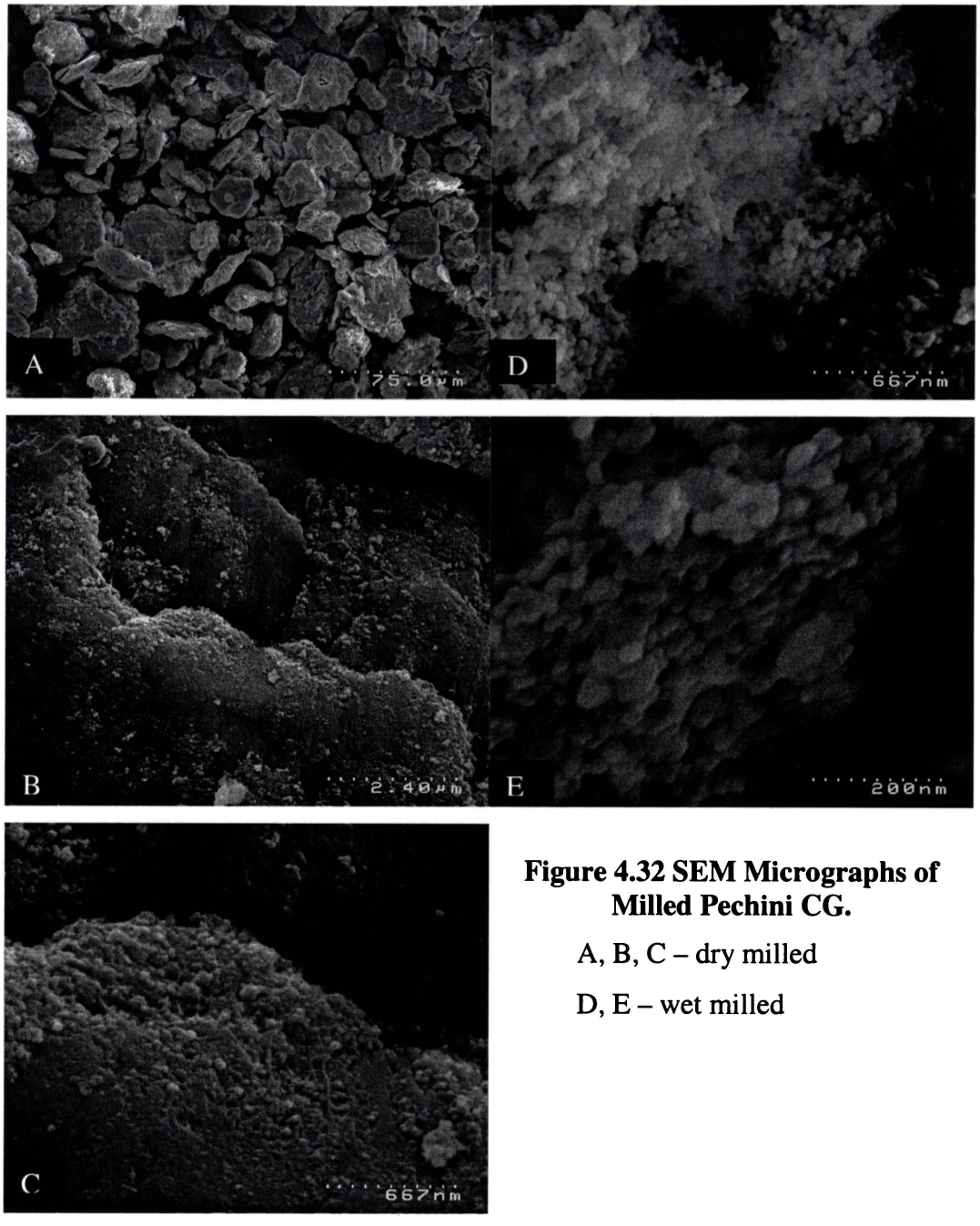

Figure 4.32 SEM Micrographs of Milled Pechini CG.

A, B, C – dry milled

D, E – wet milled

4.3 Pellet Characterisation

The pellet characterisation section contains observations of interest noted during the fabrication of the pellets and results of the various methods used to characterise the pellets. The methods include Raman spectroscopy, density measurements, x-ray microscopy, ion beam analysis and SEM investigation.

4.3.1 Experimental Observations

During the fabrication of the pellets there were two main difficulties encountered; these are discussed below.

Pellet Compaction Difficulties

The powders prepared by the co-precipitation method were able to be fabricated into green pellets without the addition of a binder or lubricant. These initial green pellets were rather fragile and easily damaged. Subsequent pellets prepared from the co-precipitated powders contained a binder substance, this greatly improved the strength of the green pellets allowing for ease of handling.

The powders prepared from the Pechini method adhered strongly to the die, causing the green pellet to be severely damaged when removal from the die was attempted. Efforts to minimise this problem by lubricating the die surfaces with paraffin wax were largely unsuccessful. Addition of a binder to the Pechini powder greatly reduced the adherence to the die surfaces, allowing for successful pellet production.

The substance used as a binder was oleic acid, at a loading of 3 weight%. This substance acted not only as a binder but also as a lubricant. A binder is primarily added to provide green strength, while a lubricant is used to decrease die-wall and particle-particle friction and facilitate mould release[26].

Sintering of Pellets Prepared from Pechini Powders

It was discovered that pellets produced the Pechini method powders were prone to cracking and delamination during the sintering process. This meant the Pechini powder pellets had a very high rejection rate. An example of the problems encountered are shown in Figure 4.33.

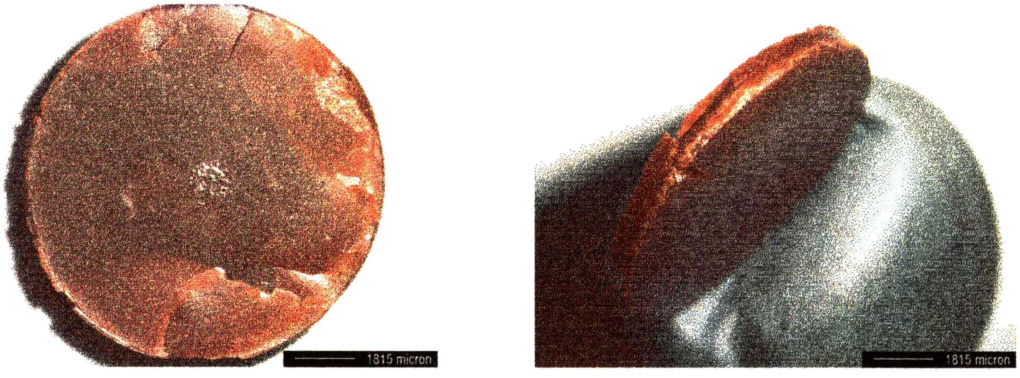

Figure 4.33 Photographs of Delamination and Cracking Problems.

4.3.2 Raman Spectroscopy

Raman spectroscopy was performed on sintered pellets. This method of spectroscopy was used as a secondary method of determining phase composition and structure.

The results obtained for the praseodymia double doped samples are shown in Figure 4.34.

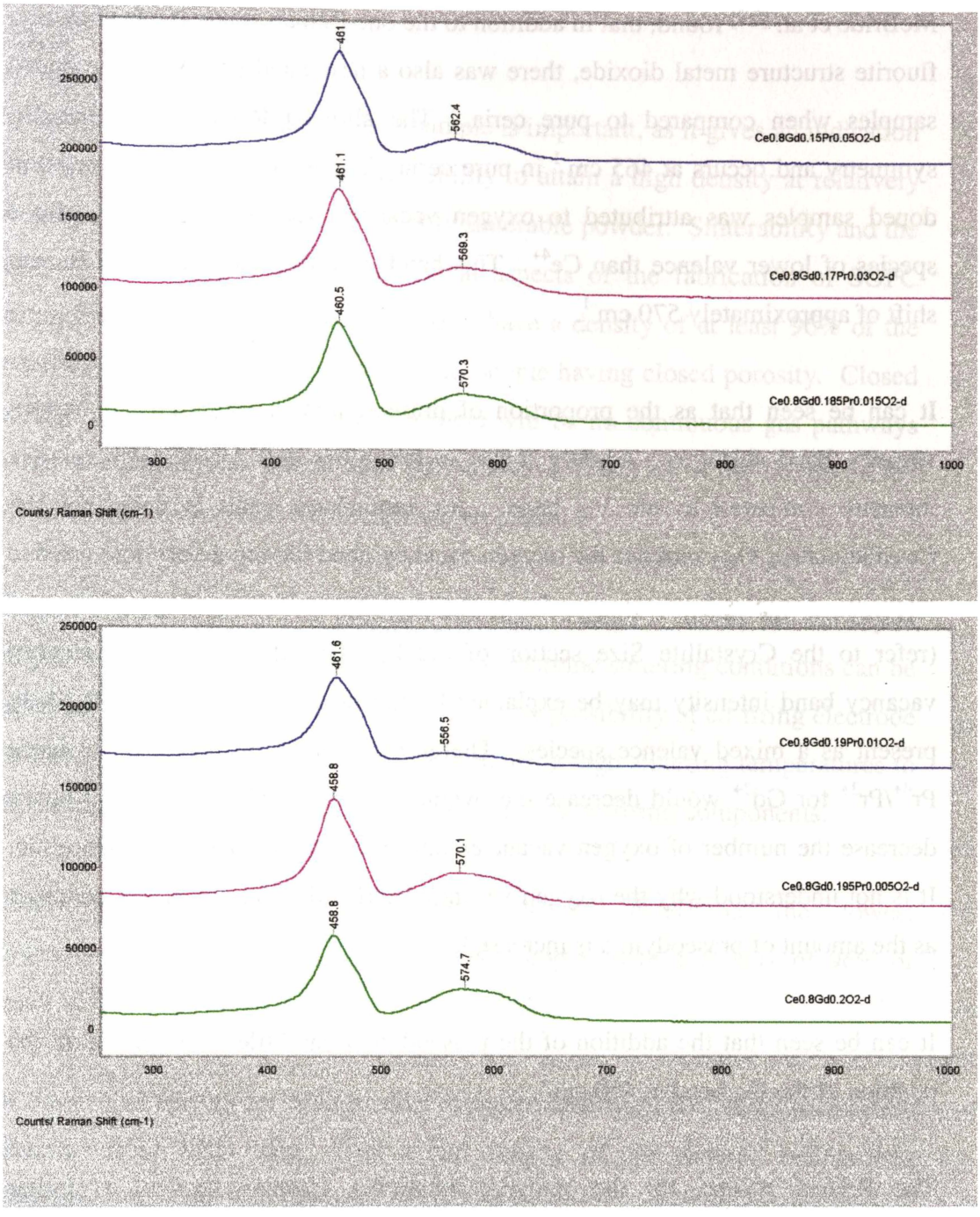

Figure 4.34 Raman Spectra for Pr Double Doped Samples.

It is noted that all six of the spectra show the presence of two bands, one at approximately 460 cm^{-1}, and a broader, less intense band at approximately 570 cm^{-1}. This is consistent with the results obtained by McBride et al.[27] for ceria doped with a single rare earth species.

McBride et al. [27] found, that in addition to the one Raman active mode allowed a fluorite structure metal dioxide, there was also a new band present in the doped samples when compared to pure ceria. The allowed Raman mode has F_{2g} symmetry and occurs at 465 cm^{-1} in pure ceria. The additional band detected in doped samples was attributed to oxygen vacancies formed by doping with a species of lower valence than Ce^{4+}. This band was found to occur at a Raman shift of approximately 570 cm^{-1}.

It can be seen that as the proportion of praseodymia is increased the oxygen vacancy band shifts to a slightly lower wavenumber and decreases in relative intensity compared to the F_{2g} band. An anomalous result is noted for the $Ce_{0.8}Gd_{0.19}Pr_{0.01}O_{2-d}$ sample; the oxygen vacancy band having a very low relative intensity. Samples from this powder have shown anomalous results in other areas (refer to the Crystallite Size section of 4.2.3). This decrease in the oxygen vacancy band intensity may be explained by the fact that praseodymia is likely present as a mixed valence species. Therefore, substituting the mixed valence Pr^{4+}/Pr^{3+} for Gd^{3+} would decrease the overall amount of M^{3+} present and hence decrease the number of oxygen vacancies introduced from charge compensation. It is not understood why the oxygen vacancy band shifts to a lower wavenumber as the amount of praseodymia is increased.

It can be seen that the addition of the praseodymia has little or no effect on the position of the F_{2g} band at 460 cm^{-1}.

The Raman spectra for the samaria containing samples showed a similar systematic variation in the relative intensity of the oxygen vacancy band as the praseodymia containing samples; however the peak position did not show the systematic variation.

4.3.3 Densities

The determination of the density of a sample is important, as it gives an indication of the sinterability of a powder. The ability to attain a high density at relatively low temperatures would indicate a highly sinterable powder. Sinterability and the ability to become fully dense are critical aspects of the fabrication of SOFC electrolytes. The electrolyte is required to have a density of at least 96% of the theoretical value, this value equates to the sample having closed porosity. Closed porosity is necessary as it means that there will be no continuous gas pathways through the electrolyte. Continuous gas pathways would allow the mixing of the individual gas streams that the electrolyte separates.

A highly sinterable powder is desirable not only because it means full density is likely to be achieved but also as it means less extreme sintering conditions can be employed, reducing energy costs and opening the possibility of co-firing electrode and electrolyte components. Electrolytes requiring high sintering temperatures to achieve closed porosity could preclude the option of co-firing components.

Initially sintering studies were performed to determine the lowest temperature/time combination that produced samples with a density of 96% or greater of the theoretical density.

The theoretical density for each powder is determined from the lattice parameters calculated from XRD data. The actual density of the sintered pellets was determined using an Archimedes method, these results are then expressed as a percentage value with respect to the calculated theoretical density.

The sintering regimes employed were 2 and 10 hours at 1300, 1400, 1500 and 1600 °C. It was only after sintering 10 hours at 1400 °C that the co-precipitated CG samples were produced with a density of at least 96% of the theoretical value. The sintering regimes in excess of this temperature all produced samples with densities greater than 96% of theoretical when performed using the co-precipitated powder.

The Pechini CG powder proved to be less sinterable than the co-precipitated powder, only attaining closed porosity (96% of the theoretical density) under the most extreme conditions: 10 hours at 1600 °C. The Pechini samples did show a more rapid initial densification attaining a density of 93% after 2 hours at 1400 °C as opposed to the 85% for the co-precipitated powder, however the density did not increase beyond this until the 10 hours at 1600 °C regime was used.

Based on these results it was decided to sinter all samples for 10 hours at 1400 °C. Sintering at higher temperatures could mean the volatilisation and loss of Ce from the sample. This phenomenon has been recorded by Van Herle et al.[28] when samples were sintered at temperatures above 1400 °C. More extreme sintering conditions would also encourage coarsening of the grain structure, which is generally considered an undesirable effect. It was also unknown how the double dopants would affect sintering, if the most extreme sintering regime had been opted for possible differences may have been missed.

Effect of Double Dopant on Sinterability

Density measurements of coppt double doped samples, all of which were sintered for 10 hours at 1400 °C, indicates that praseodymia containing samples were more sinterable than the other samples. This may be a product of the slightly smaller particle size of the praseodymia containing powders or possibly the praseodymia acts as a sintering aid. There was no systematic variation with praseodymia concentration but all of the praseodymia containing samples achieved densities 98-99% of theoretical. By contrast the CG material had achieved only 96%. Samaria double doping did not appear to have a significant effect on the density attained, the samples achieving closed porosity but failing to achieve the higher densities exhibited by the praseodymia containing pellets.

4.3.4 X-ray Microscopy

X-ray microscopy was used to examine density variation within both green and sintered pellets. The purpose for the examination was to determine if the powder preparation route strongly affected the density variation within a pellet; also whether a strong correlation existed between density variations in the green pellet and the sintered pellet and the effect of the sintering temperature on this relationship. Density variations within a sintered pellet could mean that there would be regions of higher and lower conductivity, as it is known that samples with a lower total density exhibit lower conductivities[29].

Large variations in density are also likely to cause mechanical weakness within the pellet, however mechanical testing was outside the scope of this research.

Figure 4.35A-D show the x-ray micrographs of pellets prepared from the coppt CG powder. The green pellets were prepared under identical conditions, however the coppt pellets were not fabricated using a binder while the Pechini pellets were. The sintered pellets represent the products of the least extreme (2 hours at 1300 °C) and most extreme (10 hours at 1600 °C) sintering conditions.

It is apparent that both of the green pellets show variations in density as indicated by the presence of light and dark regions on the micrograph (light regions equate to lower density). Both of the sintering regimes shown are postulated to have reduced the density variations that were present in the green pellets, as evidenced by the general lack of colour variation. The pellet sintered at 1300 °C still shows a small number of features from the green pellet, unlike the pellet sintered at 1600 °C, indicating that the higher sintering temperature is more effective at eliminating density variations present in the green pellet.

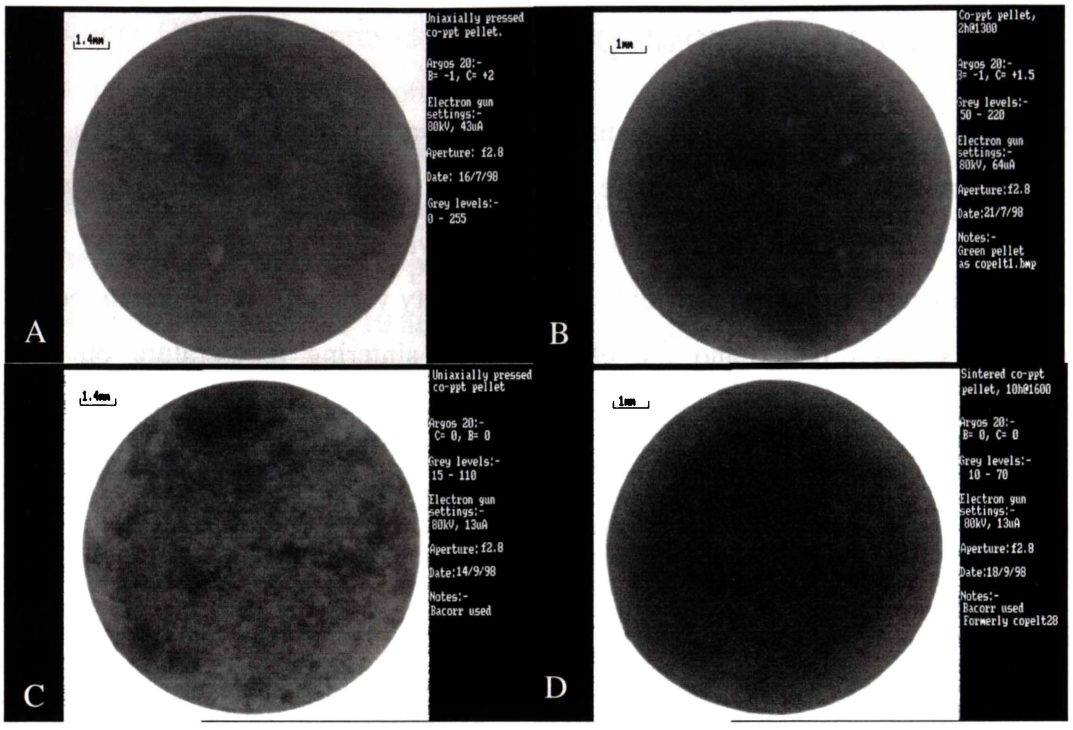

Figure 4.35 X-ray Micrographs of Pellets Prepared from Coppt CG.

A. Green pellet. B. Same pellet as A, after sintering 2 hours at 1300 °C.
C. Green pellet. D. Same pellet as C, after sintering 10 hours at 1600 °C.

In the sintered pellets it can be seen that the outer circumference has a lower density than the centre of the pellet. This is a product of the sintering process. Radial shrinkage during the sintering process causes the central regions to become more dense than the outlying regions.

Figure 4.36A-D show the x-ray micrographs of pellets prepared from the Pechini CG powder. It can be seen that the green pellets have a very uniform density, particularly when compared to the green pellets prepared from the coppt CG powder. The sintered Pechini pellets also show the density variations seen in the sintered coppt pellets, that is the centre of the pellet being more dense that the outer regions.

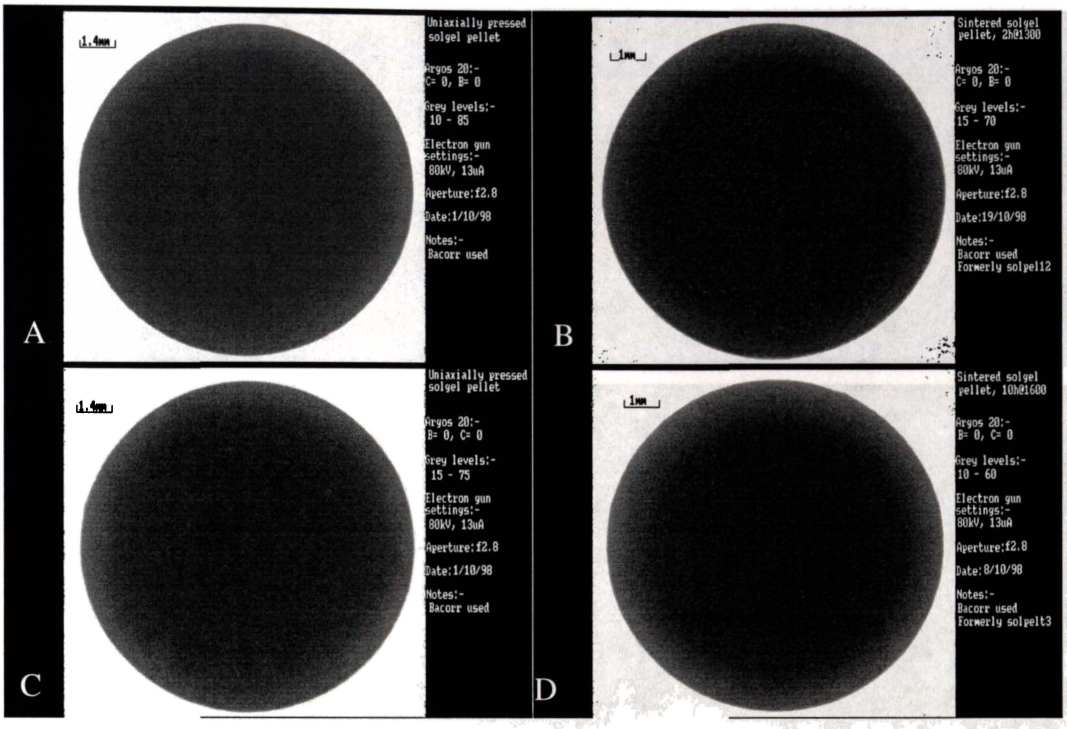

Figure 4.36 X-ray Micrographs of Pellets Prepared from Pechini CG.

A. Green pellet. B. Same pellet as A, sintered 2 hours at 1300 °C.
C. Green pellet. D. Same pellet as C, sintered 10 hours at 1600 °C.

The sintered pellets prepared from the two different types of powder (Pechini and coppt) appear to be quite uniform in density (ignoring the radial variations), despite the fact that there is a noticeable difference between the green pellets. It was decided to perform a higher magnification investigation of the sintered pellets. The micrographs of this investigation are shown in Figure 4.37A-D.

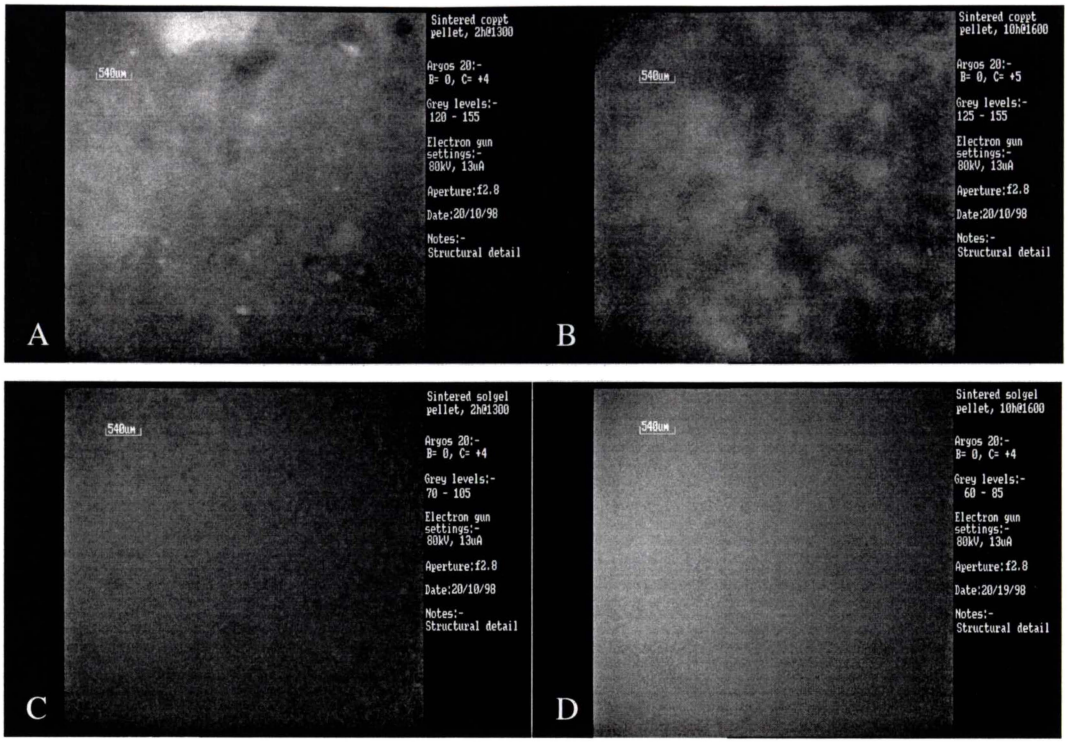

Figure 4.37 X-ray Micrographs - Increased Magnification.

A. Pellet prepared from coppt CG, sintered 2 hours at 1300 °C
B. Pellet prepared from coppt CG, sintered 10 hours at 1600 °C
C. Pellet prepared from Pechini CG, sintered 2 hours at 1300 °C
D. Pellet prepared from Pechini CG, sintered 10 hours at 1600 °C

From Figure 4.37 it is obvious that the sintered pellets from Pechini and co-precipitated powders are not as similar as they appeared at lower magnifications (Figure 4.35 and Figure 4.36). It can be seen that the pellets fabricated from the coppt powder show non-uniform density variations. This is more pronounced at the lower sintering temperature but is still significant in the samples sintered at 1600 °C. In contrast the Pechini pellets are very uniform, even at the lower sintering temperature of 1300 °C.

The only difference between the pellets, other than powder fabrication method, was that a binder was used for the fabrication of the Pechini pellets. This was investigated as a possible cause for the difference in density variations. A number of pellets were fabricated from the coppt powder, only this time a binder was used - this was the same binder, at the same loading, as used for the Pechini pellets. X-ray micrographs of these pellets are shown in Figure 4.38.

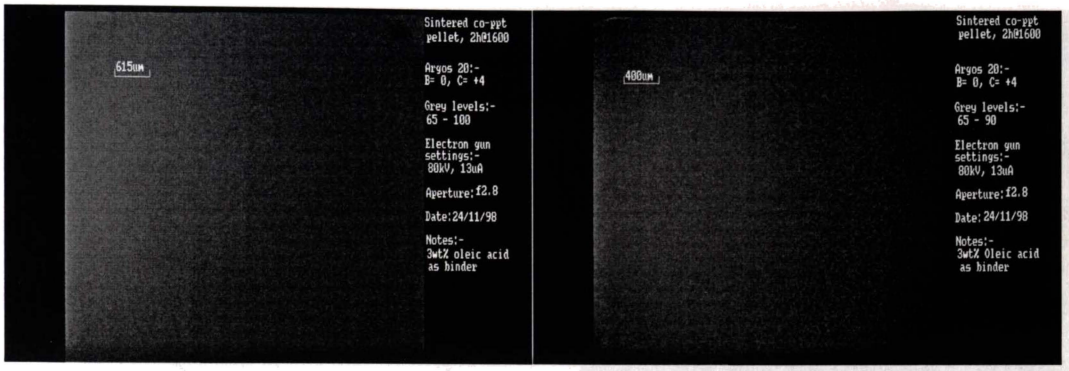

Figure 4.38 Sintered Coppt Pellets, Prepared Using a Binder.

It is noted that the addition of binder to the powder during pellet fabrication caused a dramatic change in the sintered pellet (compare Figure 4.38 to Figure 4.37A and B). This reduction of the density variation within the pellet is presumably due to the lubricant effect the binder material exhibits, allowing the powder particles to move past each other more easily during the compaction stage, allowing for a more even density in the green pellet, carrying through to the sintered item.

Regarding the radial density variations observed in sintered pellets, it was possible that the effect may have been a product of the method of x-ray generation and detection. This is plausible; as the x-rays diverge from a point source until they are detected by the detector the rays travel slightly different distances and hence lose different amounts of energy. To eliminate this possibility the samples were shifted off centre and re-examined. As can be seen in Figure 4.39 the radial density variation can still be noted without distortion, it is therefore concluded that these features are not instrumental in origin.

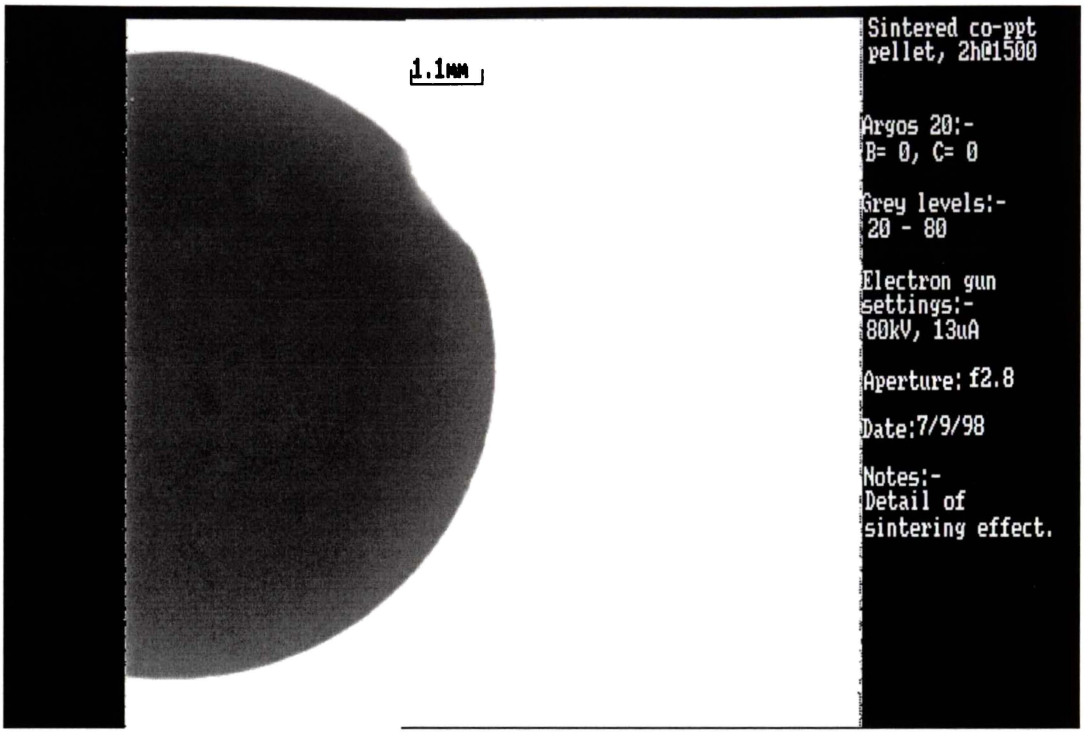

Figure 4.39 X-ray Micrograph of an Off-Centre Sample.

The possibility was also raised that the sample holder, a folded filter paper, may have contributed to the some of the features noticed. This possibility was also investigated, by specifically attempting to detect the holder.

As can be seen in
Figure 4.40, the filter paper holder can be made out, though only when the image is adjusted to contain only a narrow range of grey levels at the upper end of the scale. This image adjustment renders all details of the pellet, other than shape, unintelligible. Image adjustment for pellet details take the form of narrowing the grey levels present, though at the lower end of the range. It was concluded that the sample holder had no effect on the imaging of the pellets with respect to imposed density variations.

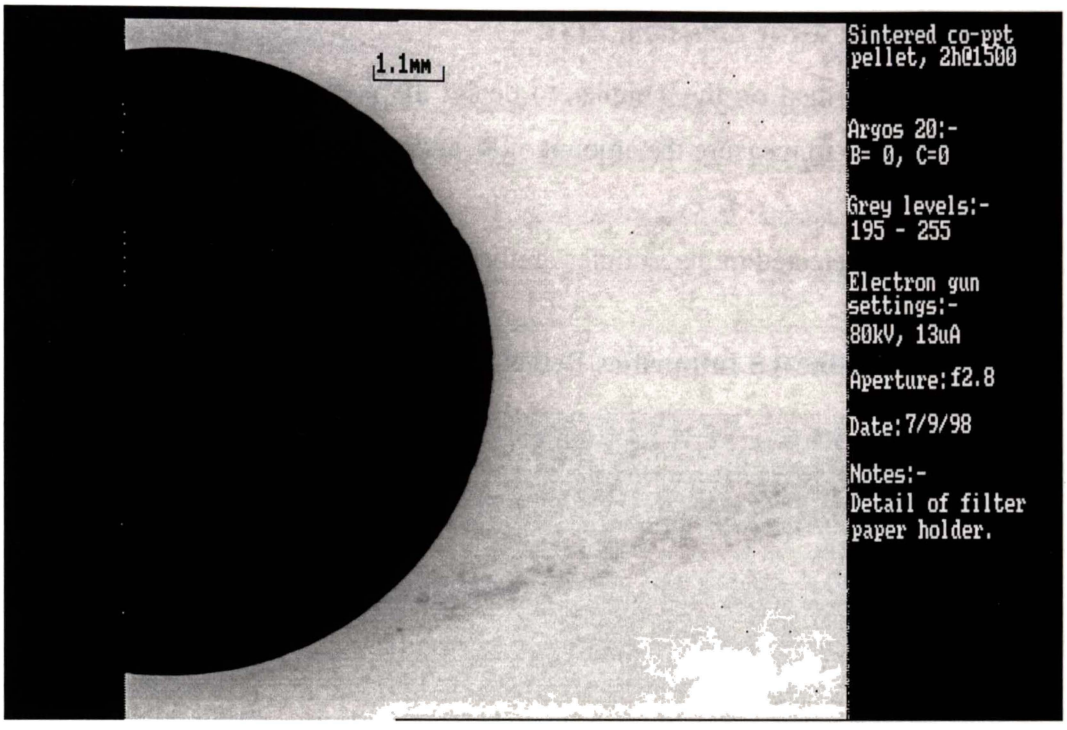

Figure 4.40 X-ray Micrograph - Holder Features.

4.3.5 Ion Beam Analysis, IBA

Due to limited beam time ion beam analysis was only performed on the CG, CGP005, CGP01, CGP015, CGP03 and CGP05 compositions prepared by co-precipitation. The purpose of subjecting the samples to IBA was an attempt to determine compositional differences beyond those one would expect based on stoichiometric considerations.

Nuclear Reaction Analysis, NRA

NRA was one of the methods employed to determine oxygen levels present in the samples. The depth of penetration was approximately 5.8 μm, and hence oxygen content is an average value from this depth to the surface. All of the samples showed an oxygen content of 39.6 ± 0.4 atom%. This is significantly below the amount expected based on the stoichiometry of the samples. Based on the stoichiometry one would expect an oxygen content in the range of 65 atom%. It is unknown why such a low result was obtained.

Particle Induced X-ray Emission, PIXE

PIXE was performed on the samples to detect the presence of impurities in the samples and also to measure the amount of Pr present.

The impurities detected in the samples are listed in Table 4.5.

Table 4.5 Impurities Detected in Sintered Samples.

Element	Average	Range
Ca	0.01 at.%	0.002 – 0.015 at.%
Fe	0.03 at.%	0.01 – 0.05 at.%
Co	0.17 at.%	0.15 – 0.2 at.%
Mo	0.01 at.%	0.001 – 0.011 at.%

It can be seen from Table 4.5 that the most abundant impurity element is cobalt. This is not of great concern as Lewis et al.[30] have intentionally added Co_3O_4 to doped ceria samples as a sintering aid. Co_3O_4 was added at a maximum loading of 4 cation%. It was found that levels between 1 and 4 cation% had beneficial effects on the sample, below 1 cation% no measurable effect was observed. Therefore one would expect that the amount of cobalt present in these samples would have no deleterious effect.

Gd was detected in the samples at a level of approximately 8 atom%. This is slightly higher than what one would expect based on the nominal compositions of the samples, which indicate a range from 5-7 atom%.

It was attempted to measure the amount of Pr present, however the results were ambiguous as the Pr was present at low levels and the Pr-L x-ray line lies very close to the strong Ce-L x-ray line.

Rutherford Back Scattering, RBS

RBS was performed on the samples as another method of determining the oxygen content of the samples, more specifically from the surface to a depth of approximately 4 μm. RBS is a standardless method, where the results are modelled using RUMP code to obtain the composition. The simulation lines in the following figures are those for the nominal sample compositions.

Figure 4.41 shows a typical result obtained for the majority of samples tested. The samples show a stoichiometry close to that of CeO_2 from the surface to the maximum depth of testing. This result would put into doubt the results obtained through NRA.

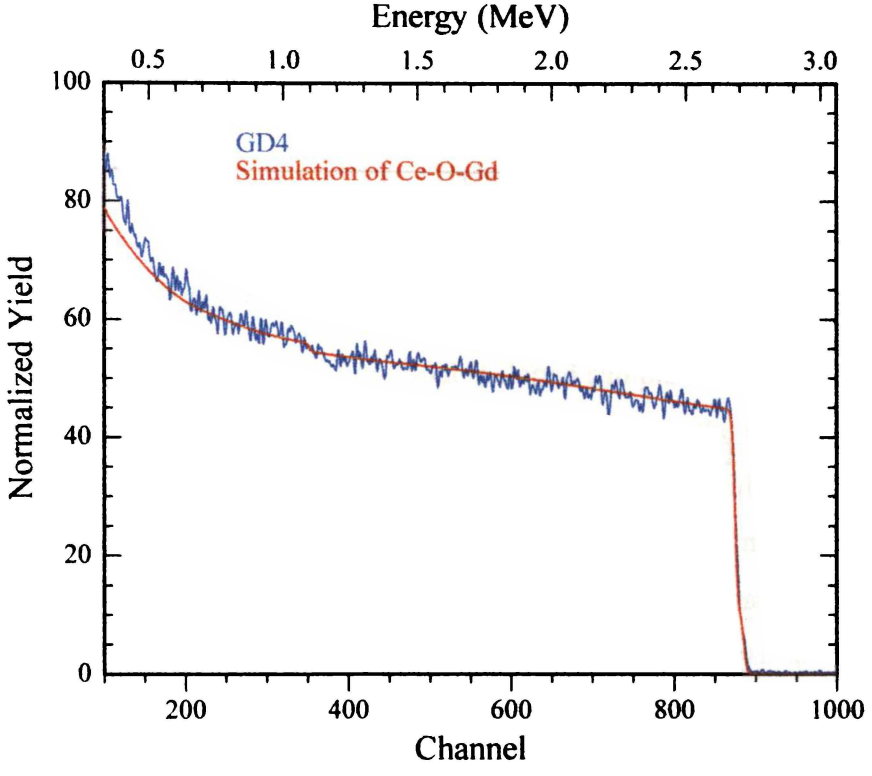

Figure 4.41 RBS Spectra Representative of most Samples.

Unlike the majority of samples CGP005 showed the presence of oxygen enrichment at the surface. This is indicated by decreased back scattering yield, compared to the simulation of the stoichiometric compound, for the heavier elements, channels 800-900, in Figure 4.42. Simulation of this result using RUMP code indicates that there is oxygen enrichment in the first 1000 nm.

The surface having 73 ± 2 atom% continuously decreasing to 66 ± 2 atom% oxygen at a depth of 1 μm.

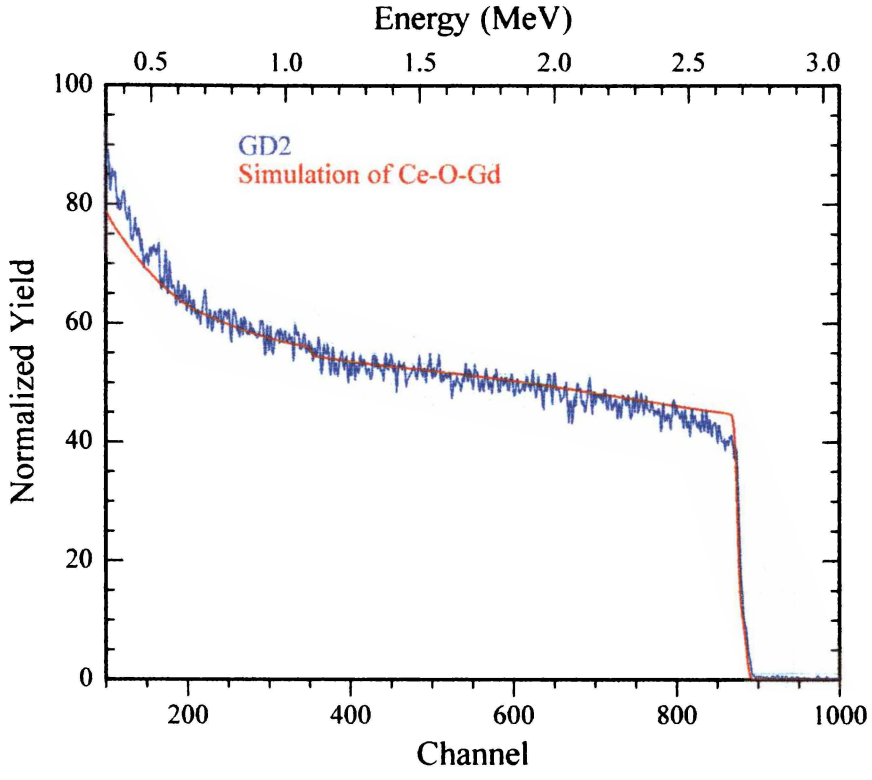

Figure 4.42 RBS Spectra of Sample Showing Oxygen Enrichment.

4.3.6 SEM of Pellets

SEM investigation of the sintered pellets was performed to gather information about grain size and shape. Grain size information can be used to judge the sinterability of a powder, as evidenced by the presence of porosity or grain coarsening.

Effect of Sintering Regime

Pellets sintered at different temperatures were investigated using SEM. It was seen that samples that had not achieved a density of 96% of theoretical showed a high amount of porosity, while samples that had achieved a higher density did not.

Figure 4.43 shows pellets sintered 2 hours at 1300 °C and 10 hours at 1600 °C, in addition to the differences in porosity, it can also be seen that the pellet sintered at 1600 °C has very large grains - in places in excess of 20 μm, indicating that grain coarsening has occurred.

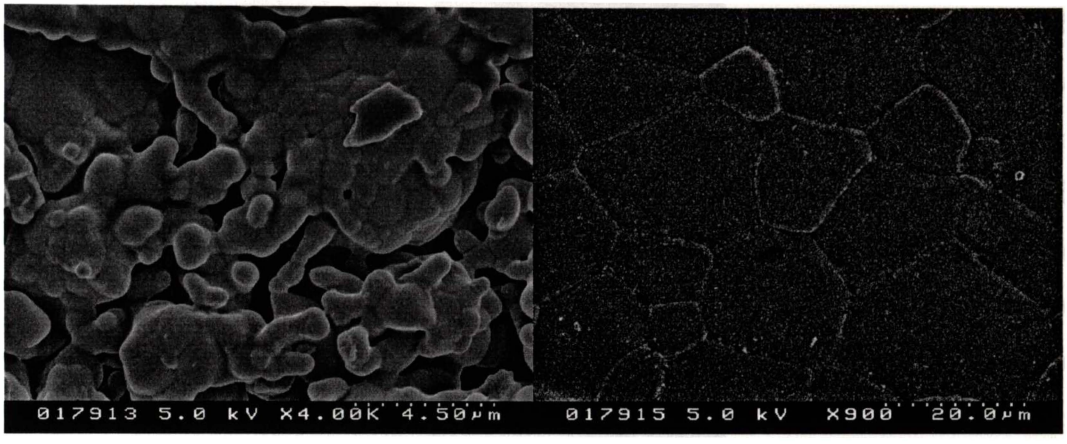

Figure 4.43 SEM Micrograph of Different Sintering Regimes.

Left: 2 hours at 1300 °C, Right: 10 hours at 1600 °C

Effect of Double Dopant

Inspection of the SEM images of the double doped samples reveals that all of the double doped samples have smaller grain sizes compared to the base CG material. There does not appear to be any systematic variation with double dopant concentration or double dopant type. All the double dopant samples show a grain size of 1.0 ± 0.1 μm. In comparison the CG pellets show a grain size of 2.6 ± 0.1μm. Figure 4.44 shows SEM micrographs of sintered pellets illustrating the differences in grain size between the base material and double doped samples. It can be seen that all three samples show grains of similar shapes, generally 5 - 8 sided in nature; the praseodymia and samaria containing samples show grains significantly smaller than the base CG material.

This difference in grain sizes is not due to different sized starting powders as all of the powders had very similar particle sizes. Normally with samples of high density, such as those examined, one would attribute the grain size difference to differences in the powder sinterability.

A highly sinterable powder will attain high density rapidly, subsequent heat treatment in excess of that required for densification will lead to grain growth. One could therefore assume that the CG powder was highly sinterable and had undergone grain growth (due to the larger grain size compared to the double doped samples). However from the sintered density results this would not appear to be the case as the sintering regime employed (10 hours at 1400°C) was the first one at which the CG samples attained closed porosity (96% of the theoretical density); one would therefore not expect to observe grain growth due to excess heat treatment. It would therefore appear that both samaria and praseodymia act to impede grain growth in the samples, as shown in Figure 4.44. This is desirable, as large grain sized items are mechanically weaker than their fine grained counterparts[28].

Figure 4.45 shows SEM micrographs of sintered pellets prepared from the Pechini powders. It can be seen that these too follow the trend of the double doped samples having smaller grain sizes than the base material, CG. It is also noted that the grain sizes of these samples are very similar to those obtained for the samples prepared from the co-precipitated powders. There is no significant difference between the shape of these grains and those of samples prepared from co-precipitated powders. There is some residual porosity present and also evidence of grain pull-out from the polishing process. Grain pull-out to this extent was not evident in samples prepared from the co-precipitated powder, possible indicating that the Pechini samples have a lower mechanical strength, though that is outside the scope of this research.

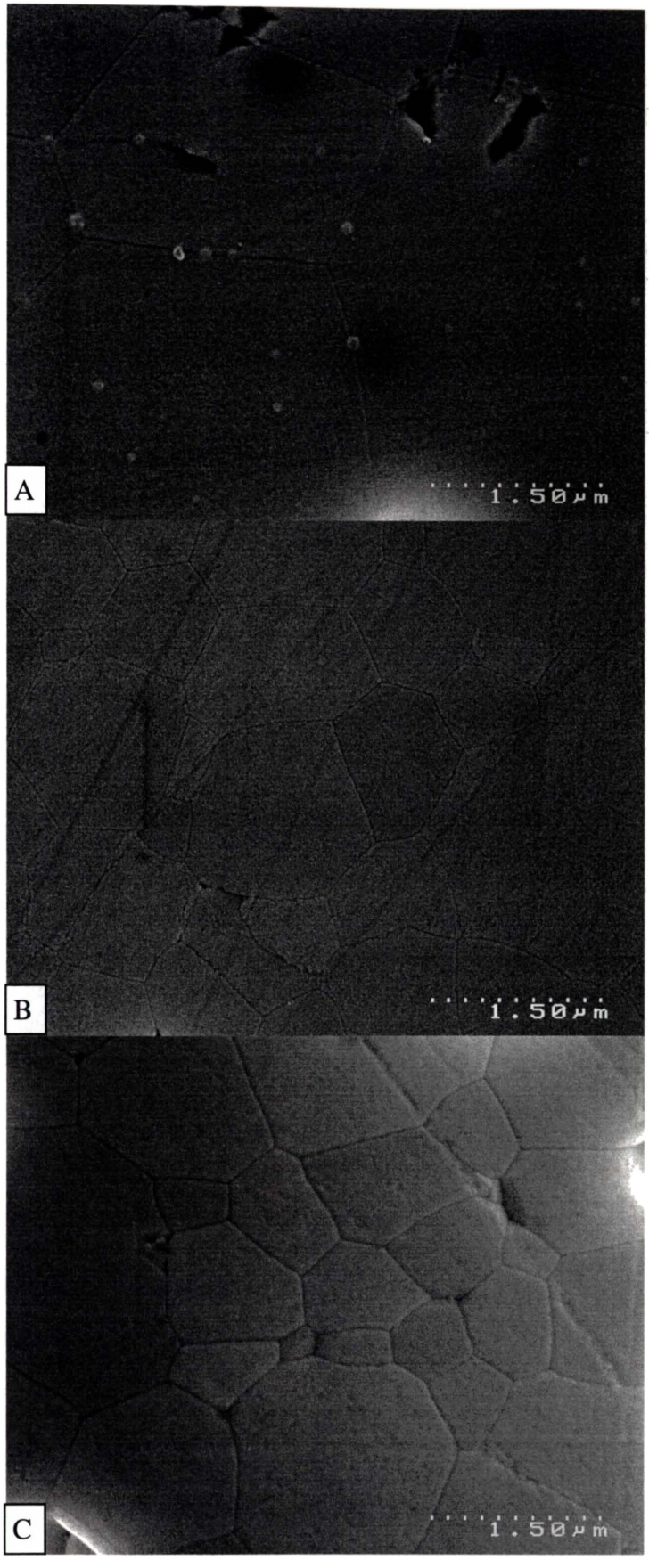

A = CG

B = CGP005

C = CGP05

Figure 4.44 SEM Micrographs of Sintered Pellets Prepared from Coppt Powders.

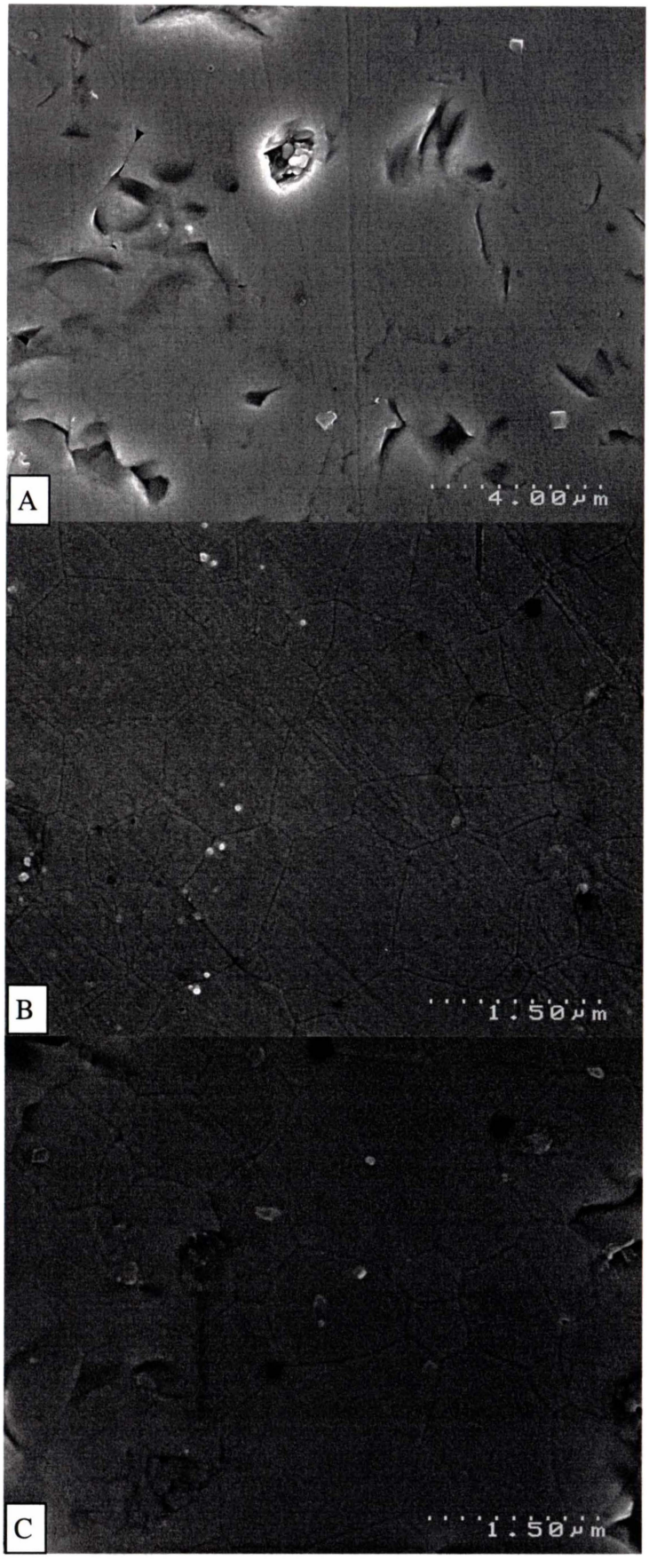

A = CG

B = CGP03

C = CGS03

Figure 4.45 SEM Micrographs of Sintered Pellets Prepared from Pechini Powders.

Other Imaging Modes

In addition to the standard secondary electron imaging of the samples, backscattered electron imaging and x-ray elemental analysis were performed. In backscattered electron imaging the contrast observed is due to differences in atomic number. Energy dispersive x-ray analysis (EDX) detects the x-rays emitted by the elements present when subjected to a high energy electron beam; each element will emit x-rays of characteristic energy and wavelength. These methods were employed in an attempt to detect evidence of solute segregation. Solute segregation having been identified by other researchers as one of the causes of the 'Grain Boundary Effect'.

In the backscattered images atomic number contrast was scarcely observed, as displayed in Figure 4.46.

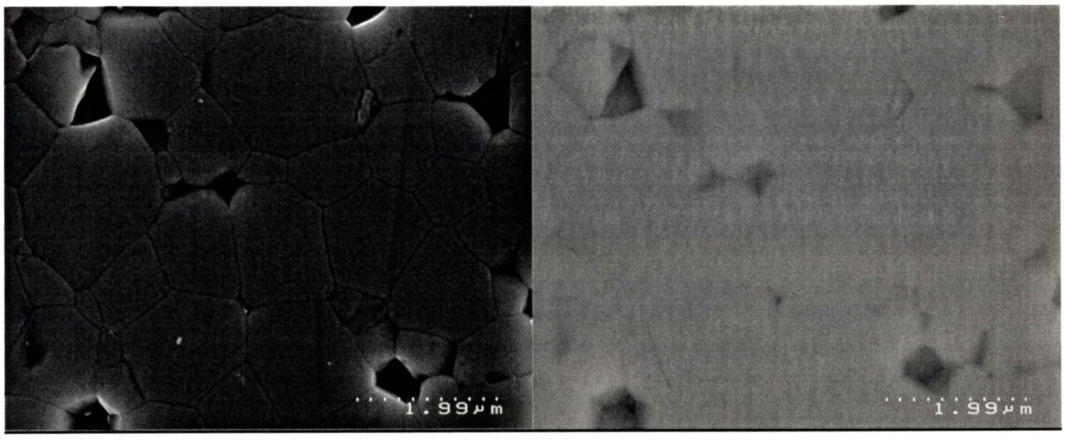

Figure 4.46 CGP05 - Secondary Electron Image (Left), Backscattered Image (right).

Elemental mapping of the sample, using EDX, showed the samples to have uniform elemental distributions, as displayed in Figure 4.47.

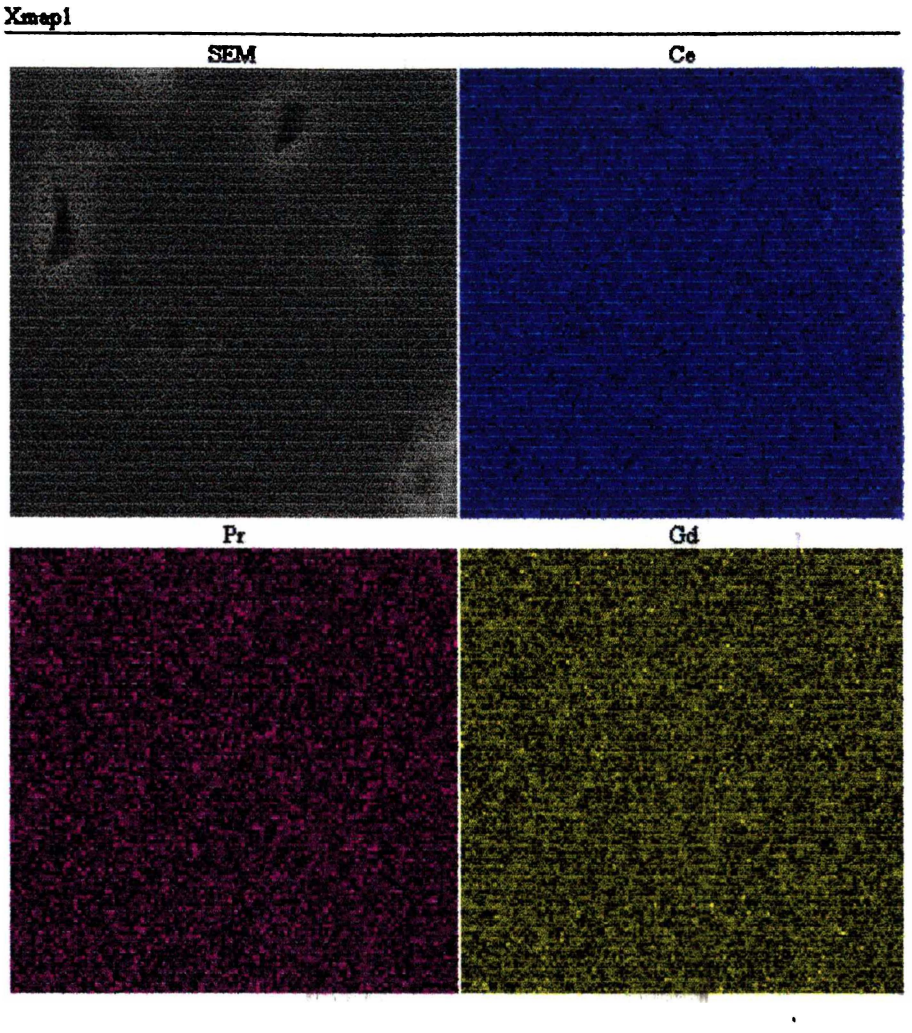

Figure 4.47 Elemental Mapping of CGP05 Pellet.

Based on the electron backscattering images and EDX analysis there does not appear to be any detectable solute segregation in the samples.

4.4 Impedance Spectroscopy

Impedance spectroscopy was performed on all samples to evaluate their conductivity properties. Initial measurements were performed at different temperatures under air and subsequently at a constant temperature while the oxygen partial pressure was varied. As the materials investigated for this thesis are intended as electrolytes for SOFCs their conductivity properties are important.

Measurements made at different temperatures enable the determination of activation energies for the samples, while measurements made at different oxygen partial pressures allow the determination of the ionic domain boundary.

4.4.1 Complex Plane Results

Figure 4.48 and Figure 4.49 are examples of the complex plane graphs obtained from the impedance spectroscopy method. It can be seen at the lower temperature, Figure 4.48, that clearly resolved arcs are present. The arc at lower real impedance values is attributable to lattice processes, while the smaller arc at higher impedances is due to grain boundary processes; the final portion of the graph arises from electrode processes[31]. By fitting semi-circles to these arcs real axis intercepts can be determined for the calculation of conductivities. The real axis values are proportional to the resistance of the system which, through the use of a simple mathematical operation yields the conductivity of the sample. The imaginary impedance value for the apex of the semi-circle is proportional to the capacitance of the associated process.

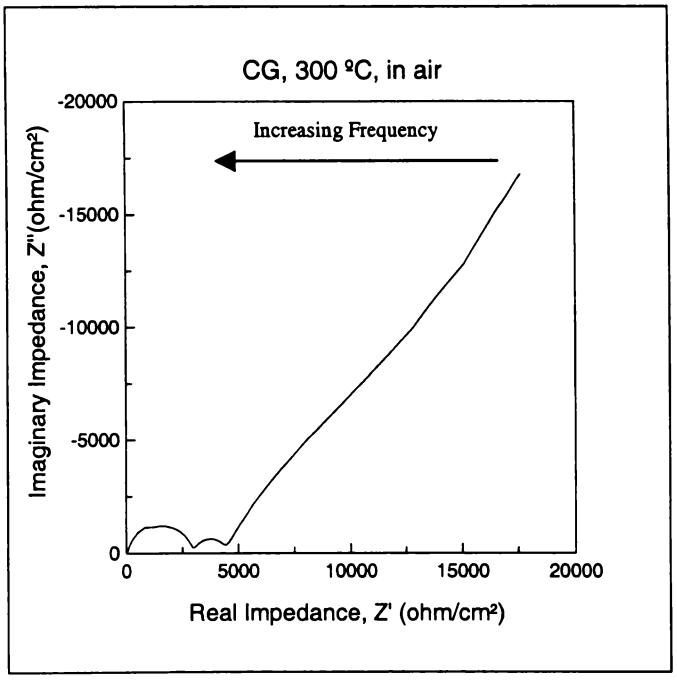

Figure 4.48 Complex Plane Impedance Plot.

In Figure 4.49 it is seen that at elevated temperatures the arcs can no longer be resolved, and that the impedance values at higher frequencies have been forced into the positive imaginary impedance domain. In these cases the real axis intercept was used to calculate the conductivity of the sample.

This type of variation with temperature is well known[31]. As the temperature increases the time constants associated with the different processes become smaller, resulting in the separate arcs merging.

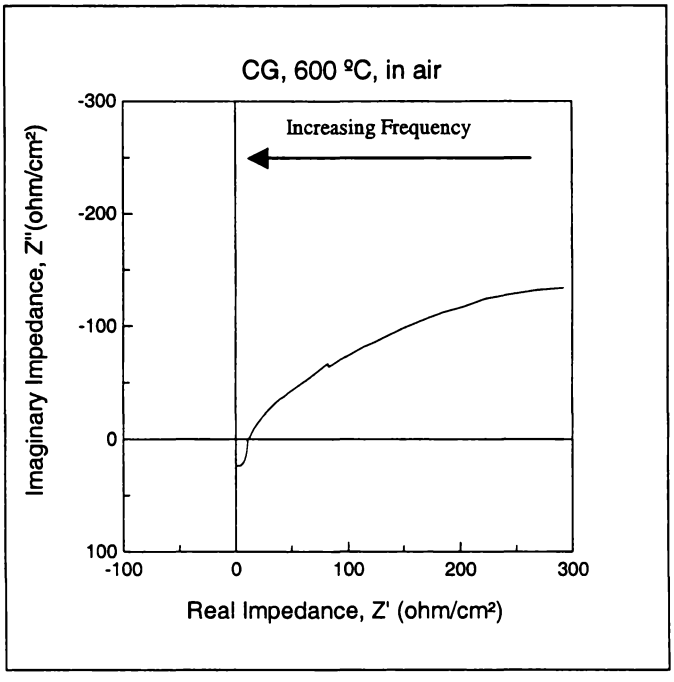

Figure 4.49 Complex Plane Impedance Plot.

The complex plane results obtained for the samples show that all of the double doped samples prepared by co-precipitation, except the CGS03 sample, have grain boundary arcs significantly smaller than the lattice arc. Figure 4.50 shows the complex plane data for CG, CGS01 and CGS03 samples. The CG samples have grain boundary arcs smaller than the lattice arc, but not to the same extent as the double doped samples. It is not known why the CGS03 sample has such a large grain boundary arc. CGS01 is included as an example of the majority of the double doped samples. One should be aware that the results in Figure 4.50 while having been normalised for the samples area, have not been normalised for sample thickness and hence only relative arc sizes can be compared.

The observation that most of the co-precipitated samples show grain boundary arcs smaller than the lattice arc, indicating a lower resistance, is not usually observed in fluorite type oxygen ion conductors. One normally expects the grain boundaries to have a higher resistance[32], sometimes reducing the electrical performance by three orders of magnitude[33].

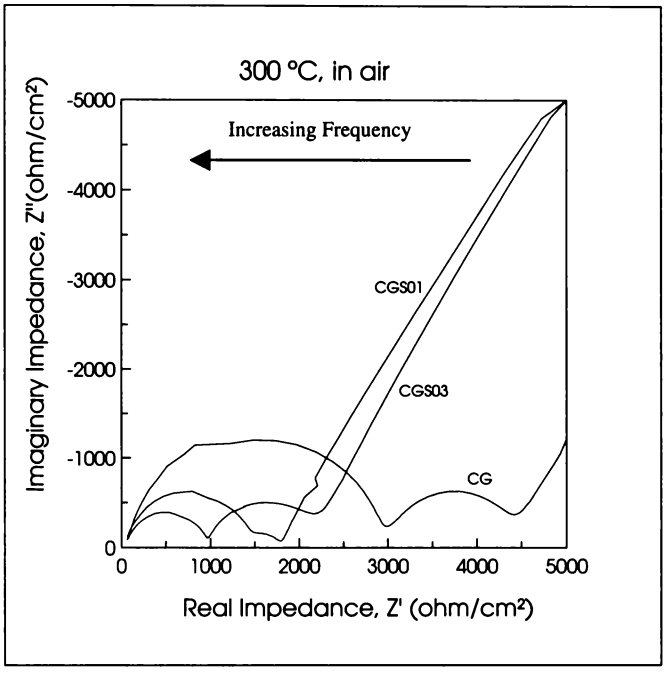

Figure 4.50 Complex Plane Impedance Plot.

Pechini Samples

The three compositions prepared by the Pechini method also showed well defined arcs at low temperatures that merged as temperature was increased. The Pechini CGP03 and CGS03 showed large grain boundary arcs, larger than the lattice arc, this indicates that these samples have grain boundaries that are more resistive than the lattice - this is the situation normally encountered. The Pechini CG sample has a very small grain boundary arc, becoming difficult to detect above temperatures of 350°C.

4.4.2 Conductivities

Conductivity results, obtained through impedance spectroscopy, were collected over a range of temperatures, at each temperature the same trend was observed, as displayed in Figure 4.51.

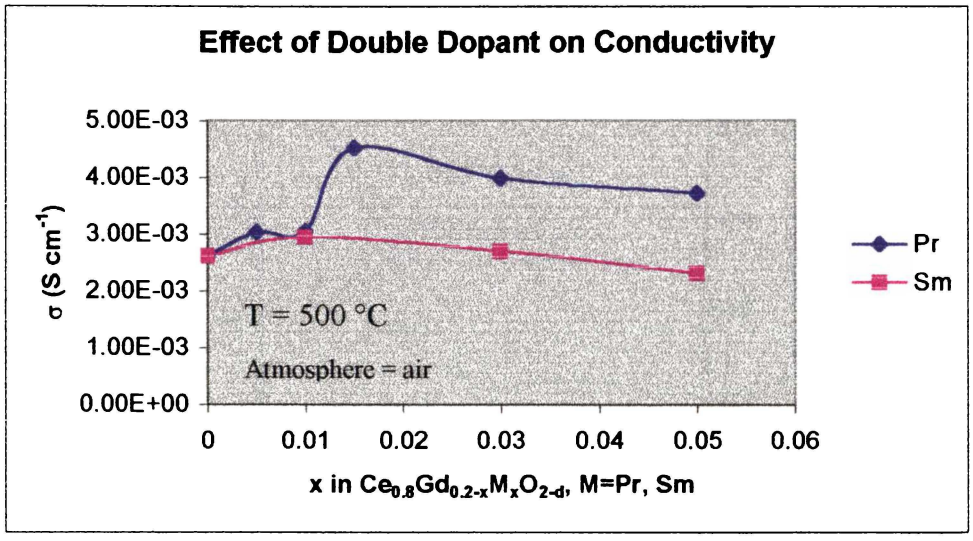

Figure 4.51 Isothermal Plot of σ versus Double Dopant Content.

It can be seen that for each of the double dopants a maximum in conductivity is reached. For praseodymia this maximum is at x = 0.015, while for samaria it is x = 0.01, though the maximum for samaria is broad and may occur at a slightly higher Sm content. It is noted that all praseodymia containing compositions exhibit higher conductivities than the CG material (x = 0), while the sample with the highest samaria content shows a conductivity lower than CG, though the difference is not very marked.

The conductivity for Pr = 0.01 is lower than one would have expected based on the general trend established from the other samples. This CGP01 sample has shown anomalous results in other areas namely crystallite size and Raman spectroscopy. In the Raman spectrum the band attributed to oxygen vacancies was lower in intensity than expected based on the trend shown by the other samples.

As the temperature of testing increased, the conductivity exhibited by the samples increased as shown in Figure 4.52. For clarity only the CG, CGP015 and CGS01 results are shown. This increase in conductivity was expected, as the increase in temperature increases the mobility of the charge carriers present in the sample.

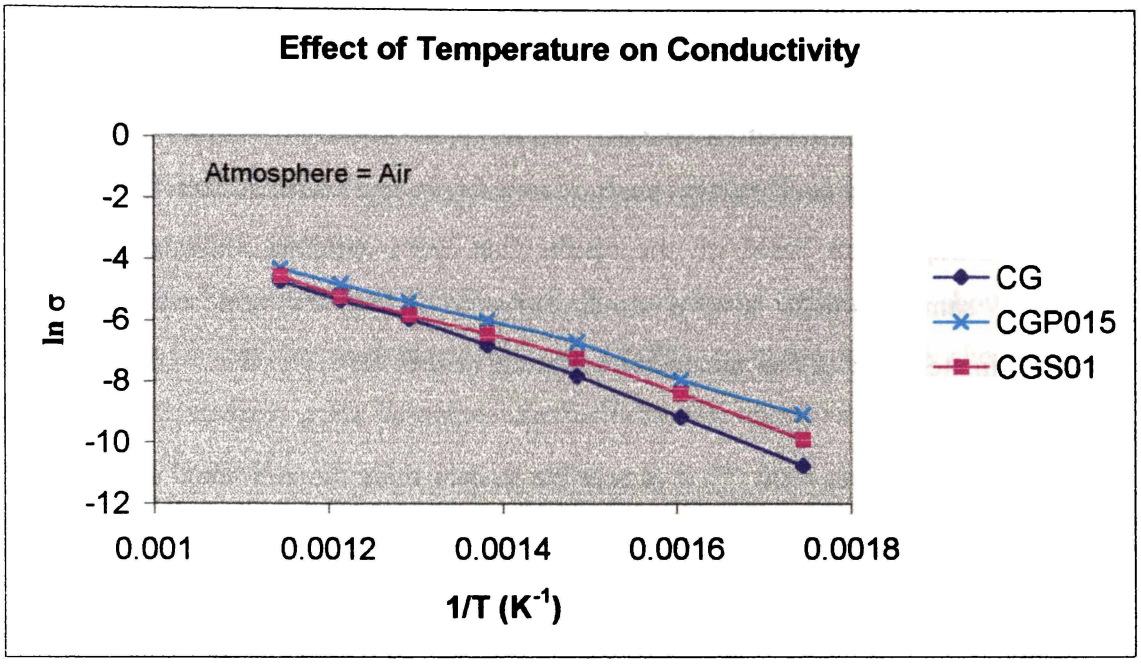

Figure 4.52 Conductivity of Samples in Air.

The conductivities for CG, CGP015 and CGS01 at 600 °C were 8.89 x 10^{-3}, 1.33 x 10^{-2} and 1.04 x 10^{-2} S cm^{-1} respectively. Lubke et al.[34] also measured conductivities at this temperature and the results obtained here compare favourably; Lubke et al. having obtained a conductivity of 4.1 x 10^{-3} S cm^{-1} for $Ce_{0.8}Gd_{0.2}O_{1.9}$. Lubke et al. did not test a composition equating to the CGP015 tested here, however they did test compositions that are the same as CGP01 and CGP03. The conductivities they obtained for these compositions were 3.4 x 10^{-3} and 9.4 x 10^{-3} S cm^{-1} respectively, the results from this work were 1.01 x 10^{-2} and 1.26 x 10^{-2} S cm^{-1}. It would appear, based on measured conductivities, that the samples prepared for this work are superior to those of Lubke et al. Estimation of the conductivity of CGP03 at 600 °C from the graph included in the work of Maricle et al.[35] gives a result of approximately 1.3 x 10^{-2} S cm^{-1}.

While this result is higher than that obtained for the CGP03 composition in this work, the CGP03 composition was the one they determined to have the highest conductivity of the compositions tested. For this work the CGP015 composition gave the highest conductivity (1.33×10^{-2} S cm^{-1}), therefore when these best performing samples are compared the results are very similar.

Maricle et al.[35] also prepared a samaria double doped sample, which was observed to have a measured conductivity of approximately 4.3×10^{-2} S cm^{-1} at 700 °C. Although conductivity measurements were not made at 700 °C for this work, extrapolation based on the results that were obtained indicate that the CGS01 sample would have a conductivity of 2.1×10^{-2} S cm^{-1} at 700 °C, approximately half of that obtained by Maricle et al.[35].

At low temperatures (300 °C) it is possible to determine the individual lattice and grain boundary components of the overall conductivity, as clearly resolved arcs are present in the complex plane impedance graphs, these results are displayed in Figure 4.53.

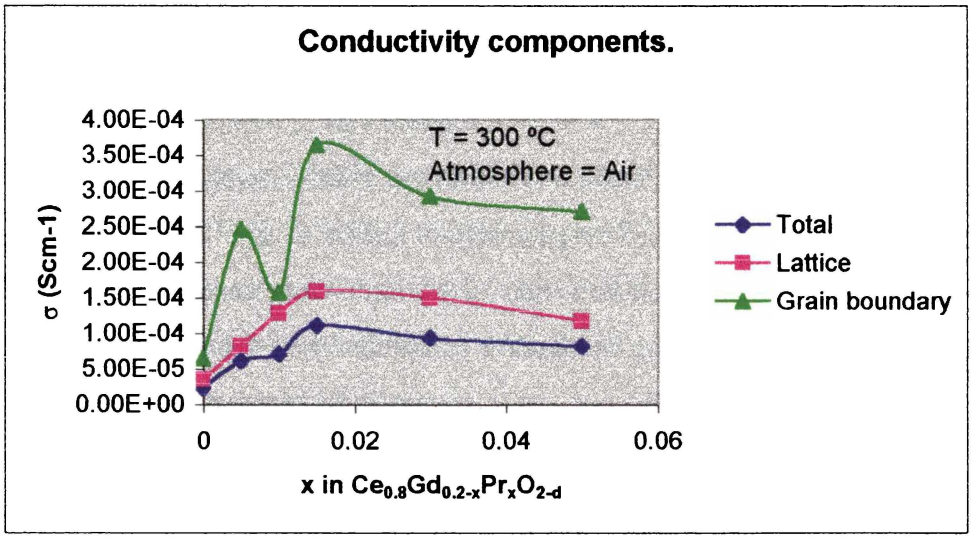

Figure 4.53 Conductivity Components of Pr Containing Samples.

It can be seen that the addition of Pr has an effect on both the lattice and grain boundary conductivities, with the grain boundary conductivity affected more than the lattice conductivity.

It can also be seen that the anomalous conductivity of CGP01, noted previously, is a result of a decrease in the grain boundary conductivity - despite backscattered electron imaging and EDX mapping showing no indication of solute segregation or grain boundary phases. These results confirm the surmise of Steele[32] that the addition of praseodymia acts to increase the conductivity of the grain boundaries, however there is also an increase in the intrinsic conductivity of the materials with praseodymia content. It should be recalled that lattice conductivities are considered to be intrinsic of the material, while grain boundary conductivities have been postulated as being dependent on processing/fabrication factors[33, 36].

Similar results were obtained for the samaria containing samples, as shown in Figure 4.54; it can be seen that only the CGS01 (x=0.01) sample shows a significant increase in grain boundary conductivity, the other compositions show only a slight increase.

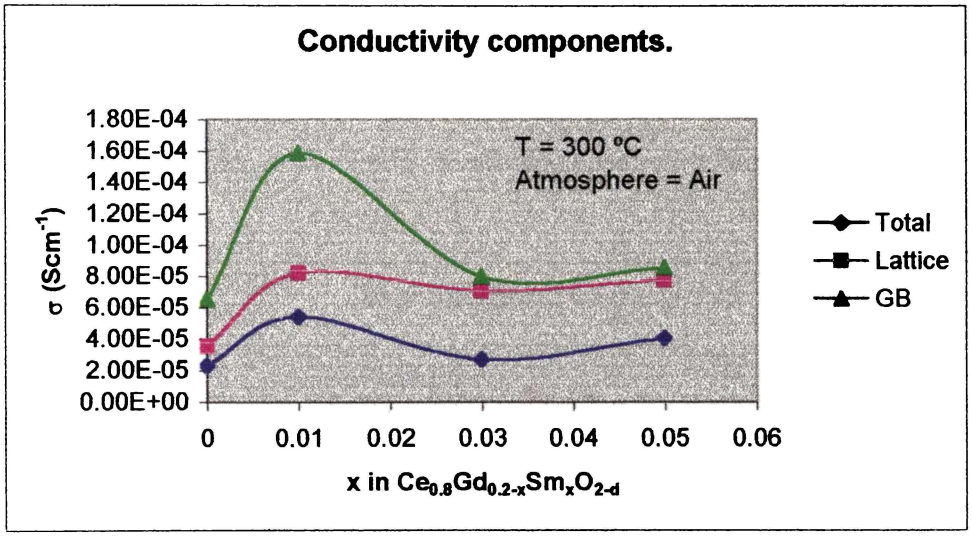

Figure 4.54 Conductivity Components for Sm Containing Samples.

Pechini Samples

The measured conductivities for the Pechini samples at 600 °C in air were 3.98 x 10^{-3}, 4.12 x 10^{-3} and 7.35 x 10^{-3} S cm^{-1} for CG, CGP03 and CGS03 respectively. As can be seen from Figure 4.55 this is significantly lower than the co-precipitated samples of these compositions.

Figure 4.55 also indicates that samaria double doping increases the conductivity of the material to a greater extent than praseodymia double doping. This effect is the inverse of that observed in the samples prepared by co-precipitation.

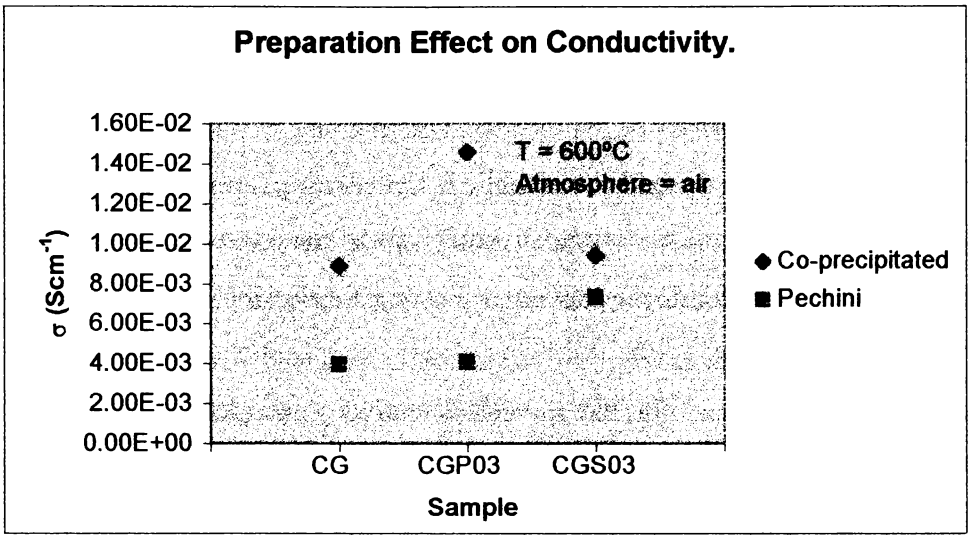

Figure 4.55 Conductivity Variation with Preparation Method.

The conductivities of the different sample components, that is grain boundary and lattice, were also calculated for the Pechini samples and are displayed in Figure 4.56, contrasted with the same results for the co-precipitated samples.

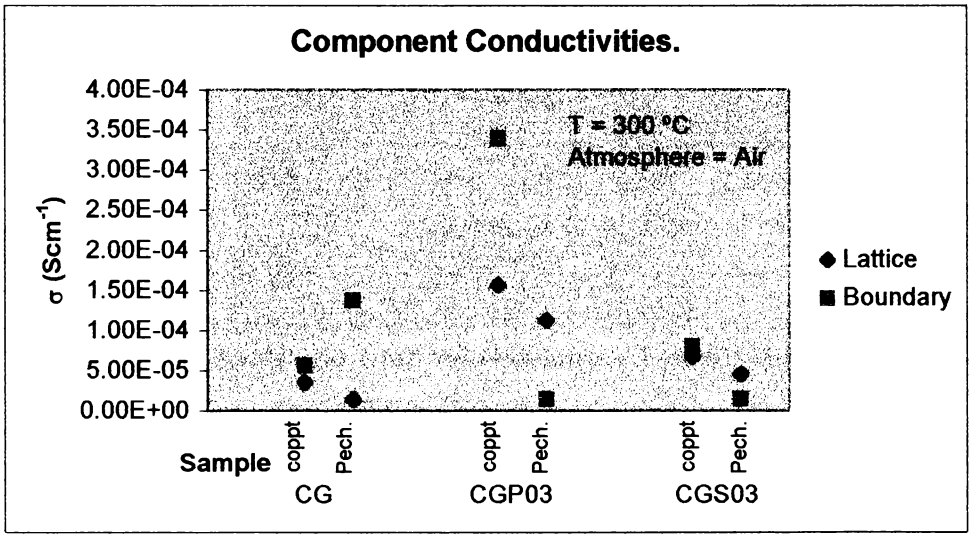

Figure 4.56 Component Conductivity Variation with Preparation Method.

It can be seen that there is no consistent variation between the preparation methods.

4.4.3 Activation Energies

From the results obtained measuring the conductivity at different temperatures it is possible to construct Arrhenius type plots, from which the activation energy for conduction can be determined. Figure 4.57 is an example of such a plot, it is noted that a change of slope was present at approximately 400 °C for all of the samples.. An explanation for this, proposed by Steele[32], is that the change in slope is due to different activation energies for grain boundary and lattice conductivities. Steele indicates that 'clean' gadolinia doped ceria (without grain boundary impurities) has a change in activation energy at ca. 400 °C. The fact that the samples for this work showed a change of slope in this same region further supports the assertion that the samples do not have grain boundary impurities.

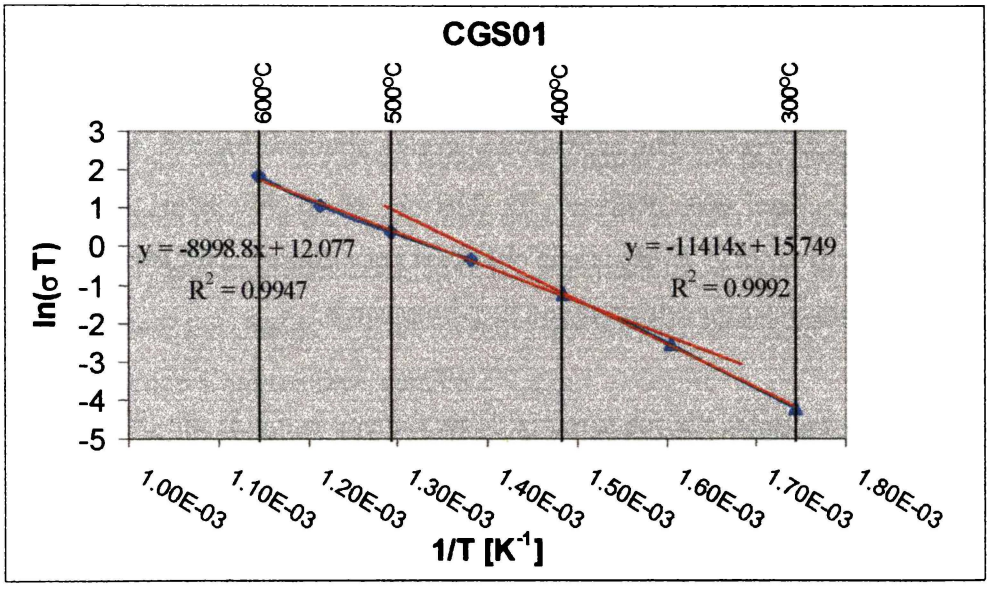

Figure 4.57 Arrhenius plot for CGS01

The total activation energies obtained by ignoring the change in slope for the praseodymia double doped samples are displayed in Table 4.6.

Table 4.6 Activation Energies of Praseodymia Double Doped Samples.

Sample	Activation energy (eV)
CG	0.88
CGP005	0.82
CGP01	0.79
CGP015	0.78
CGP03	0.80
CGP05	0.80

It can be seen that all of the praseodymia containing samples have lower activation energies than the CG base material. It is also noted that the CGP015 sample, which showed the maximum in conductivity also has the lowest activation energy. The activation energy measured for CG is identical to that obtained by Lubke et al.[34] for their samples, while the activation energies obtained for the praseodymia containing samples are higher than those of Lubke et al, who obtained 0.77 and 0.70 eV for composition corresponding to CGP01 and CGP03 respectively. The activation energies obtained for this work are also slightly higher than that obtained by Maricle et al.[35], who measured an activation energy of 0.73 eV for their optimum composition, compared with 0.78 eV for the optimum composition found in this research.

The activation energies for the samaria double doped samples are listed in Table 4.7.

Table 4.7 Activation Energies for Samaria Double Doped Samples.

Sample	Activation energy (eV)
CG	0.88
CGS01	0.81
CGS03	0.91
CGS05	0.85

It can be seen that CGS01, the samaria containing sample which showed the highest conductivity also has the lowest activation energy. Unlike the praseodymia containing samples, the higher levels of samaria have not reduced the activation energy to the same extent, in fact the CGS03 sample has a higher activation energy than the CG base material. While Maricle et al.[35] did study the CGS01 composition, they did not publish an activation energy for total conductivity.

As it is possible to resolve grain boundary and lattice conductivities using impedance spectroscopy, it is possible for activation energies for the two components to be determined. It should be recalled that the two components can only be separated at relatively low temperatures, in this case 300 - 450 °C. Figure 4.58 is an example of the graphs produced for the determination of the activation energies for the individual conductivity components. It can be seen that the lattice conductivity data still shows a change in slope at ca. 400 °C. As the grain boundary conductivity does not form a part of these results the 'different activation energies for lattice and grain boundaries' explanation proposed by Steele[32] cannot apply. A further possible explanation for the change in slope of the lattice conductivity is that there were dopant ion-oxygen vacancy pairs present and at the slope transition temperature the binding enthalpy of these was overcome causing a change in activation energy (dopant ion-oxygen vacancy pairs were discussed in Chapter One, section 1.7.3).

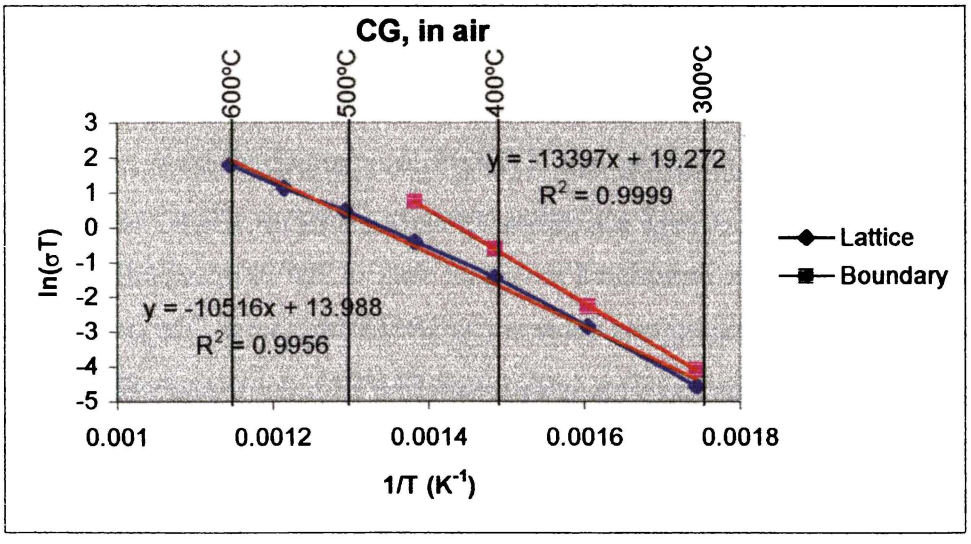

Figure 4.58 Arrhenius Plot for Different Conductivity Components.

The results obtained from these Arrhenius plots for the all of the samples are displayed in Table 4.8.

Table 4.8 Activation Energies for Conductivity Components.

Sample	Lattice activation energy (eV)	Boundary activation energy (eV)
CG	0.87	1.10
CGP005	0.90	0.80
CGP01	0.70	0.94
CGP015	0.76	0.76
CGP03	0.74	0.83
CGP05	0.74	0.92
CGS01	0.80	0.85
CGS03	0.84	1.08
CGS05	0.82	0.86

From Table 4.8 it can be seen that generally the activation energy for grain boundary conduction is higher than that for the lattice, though there are exceptions: for CGP005 the lattice activation energy is lower than the grain boundary activation energy and in the case of CGP015 the values are the same. Other researchers[32, 34, 35] have also found that the activation energy for grain boundary conduction is usually higher than that for lattice conduction. Of the praseodymia containing samples it is noted that CGP01 has the lowest activation energy for lattice conduction, not CGP015 as one might have expected (as CGP015 had the lowest total activation energy). However when grain boundary activation energies are considered it is seen that, of the praseodymia containing samples, CGP01 has the highest value and CGP015 the lowest. This indicates that the best performing composition, in this case CGP015, does not necessarily have the lowest activation energies for both of the component conductivities but the lowest overall activation energy.

The case is less ambiguous for the samaria containing samples, the CGS01 composition, determined earlier to be the best performing CGS system, has both the lowest lattice and grain boundary activation energies.

Pechini Samples

Only the Arrhenius plot (used to determine that activation energy of conduction) for the Pechini CG sample showed the clear change in slope exhibited by the co-precipitated samples, again at ca. 400 °C. Steele[32] indicates that samples showing no change in slope would be expected to be impure, though this was not evidenced when the samples were examined using backscattering electron imaging or energy dispersive x-ray analysis.

The overall activation energies determined for the Pechini CGP03 and CGS03 were identical to their co-precipitated counterparts, while the Pechini CG sample's activation energy was 0.02 eV higher than the co-precipitated sample (0.88 eV as opposed to 0.86 eV).

Individual component activation energies could not be determined for the Pechini CG sample due insufficient data. Results for CGP03 and CGS03 show that the activation energy for lattice conduction was lower compared to the co-precipitated samples, while the grain boundary activation energy was higher.

4.4.4 Effect of Oxygen Partial Pressure

The base CG material and the two double doped materials that exhibited the highest conductivities were studied by impedance spectroscopy under varying oxygen partial pressures.

The results of these studies are presented in Figure 4.59, Figure 4.60 and Figure 4.61.

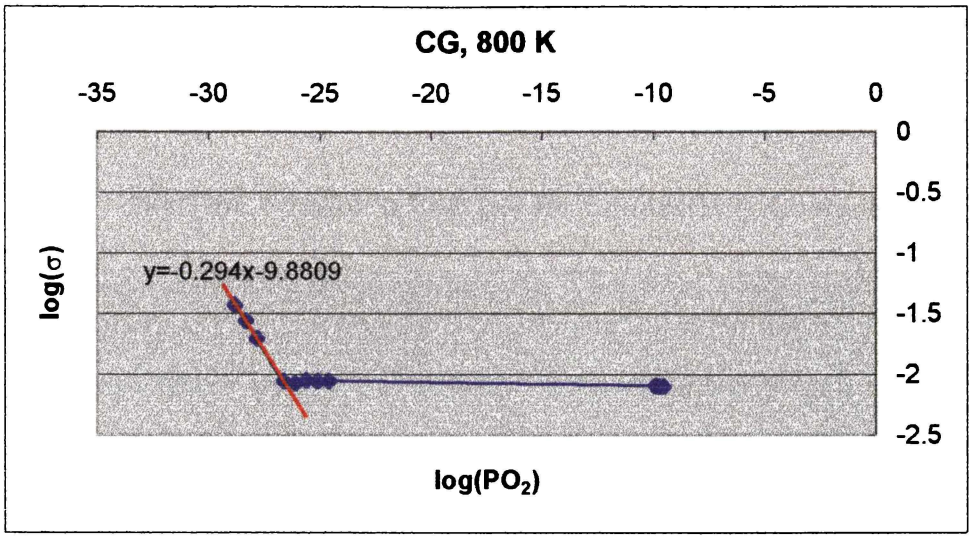

Figure 4.59 Effect of Oxygen Partial Pressure on Conductivity - CG.

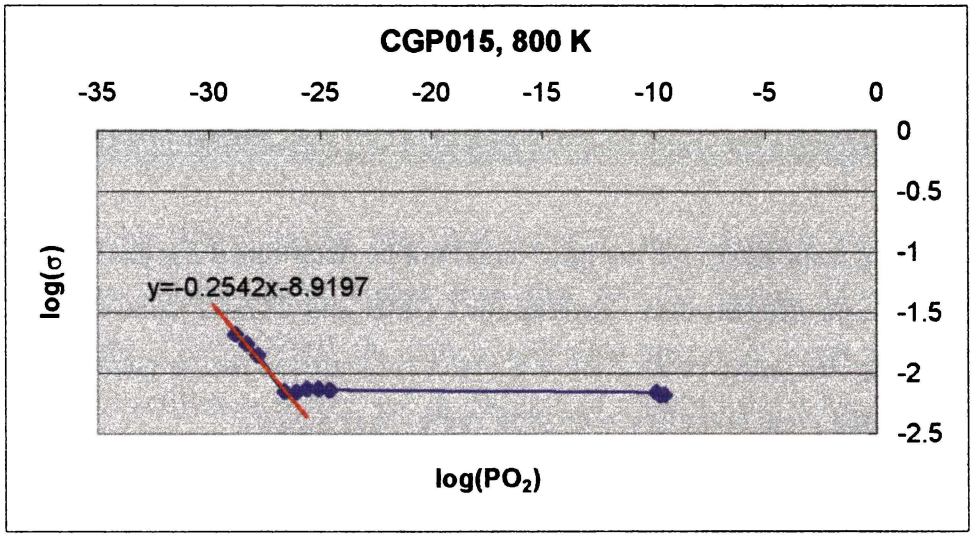

Figure 4.60 Effect of Oxygen Partial Pressure on Conductivity - CGP015

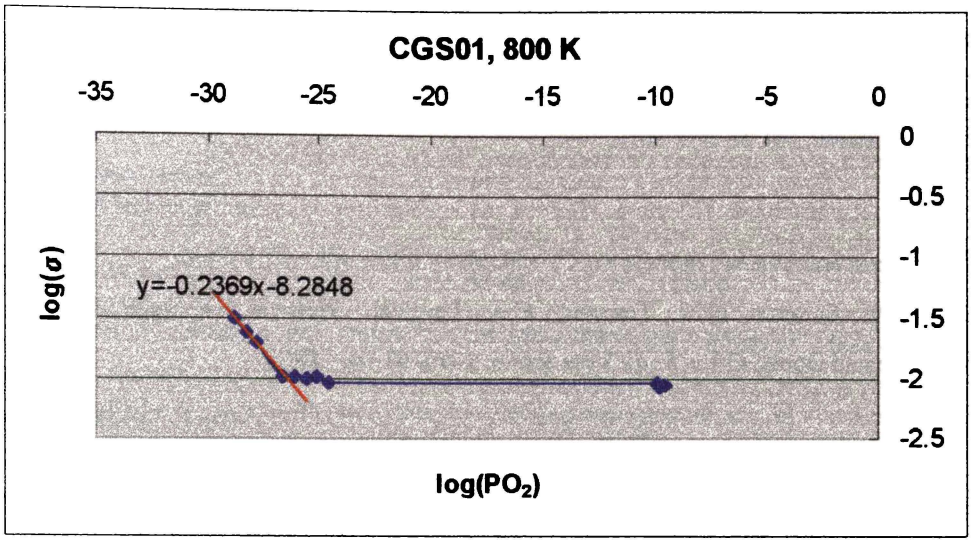

Figure 4.61 Effect of Oxygen Partial Pressure on Conductivity - CGS01

It can be seen from the above figures that all of the samples show evidence of electronic conductivity below approximately 10^{-26} atm. Therefore the ionic domain, where electronic and ionic conduction are of equal magnitude, is 10^{-26} atm. The slope of the electronic conductivity portion of the graphs ranges from -0.24 to -0.29, which is of the same order as the predicted slope of -0.25 (refer section 1.6.3). Calculation of the electrolytic domain boundary (EDB) yields values of 1.5×10^{-20} atm, 1.8×10^{-19} atm and 6.9×10^{-19} atm for CG, CGP015 and CGS01 respectively. The EDB, as defined by Gao and Sammes[4], is where the ionic conductivity is one hundred times the electronic conductivity of the material. In comparison to the work of Maricle *et al.*[35] the ionic domain of the materials studied is at a lower oxygen partial pressure. However their samples were tested at 973 K (compared to the 800 K used here) and hence one would expect a higher ionic domain partial pressure for them, as the ionic domain of a material contracts with increasing temperature. The ionic domain value of 10^{-26} atm for all three samples indicates that there appears to be no substantial extension of the ionic domain through the use of double dopants. Maricle *et al.*[35] reported a two order of magnitude extension of the ionic domain when praseodymia double doping was employed. Lubke and Wiemhofer[34] found only a slight increase in ionic domain. The EDB results for the samples studied in this research indicate that the use of double dopants may slightly decrease the EDB of gadolinia doped ceria.

Bibliography

[1] Hong, S. J., Virkar, A.V., Lattice Parameters and Densities of Rare-Earth Oxide Doped Ceria Electrolytes., *Journal of the American Ceramic Society,* **78**(2): p.433-439, (1995).

[2] Griffiths, T. R., Hubbard, H.V.St.A., Davies, M.J., Electron Transfer Reactions in Non-Stoichiometric Ceria and Urania., *Inorganica Chimica Acta,* **225**:p.305-317, (1994).

[3] Mogensen, M., Sammes, N.M., Tompsett, G.A., Physical, Chemical and Electrochemical Properties of Pure and Doped Ceria, *Solid State Ionics,* **129**:p.63-94, (2000).

[4] Gao, W., Sammes, N.M., *An Introduction to Electronic and Ionic Materials.*, World Scientific, (1999).

[5] de With, G., Process Control in the Manufacture of Ceramics., p.28-67, in *Processing of Ceramics - Part I*, Brook, R. J. (ed.), VCH, (1995).

[6] Bortzmeyer, D., Die Pressing and Isostatic Pressing., p.126-151, in *Processing of Ceramics - Part I*, Brook, R. J. (ed.), VCH, (1995).

[7] Van Herle, J., Horita, T., Kawada, T., Sakai, N., Yokokawa, M. Dokiya, Preparation of Doped Ceria Powder, in *4th International Symposium on Solid Oxide Fuel Cells.*, p.1082-,

[8] Rao, V. V. S., ., Rao, R.V.G., Biswas, A.B., Thermogravimetric Analysis of La, Ce, Pr and Nd Oxalates in Air and in Carbon Dioxide Atmosphere., *Journal of Inorganic and Nuclear Chemistry,* **27**:p.2525-2531, (1965).

[9] Mobius, R., Dietzold, W., Matthes, F., Zur Differentialthermoanalyse der Oxalathydrate der Seltenen Erdmetalle., *Journal of Inorganic and Nuclear Chemistry,* **28**(9): p.1847-1853, (1966).

[10] Mobius, R., Matthes, F., Zur Thermodgravimetrie der Oxalathydrate der Seltenen Erdmetalle, *Journal of Inorganic and Nuclear Chemistry,* **28**(8): p.1601-1607, (1966).

[11] Rao, S. V. V., Rao, R.V.G., Biswas, A.B., Thermal Decomposition of Cerous Oxalate and Variation of Surface Area of the Products., *Journal of the American Ceramic Society,* **47**(7): p.356-360, (1964).

[12] Sameshima, S., Ono, H., Sonoda, K., Higashi, K., Hirata, Y., Powder Preparation and Sintering of Rare Earth-Doped Ceria., in *Pac-Rim2,*

[13] Yahiro, H., Eguchi, Y., Eguchi, K., Arai, H., Oxygen Ion Conductivity of the Ceria-Samarium Oxide System with Fluorite Structure., *Journal of Applied Electrochemistry,* **18**:p.527-531, (1988).

[14] Beekmans, N. M., Heyne, L., Correlation Between Impedance, Microstructure and Composition of Calcia Stabilised Zirconia., *Electrochimica Acta,* **21**:p.303-310, (1976).

[15] Scardi, P., Di Maggio, R., Lutterotti, L., Maistrelli, P., Thermal Expansion Anisotropy of Ceria-Stabilized Tetragonal Zirconia., *Journal of the American Ceramic Society,* **75**(10): p.2828-2832, (1992).

[16] Shuk, P., Greenblatt, M., Hydrothermal Synthesis and Properties of Mixed Conductors Based on $Ce_{1-x}Pr_xO_{2-d}$ Solid Solutions., *Solid State Ionics,* **116**:p.217-223, (1999).

[17] Rahaman, M. N., Zhou, Y.C., Effect of Solid Solution Additives on the Sintering of Ultra-fine CeO_2 Powders., *Journal of the European Ceramic Society,* **15**:p.939-950, (1995).

[18] Pijolat, M., Prin, M., Soustelle, M., Touret, O., Nortier, P., Surface Area Stability of Lanthanum-Doped Ceria., *Solid State Ionics,* **63-65**:p.781-785, (1993).

[19] Hirano, M., Inagaki, M., Preparation of Monodispersed Cerium(IV) Oxide Particles by Thermal Hydrolysis: Influence of the Presence of Urea and Gd Doping on their Morphology and Growth., *Journal of Materials Chemistry,* **10**:p.473-477, (2000).

[20] Hartridge, A., Krishna, M.G., Bhattacharya, A.K., A Study of Nanocrystalline CeO_2/PrO_x Optoionic Thin Films: Temperature and Oxygen Vacancy Dependence., *Materials Science and Engineering,* **B57**:p.173-178, (1999).

[21] Taylor, R. E., Estimation Techniques and Selected Effects., in *Thermal Expansion of Solids*, Ho, C. Y. (ed.), ASM International, (1998).

[22] Steele, B. C. H., Oxygen Transport and Exchange in Oxide Ceramics., *Journal of Power Sources,* **49**:p.1-14, (1994).

[23] Mogensen, M., Lindegaard, T., Hansen, U.R., Physical Properties of Mixed Conductor Solid Oxide Fuel Cell Anodes of Doped CeO_2., *Journal of the Electrochemical Society,* **141**(8): p.2122-2128, (1994).

[24] Lange, F. F., Contributions of Sintering and Coarsening to Densification: A thermodynamic approach., p.57-70, in *Advanced Ceramics III*, Somiya, S. (ed.), Elsevier Science Publishers Ltd, (1990).

[25] Van Herle, J., Horita, T., Kawada, T., Sakai, N., Yokokawa, H., Dokiya, M., Fabrication and Sintering of Fine Yttria Doped Ceria Powder., *Journal of the American Ceramic Society,* **80**(4): p.933-940, (1997).

[26] Lee, W. E., Rainforth, W.M., *Ceramic Microstructures, Property Control by Processing.*, Chapman and Hall, (1994).

[27] McBride, J. R., Hass, K.C., Poindexter, B.D., Weber, W.H., Raman and X-ray Studies of $Ce_{1-x}RE_xO_{2-y}$, where RE=La, Pr, Nd, Eu, Gd, and Tb., *Journal of Applied Physics,* **76**(4): p.2435-2441, (1994).

[28] Van Herle, J., Horita, T., Kawada, T., Sakai, N., Yokokawa, H., Dokiya, M., Sintering Behaviour and Ionic Conductivity of Yttria-Doped Ceria., *Journal of the European Ceramic Society,* **16**:p.961-973, (1996).

[29] Mogensen, M., Lindegaard, T., Hansen, U.R., Mogensen, G., Optimalizing Mixed Conductor SOFC Anodes of Doped CeO_2., in *Symposium on Ionics and Mixed Conducting Ceramics,* (1994). San Francisco.

[30] Lewis, G. S., Atkinson, A., Steele, B.C.H., Sintering of Gadolinia-Doped Ceria at Reduced Temperature., in *Fourth European SOFC Forum,* p.773-782, (2000). Lucerne, Switzerland.

[31] Macdonald, J. R., *Impedance Spectroscopy: Emphasizing Solid Materials and Systems*, Wiley-Interscience, (1987)

[32] Steele, B. C. H., Appraisal of $Ce_{1-y}Gd_yO_{2-y/2}$ Electrolytes for IT-SOFC Operation at 500 °C., *Solid State Ionics,* **129**:p.95-110, (2000).

[33] Gerhardt, R., Nowick, A.S., Grain Boundary Effect in Ceria Doped with Trivalent Cations: I, Electrical Measurements., *Journal of the American Ceramics Society,* **69**(9): p.641-646, (1986).

[34] Lubke, S., Wiemhofer, H. D., Electronic Conductivity of Gd-Doped Ceria with Additional Pr-Doping., *Solid State Ionics,* **117**(3-4): p.229-243, (1999).

[35] Maricle, D. L., Swarr, T.E., Karavolis, S., Enhanced Ceria - a Low-Temperature SOFC Electrolyte., *Solid State Ionics,* **52**:p.173-182, (1992).

[36] Tian, C., Chan, S.-W., Ionic Conductivities, Sintering Temperatures and Microstructures of Bulk Ceramic CeO_2 Doped with Y_2O_3., *Solid State Ionics,* **134**:p.89-102, (2000).

Chapter Five

5 Conclusions and Recommendations

5.1 Overview

This chapter contains conclusions drawn from the discussion of the results presented within this thesis. The final part of this chapter consists of recommendations for future work based on the conclusions presented. The use of the simplified sample composition codes continues in this chapter, refer to Appendix 4.

The purpose of this research was to investigate the double doping of $Ce_{0.8}Gd_{0.2}O_{2-\delta}$ with praseodymia and samaria. Praseodymia double doping was examined to gauge its effectiveness in increasing the conductivity and extending the ionic domain of the $Ce_{0.8}Gd_{0.2}O_{2-\delta}$ material considered due to the controversy and general lack of consensus on its effectiveness. Samaria was considered as it was the other co-dopant proposed by the paper first reporting double doping. While the initial paper reported the results of one samaria containing sample, there appears to have been little further work looking at the use of samaria as a double dopant in $Ce_{0.8}Gd_{0.2}O_{2-\delta}$. Further, some aspects of the fabrication method were also investigated.

5.2 Conclusions

The conclusions for this work have been divided into three sections: Powder Preparation and Characterisation, Pellet Fabrication and Characterisation and finally Impedance Spectroscopy. Following these sections is a synopsis of the conclusions presented.

5.2.1 Powder Preparation and Characterisation

Results obtained from x-ray diffraction and Raman spectroscopy indicate that the two preparation methods employed, co-precipitation and a Pechini method variant, produce single phase oxide powders with the cubic fluorite structure. This phase was stable to at least 1273 K for all of the compositions studied, with no evolution of secondary phases.

Thermal analysis of the co-precipitation intermediate products show them to consist of a single mixed oxalate species rather than separate oxalates for each metal ion. There were only slight differences between the compositions tested; the main difference was that the base material (CG) showed a more intense initial endothermic process and an exothermic oxalate decomposition process offset to a higher temperature compared to the double doped materials.

Thermal expansion coefficients, determined by high temperature x-ray diffraction, revealed that the powder preparation methods employed caused little or no difference. The change in composition of the materials did effect the thermal expansion, the addition of praseodymia causing a greater change than samaria addition. The use of praseodymia as a double dopant increased the thermal expansion coefficient from ca. 1 x 10^{-5} K^{-1} to ca. 1.25 x 10^{-5} K^{-1}. Use of samaria as a double dopant caused only a slight increase in thermal expansion. There was no systematic variation due to double dopant concentration observed for either of the double dopant species. The thermal expansion coefficient of the praseodymia containing samples is more closely matched to the thermal expansion of the ferritic stainless steels than the CG base material.

Ferritic stainless steels have been proposed by other researchers as a possible intermediate temperature interconnect material[1].

Physical characterisation of the oxide powders, that is particle size measurements and surface area analysis, revealed that slight variations between the compositions were detectable. The median particle size ranged between 0.22 μm and 0.25μm, with praseodymia containing powders consistently having smaller particles than the base CG material or the samaria containing samples. Surface area measurements ranged between 15 m^2/g and 22 m^2/g with no systematic variations. The preparation technique did not seem to have a marked effect on these physical powder properties.

Scanning electron microscopy inspection of the oxide powders, reveals that the preparation methods produce powders of differing morphologies. The co-precipitated powders consist of many elongated crystals, formed out of the primary crystallites; the Pechini method powders consist of what appear to be highly porous agglomerates of primary crystallites.

5.2.2 Pellet Fabrication and Characterisation

The powders prepared by the Pechini method proved difficult to form into pellets without the use of a binder; the co-precipitated powders did not require the use of a binder, though they were less fragile when a binder was employed. X-ray microscopy of green and sintered pellets indicates that the use of a binder reduces the density variation within a pellet when compared to pellets prepared without a binder.

Sintering studies on the co-precipitated CG material indicated that a sintering regime of 10 hours at 1400 °C yielded pellets with a density of at least 96% of the theoretical density. Powders prepared by the Pechini method, while showing rapid initial densification, only obtained 96% density after being sintered for 10 hours at 1600 °C. The sintered pellets prepared from Pechini powders also had a high rejection rate due to cracking and delamination.

The use of samaria as a double dopant had no significant effect on the sintering of the pellets. The praseodymia containing powders were more sinterable than either the base material or the samaria containing powders. The praseodymia containing samples achieved a sintered density of 98-99% of theoretical after sintering for 10 hours at 1400 °C; this may be due to the slightly smaller particle size of the praseodymia containing powders or the praseodymia may be acting to enhance the sintering process.

Visual examination of the sintered pellets using SEM shows that both of the powder preparation methods produce grains of similar shapes. It is also noted that both of the double dopant species employed appear to inhibit grain growth of the material.

Particle induced x-ray emission (PIXE) analysis of sintered pellets indicates that the most abundant impurity present was cobalt, with an average content of 0.17 atom%. Backscattered electron imaging and energy dispersive x-ray (EDX) elemental mapping failed to find any evidence of solute segregation or grain boundary phases (a common reason for poor electrical performance of oxide ion conductors).

5.2.3 Impedance Spectroscopy

Presentation of the impedance spectroscopy data in complex plane form shows that at low temperature grain bulk, grain boundary and electrode conduction processes can be resolved; as the temperature is increased the individual processes become less distinct until they can no longer be separated.

Comparison of the well resolved low temperature data indicates that the samples prepared from Pechini method powders have a grain boundary resistance higher than the grain bulk. In the samples prepared from the co-precipitated powder this phenomenon was reversed.

Conductivity calculations based on high temperature (600 °C, in air) data reveals that for any given composition the co-precipitated samples consistently gave higher conductivities than those prepared by the Pechini method.

The effect of double dopant content on conductivity was evaluated. All of the praseodymia containing samples gave higher conductivities than the base CG material, with the maximum in conductivity (1.33×10^{-2} S cm^{-1} at 600 °C in air) occurring for the composition $Ce_{0.8}Gd_{0.185}Pr_{0.015}O_{2-\delta}$. The use of samaria as the double dopant material did not increase the conductivity to the same extent as praseodymia addition; the highest conductivity (at 600 °C in air) of 1.04×10^{-2} S cm^{-1} being recorded for the composition $Ce_{0.8}Gd_{0.19}Sm_{0.01}O_{2-\delta}$. The conductivity for the base CG material under identical conditions was 8.89×10^{-3} S cm^{-1}.

Comparisons of the individual grain boundary and grain bulk conductivities indicate that praseodymia increases the conductivity of both, though the grain boundary conductivity is increased to a greater extent. This partially supports the findings of Lubke[2] and the comment by Steele[3] that the double dopant was acting to increase the grain boundary conductivity, the results found here also suggest that the grain bulk conductivity is being increased to an extent.

Activation energy for conduction values were calculated by the construction of Arrhenius type plots and measuring the slope of the resultant straight line. It was observed that all of the samples exhibited a change in activation energy at ca. 400 °C. This change was interpreted as indicating the samples' grain boundaries were 'clean' as discussed by Steele[3]. When individual conduction processes, that is grain boundary and grain bulk conduction, were plotted it was seen that the grain bulk activation energy also exhibited a change at ca. 400 °C, this may indicate the presence of dopant ion-oxygen vacancy pairs.

Calculated activation energies show that compositions which exhibited the highest conductivity also had the lowest activation energies. Activation energies for all of the praseodymia containing samples were lower than that for the CG base material. The activation energies for the samaria containing samples were generally higher than those of the praseodymia containing samples, but still slightly lower than that of CG.

There was no apparent extension of the ionic domain of the base CG material by the addition of either double dopant. The ionic domain boundary for all three samples was 10^{-26} atm at 800 K.

5.2.4 Conclusions Summary

Of the two powder preparation techniques employed it appears the co-precipitation method is to be preferred. The reasons being the co-precipitated powder was more easily fabricated into green pellets and more sinterable. The green pellets did not show the cracking and delamination problems on sintering exhibited by green pellets prepared from the Pechini powders. Also the pellets prepared using the co-precipitated powders showed higher conductivities than their Pechini method equivalents.

Of the two double dopants investigated, the praseodymia dopant gave greater performance improvements. Praseodymia containing samples showed increased sinterability and improved conductivity.

This work confirms that the use of praseodymia as a double dopant in $Ce_{0.8}Gd_{0.2}O_{2-\delta}$ does increase the conductivity of the material, however Maricle et al's[4] finding of a two orders of magnitude increase in the ionic domain could not be substantiated.

5.3 Recommendations

Future work on these double doped materials should include customising the sintering regime for the praseodymia double doped materials. These samples attained a high density under the sintering conditions employed for this work, it may be possible to sinter them to a sufficient density (96% of theoretical) at lower temperatures.

More impedance spectroscopy at low oxygen partial pressures needs to be performed to more accurately determine the electrolytic domain of the materials.

Experimental fuel cells should be constructed employing the best performing materials. The materials' performance in a fuel cell could then be evaluated, particularly power densities and long term stability. Construction of fuel cells with different anode/electrolyte/cathode combinations should also be trialed to obtain an optimum combination for these particular electrolytes.

The materials studied here could also be evaluated as possible oxygen sensor and oxygen pump electrolytes.

Bibliography

[1] Steele, B. C. H., Materials for IT-SOFC Stacks; 35 Years R&D: The Inevitability of Gradualness?, *Solid State Ionics,* **134**:p.3-20, (2000).

[2] Lubke, S., Wiemhofer, H. D., Electronic Conductivity of Gd-Doped Ceria with Additional Pr-Doping., *Solid State Ionics,* **117**(3-4): p.229-243, (1999).

[3] Steele, B. C. H., Appraisal of $Ce_{1-y}Gd_yO_{2-y/2}$ Electrolytes for IT-SOFC Operation at 500 °C., *Solid State Ionics,* **129**:p.95-110, (2000).

[4] Maricle, D. L., Swarr, T.E., Karavolis, S., Enhanced Ceria - a Low-Temperature SOFC Electrolyte., *Solid State Ionics,* **52**:p.173-182, (1992).

Appendix One

Kröger-Vink Notation

The most commonly used notation to describe defect chemistry. In this notation a defect is symbolised by a major character in combination with a subscript and superscript character. The major symbol refers to the species in question, the subscript identifies the lattice site occupied by the species and the superscript refers to the effective charge. The charge is not the charge of the species; rather it is the effective charge of the defect with respect to the ideal crystal lattice. Charge symbols are as listed in Table 1:

Table 1 Symbols used to denote defect charge.

Charge	Symbol
Positive	$\bullet$
Negative	$/$
Neutral	x

Electrons and electron holes are signified $e^{/}$ and $h^{\bullet}$ respectively.
Vacancies are given the symbol V, with interstitial sites given the symbol i.

For example, in a system AB, where A and B have charges of 2+ and 2- respectively, with an impurity C having a charge 1+ the following notations would apply: .

A_A^x an A on an A lattice site

B_B^x a B on a B lattice site

$C_A^{/}$ impurity C occupying an A site, with the defect having an effective charge of 1- (in the ideal, pure, material the A lattice site has an effective charge of 2- so that when occupied by an A ion the overall charge is zero)

$V_B^{\bullet\bullet}$ a vacant B site, effective charge 2+

$B_i^{//}$ a B ion occupying an interstitial site, effective charge 2-

This is not a comprehensive list but a number of examples of how the notation is used. Often if a defect has an effective neutral charge no charge superscript is used

Appendix Two

Basic Crystallography

Unit Cells

A crystal is a periodic three dimensional array of ordered atoms. The basic repeating unit is termed the unit cell. Its size and shape are determined by six parameters: a,b,c the length of the three sides, α, β, γ the three angles of the unit cell, refer Figure 1.

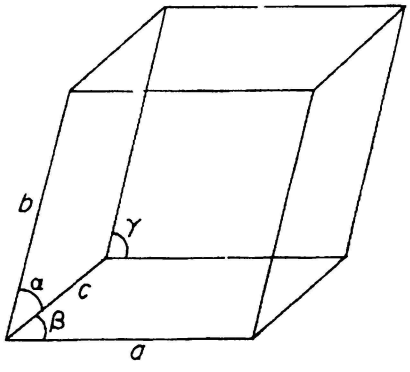

Figure 1 Unit Cell Parameters.

There are seven possible shapes a unit cell can take, termed the seven crystal systems. The details of these systems are shown in Table 1.

Table 1 Charactersitics of the Seven Crystal Systems.

System	Parameters	
Cubic	$a = b = c$	$\alpha = \beta = \gamma = 90°$
Tetragonal	$a = b \neq c$	$\alpha = \beta = \gamma = 90°$
Hexagonal	$a = b \neq c$	$\alpha = \beta = 90° \gamma = 120°$
Rhombohedral	$a = b = c$	$\alpha = \beta = \gamma \neq 90°$
Orthorhombic	$a \neq b \neq c$	$\alpha = \beta = \gamma = 90°$
Monoclinic	$a \neq b \neq c$	$\alpha = \beta = 90° \neq \gamma$

Triclinic	$a \neq b \neq c$	$\alpha \neq \beta \neq \gamma \neq 90°$

The simplest lattice type is known as primitive. A unit cell with a primitive lattice contains a single equivalent lattice point, typically sited at each corner of the unit cell. For unit cells with a primitive lattice type the only translational symmetry is that of the unit cell itself. There are three types of non-primitive cells, in addition to the translational symmetry of the unit cell, there is also transitional symmetry within the unit cell. The non-primitive unit cells are: body-centred (where in addition to the corners, an atom sits in centre of the cell), face-centred (in addition to atoms at the corners there are also atoms in the centre of each face of the unit cell) and end-centred (in addition to atoms at each corner there are also atoms in the centre of two opposite unit cell faces). When these four cell types are incorporated with the seven crystal systems a total of 14 categories, termed the Bravias Lattices, are possible.

Miller Indices

It is possible to pass a plane through a unit cell so that it cuts the a axis at a distance of a/h, b axis at b/k and c axis at c/l, where h, k and l are integers. Each plane is a representative member of a parallel set of equally spaced planes, with spacing d_{hkl}, refer Figure . The values h, k and l are called the Miller indices and are used to define lattice planes. The planes used in Figure 2 are (213) planes.

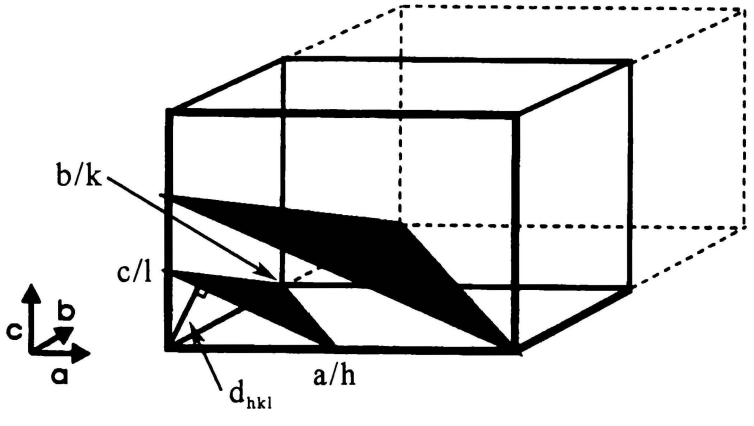

Figure 2 Illustration of Miller Indices.

The relationship between the lattice parameter and d-spacing can be determined geometrically and varies depending on the crystal system. The expressions for lattice parameters in terms of miller indices and d-spacings are shown in Table 2.

Table 2 d-spacing Expressions for Different Crystal Systems.

Crystal System	Expression of d_{hkl} in terms of lattice parameter and Miller indices.
Cubic	$\frac{1}{d^2} = \frac{h^2 + k^2 + l^2}{a^2}$
Tetragonal	$\frac{1}{d^2} = \frac{h^2 + k^2}{a^2} + \frac{l^2}{c^2}$
Orthorhombic	$\frac{1}{d^2} = \frac{h^2}{a^2} + \frac{k^2}{b^2} + \frac{l^2}{c^2}$
Hexagonal	$\frac{1}{d^2} = \frac{4}{3}\left(\frac{h^2 + hk + k^2}{a^2}\right) + \frac{l^2}{c^2}$
Monoclinic	$\frac{1}{d^2} = \frac{1}{\sin^2\beta}\left(\frac{h^2}{a^2} + \frac{k^2\sin^2\beta}{b^2} + \frac{l^2}{c^2} - \frac{2hl\cos\beta}{ac}\right)$
Triclinic	Yields a complex expression

Appendix Three

CeO_2 JCPDS File

43-1002 Wavelength= 1.54056

CeO2

Cerium Oxide

Cerianite, syn

Rad.: CuKa1 λ: 1.5405 Filter: Mono. d-sp: Calculated

Cut off: 15.0 Int.: Calculated I/Icor.: 13.20

Ref: Grier, D., McCarthy, G., North Dakota State University, Fargo, North Dakota, USA, ICDD Grant-in-Aid, (1991)

Sys.: Cubic S.G.: Fm3m (225)

a: 5.41134 b: c: A: C:

α: β: γ: Z: 4 mp:

Ref: Ibid.

Dx: 7.215 Dm: SS/FOM: F_{10}=573(.0017, 10)

Peak height intensity. Calculation of diffractometer peak intensities done with MICRO-POWD v. 2.2 (D. Smith and K. Smith) using default instrument broadening function (NBS Table), diffracted beam monochromator polarization correction, and atomic scattering factors corrected for anomalous dispersion. Cell parameters from 34-394. Atomic positions from Wyckoff for fluorite structure with Ce in 4a and O in 8c. Isotropic thermal parameters estimated as 1.0 for each atom. Ca F2 type. PSC: cF12. Mwt: 172.12. Volume[CD]: 158.46.

d Å	Int	h	k	l
3.12400	100	1	1	1
2.70600	27	2	0	0
1.91320	46	2	2	0
1.63160	34	3	1	1
1.56210	6	2	2	2
1.35280	6	4	0	0
1.24140	12	3	3	1
1.21000	7	4	2	0
1.10460	10	4	2	2
1.04140	9	5	1	1

©1995 JCPDS-International Centre for Diffraction Data. All rights reserved.

Appendix Four

Sample Composition Codes

Table 1 Composition Codes Used for Sample Identification.

Composition	Code
$Ce_{0.8}Gd_{0.2}O_{2-\delta}$	CG
$Ce_{0.8}Gd_{0.195}Pr_{0.005}O_{2-\delta}$	CGP005
$Ce_{0.8}Gd_{0.19}Pr_{0.01}O_{2-\delta}$	CGP01
$Ce_{0.8}Gd_{0.185}Pr_{0.015}O_{2-\delta}$	CGP015
$Ce_{0.8}Gd_{0.17}Pr_{0.03}O_{2-\delta}$	CGP03
$Ce_{0.8}Gd_{0.15}Pr_{0.05}O_{2-\delta}$	CGP05
$Ce_{0.8}Gd_{0.19}Sm_{0.01}O_{2-\delta}$	CGS01
$Ce_{0.8}Gd_{0.17}Sm_{0.03}O_{2-\delta}$	CGS03
$Ce_{0.8}Gd_{0.15}Sm_{0.05}O_{2-\delta}$	CGS05

Samples, in addition to a composition code, may also have an indication of the preparation method employed for their fabrication - either the modified Pechini method (abbreviated to Pechini), or co-precipitation (abbreviated to coppt) – this is only applicable to the composition codes CG, CGP03 and CGS03. All other compositions have been prepared by the co-precipitation method only. If there is no indication of preparation method then the material has been prepared by co-precipitation.